

**UNIVERSITY OF BUCHAREST**

**Semiclassical and Boson  
Descriptions of the Wobbling  
Motion in Odd-A Nuclei**

Robert Poenaru

Faculty of Physics

April 2022

## *Abstract*

**Keywords:** *nuclear shape, nuclear deformation, collective parameters, triaxiality, wobbling.*

sheeesh...

## *Acknowledgements*

sheeesh...

# Contents

<b>Abstract</b>	<b>i</b>
<b>Acknowledgements</b>	<b>ii</b>
<b>1 Introduction</b>	<b>1</b>
<b>2 Shape of Nuclei</b>	<b>3</b>
2.1 Nuclear deformation . . . . .	3
2.1.1 Collective coordinates . . . . .	3
2.1.2 Nuclear radius under rotation . . . . .	4
2.1.3 Multipole deformations . . . . .	5
2.1.4 Quadrupole Deformation . . . . .	6
2.1.4.1 Axial quadrupole deformations . . . . .	9
2.1.4.2 Non-Axial quadrupole deformations . . . . .	11
2.1.4.3 Lund Convention . . . . .	13
2.1.4.4 Alternative description of the quadrupole deformation . . . . .	13
2.1.5 Nuclear Shapes and Softness . . . . .	15
<b>3 Nuclear Models</b>	<b>18</b>
3.1 Introduction . . . . .	18
3.2 Shell model . . . . .	18
3.3 Deformed Shell Model . . . . .	27
3.3.1 Deformed Shell Model - Nilsson Model . . . . .	28
3.3.2 Single-particle states in deformed nuclei . . . . .	32
3.4 Collective Model . . . . .	48
3.4.1 Bohr Hamiltonian . . . . .	49
3.4.2 Nuclear Vibration . . . . .	53
3.4.3 Nuclear Rotation . . . . .	57
3.4.4 Superimposed Rotations and Vibrations . . . . .	64
3.4.5 Collective Quantities . . . . .	67
<b>4 Triaxial Nuclei and Their Signatures</b>	<b>80</b>
4.1 Non-axial nuclei . . . . .	80

4.1.1	Triaxial Rotor Model . . . . .	82
4.1.2	Triaxial Particle + Rotor Model . . . . .	83
4.2	Stable Triaxial Deformation . . . . .	88
4.3	Fingerprints of Triaxiality . . . . .	92
4.3.1	Chiral motion . . . . .	93
4.4	Wobbling Motion . . . . .	94
<b>5</b>	<b>Wobbling Motion in Nuclei</b>	<b>97</b>
5.1	Wobbling Motion in Even-Even Nuclei . . . . .	97
5.1.1	Testing the Harmonic Approximation . . . . .	104
5.2	Wobbling Motion in Odd-Mass Nuclei . . . . .	110

# Chapter 1

## Introduction

Ground-state nuclear shapes with spherical symmetry or axial symmetry are predominant across the chart of nuclides. Near closed shells, the deformation is indeed sufficient that models based on spherical symmetries can be used to describe nuclear properties (e.g., energies, quadrupole moments, and so on). Besides the spherical and axially-symmetric shapes, the existence of triaxial nuclear deformation was theoretically predicted a long time ago [1]. The rigid triaxiality of nuclei is defined by the asymmetry parameter  $\gamma$ , giving rise to unique quantum phenomena (this parameter will be characterized later on). The quantum mechanical properties of the rigid triaxial shapes drew a lot of attention within the nuclear physics community lately, since the description of nuclear properties for the deformed nuclei represents a great challenge from both an experimental and a theoretical standpoint (e.g., great progress for the experimental evidence of strong nuclear deformation has only been possible after the 2000s). It is worth mentioning that some experiments concerning alpha-alpha particle reactions induced in heavy nuclei in the early 1960s (e.g., [2]) helped to produce decent amount of data related to the rotational in the high-spin region ( $\geq 20\hbar$ ). Within the experimental studies made by Morinaga et al., the alpha reactions which were induced in the nuclei were generated by the formation of a so-called *compound nucleus*. This system may exist at a large spin value due to the absorption of the angular momentum from the incident particle (i.e., spin values up to  $\approx 25 \hbar$  can be obtained from a 50 MeV alpha particle energy - relative to the target nucleus [2]).

The physics of *high-spin* states have been studied from the early 1950s, with the major breakthrough on the theoretical side made by Bohr and Mottelson [1].

The elusive properties of nuclear rotation were described in terms of the rotational degrees of freedom associated with other nuclear degrees of freedom (e.g., particle-vibration, quadrupole-quadrupole, parity, and so on).

# Chapter 2

## Shape of Nuclei

### 2.1 Nuclear deformation

Most of the nuclei across the nuclide chart are spherical or symmetric in their ground state. Moreover, for the axially symmetric nuclei (i.e, either *oblate* or *prolate*), there is a prolate over oblate dominance. The spherical shell model only describes nuclei near the closed shells. On the other side, for the nuclei that lie far from closed shells, a deformed potential must be employed.

In the case of even-even nuclei, unique band structures resulting from the vibrations and rotations of the nuclear surface (as proposed by Bohr and Mottelson [1] in the *Geometric Collective Model* - GCM) appear in the energy range 0-2 MeV.

Within the GCM, the nucleus is described as a classical charged liquid drop. For the low-lying energy spectrum, usually, the compression of nuclear matter and the nuclear skin thickness are neglected. This results in the final picture of a liquid drop with a constant nuclear density and a sharp surface [3].

#### 2.1.1 Collective coordinates

The nuclear surface can be described via an expansion of the spherical harmonic functions, with some time-dependent parameters as *expansion coefficients*. The

expression of the nuclear shape is shown below [3]:

$$R(\theta, \varphi, t) = R_0 \left( 1 + \sum_{\lambda=0}^{\infty} \sum_{-\lambda}^{\lambda} \alpha_{\lambda\mu}(t) Y_{\lambda}^{\mu}(\theta, \varphi) \right) . \quad (2.1)$$

In 2.1,  $R$  denotes the nuclear radius as a function of the spherical coordinates  $\theta, \varphi$  expressing the direction, and the time  $t$ , while  $R_0$  is the radius of the spherical nucleus when all the expansion coefficients vanish. It is worth mentioning that the expansion coefficients  $\alpha_{\lambda\mu}$  act as *collective coordinates*, since the time-dependent amplitudes describe the vibrations of the nuclear surface.

### 2.1.2 Nuclear radius under rotation

To get a grasp at the physical meaning behind the deformation parameters that are used to describe the nuclear surface, it is instructive to see what happens when the system undergoes a rotation transformation.

The function  $R(\theta, \varphi)$  describes the original (non-rotated) nuclear shape. Rotating the system will result in the change of the angular coordinates  $(\theta, \varphi)$  to  $(\theta', \varphi')$ , which will correspond to a new function  $R'(\theta', \varphi')$ . Moreover, both nuclear surfaces (i.e., the non-rotated and the rotated one) must hold the equality:

$$R'(\theta', \varphi') = R(\theta, \varphi) \quad (2.2)$$

The rotational invariance of  $R$  employs that  $R'(\theta, \varphi)$  must have the same functional form, but the expansion coefficients  $\alpha_{\lambda\mu}$  must be rotated, meaning:

$$\sum_{\lambda\mu} \alpha'_{\lambda\mu} Y'_{\lambda\mu}(\theta, \varphi) = \sum_{\lambda\mu} \alpha_{\lambda\mu} Y_{\lambda\mu}(\theta, \varphi) . \quad (2.3)$$

Note that in Eq. 2.3, the spherical harmonics  $Y'_{\lambda\mu}$  are obtained via the usual rotation matrices. Finally, the invariance of Eq. 2.1 is achieved if the set of parameters  $\alpha_{\lambda\mu}$  transform similarly to a *spherical tensor with angular momentum*  $\lambda$  [4], that is:

$$\alpha'_{\lambda\mu} = \sum_{\mu'} \mathcal{D}_{\mu\mu'}^{(\lambda)} \alpha_{\lambda\mu'} . \quad (2.4)$$

Besides the spherical tensor character, the collective coordinates also have the following properties (emerging from Eq. 2.1):

- Complex Conjugation.

$$Y_{\lambda\mu}^*(\theta, \varphi) = (-1)^\mu Y_{\lambda-\mu}(\theta, \varphi), \quad (2.5)$$

$$\alpha_{\lambda\mu}^* = (-1)^\mu \alpha_{\lambda-\mu}. \quad (2.6)$$

- Parity - the coordinates  $\alpha_{\lambda\mu}$  must undergo the same change of sign under a parity transformation as the spherical harmonics, in order to keep the invariance of the nuclear surface.

$$(r, \theta, \varphi) \xrightarrow{P} (r, \pi - \theta, \pi + \varphi),$$

$$Y_{\lambda\mu}(\theta, \varphi) \xrightarrow{P} Y_{\lambda\mu}(\pi - \theta, \pi + \varphi) = (-1)^\lambda Y_{\lambda\mu}(\theta, \varphi).$$

Therefore, the parity of the expansion coefficients are:

$$\pi(\alpha_{\lambda\mu}) = (-1)^\lambda. \quad (2.7)$$

### 2.1.3 Multipole deformations

In the expansion of the nuclear surface defined by Eq. 2.1, the different values for  $\lambda$  will determine different effects regarding the physical aspects of the nucleus. As such, the first values of  $\lambda$  will be examined in terms of the physical meaning.

**Monopole mode** This corresponds to the first value of  $\lambda = 0$ . This is the simplest mode of *deformation* of a nuclear surface. Within this approximation, the spherical harmonic  $Y_0^0$  is constant, which would imply that any non-vanishing values for  $\alpha_{00}$  will correspond to the change in radius of the nucleus. This kind of excitation is also called *breathing mode* of the nucleus [1, 3]. The energy required for this kind of excitation mode is very large, since it implies a compression of the nuclear matter. As a result, this mode is irrelevant in the low-lying excited spectra of atomic nuclei.

**Dipole mode** Corresponds to  $\lambda = 1$ . In reality, this type of mode does not manifest itself as a deformation of the nucleus, but rather as a shift of the

nuclear center of mass. In the lowest order  $\lambda = 1$ , the shift is in fact a translation of the entire nucleus, and it does not represent an actual nuclear excitation.

**Quadrupole mode** Excited modes that correspond to  $\lambda = 2$ . These are the most important collective excitations that take place inside the nucleus. The loss of axial symmetry, triaxial deformations, and other shape-specific transitions that happen within the nucleus are mostly described (and very accurately) via the quadrupole effects.

**Octupole mode** This corresponds to the next increasing value of  $\lambda = 3$ , representing the main asymmetric excitations of a nucleus with states of negative-parity. The specific shape of a nuclear system governed by octupole deformations is similar to that of a pear.

**Hexadecapole deformations** Excitations which correspond to  $\lambda = 4$ . Within the nuclear theory, this is considered the highest angular momentum which can still provide relevant information for the nuclear phenomena that are studied. Currently, there is no clear evidence for pure excitations with hexadecapole nature, however, these excitations seem to have a major role in the admixture to quadrupole excitations for the ground-state shape of heavy nuclei [3].

The multipole deformations for the cases  $\lambda = 1, 2, 3$  and  $\lambda = 4$  discussed above are pictorially shown in Fig. 2.1. Excitations with higher angular momentum than the mentioned ones have practically no application within the study of atomic nuclei. Moreover, one can also see that there is an intrinsic limitation on the maximal value of  $\lambda$ , which dictates the smallness of the individual bumps of the surface (see Fig. 2.1). These bumps are described by the spherical harmonics  $Y_\lambda^\mu$ , and they decrease in size with increasing values of  $\lambda$ , but with the physical limitation given by the size of the nucleon diameter.

### 2.1.4 Quadrupole Deformation

One of the most important excitation modes (vibrational degrees of freedom) is the quadrupole deformation, corresponding to  $\lambda = 2$ . In the case of pure quadrupole

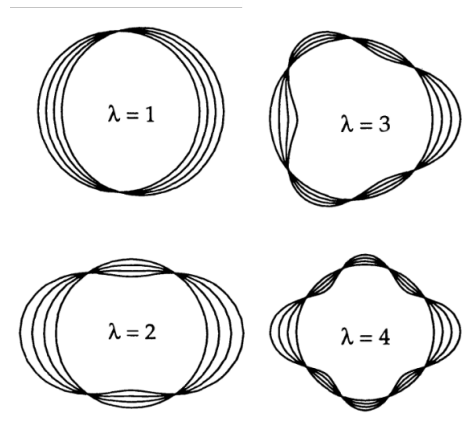


FIGURE 2.1: Graphical representation of the first few modes of excitations of the nuclear surface. The figure is taken from Ref. [3].

deformation, the nuclear surface will be given by the following expression:

$$R(\theta, \varphi) = R \left( 1 + \sum_{\mu} \alpha_{2\mu} Y_2^{\mu}(\theta, \varphi) \right). \quad (2.8)$$

From this expression, the term  $\alpha_{00}$  is of second order in  $\alpha_{2\mu}$  and it can be neglected further on. This term also reflects the conservation of volume [3, 4]. The real and independent degrees of freedom from the above expression are:  $\alpha_{20}$ , the real and imaginary parts of  $\alpha_{21}$ , and the real and imaginary parts of  $\alpha_{22}$ , respectively.

More insight in regard to the quadrupole shape of the nucleus can be achieved if one expresses  $R$  in terms of Cartesian coordinates. The spherical harmonics will attain a new form, depending on the Cartesian components of the unit vector pointing in a direction defined by  $(\theta, \varphi)$ :

$$\xi = \sin \theta \cos \varphi, \quad \eta = \sin \theta \sin \varphi, \quad \zeta = \cos \theta, \quad (2.9)$$

with the condition  $\xi^2 + \eta^2 + \zeta^2 = 1$ . With the expressions of the spherical harmonics as functions of  $(\xi, \eta, \zeta)$ , the nuclear radius will change accordingly (Cartesian expression  $R = R(\xi, \eta, \zeta)$ ). A relationship between the Cartesian components and the spherical ones for the deformation can be also obtained if one writes all coefficients  $\alpha_{2\mu}$  as functions of  $\alpha_{ij}$  (with  $i, j = \xi, \eta, \zeta$ ). Since the Cartesian deformations can be regarded as closely related to a stretch/contraction of the nucleus in a given direction, a first interpretation of the physical meaning behind the parameters  $\alpha_{2\mu}$  can be established:

- $\alpha_{20}$ : describes the stretching of the  $z$  axis with respect to the  $y$  and  $x$  axes.
- $\alpha_{2-2}$  and  $\alpha_{22}$ : give the relative length of the  $x$  axis compared to the  $y$  axis. Moreover, it also gives the oblique deformation in the  $x - y$  plane.
- $\alpha_{2-1}$  and  $\alpha_{21}$ : describe an oblique deformation, but with respect to the  $z$  axis.

With the set of parameters defined above, the shape and orientation of the nucleus can have arbitrary values (the coefficients  $\alpha_{2\mu}$  are mixing the shape and orientation), thus making the parametrization somewhat problematic. In order to fix that, the geometry can be changed if one considers the *principal axis system* (the PA reference system is a coordinate system in which the moments of inertia associated with the nucleus are diagonal). When using this reference frame, the number of parameters is still unchanged, however their physical significance becomes clearer. By denoting the new coordinate system with primed letters, nuclear radius will be described as a function  $R = R(\xi', \eta', \zeta')$ , with the conditions that  $\alpha'_{ij} = 0$ ,  $i \neq j$ . The condition will further imply that the newly expressed parameters ( $\alpha'_{2\mu}$ ) have the following form:

$$\begin{aligned}\alpha'_{2\pm 1} &= 0 , \\ \alpha'_{2\pm 2} &\equiv a_2 , \\ \alpha'_{20} &\equiv a_0 ,\end{aligned}\tag{2.10}$$

where the conveniently denoted terms  $a_2$  and  $a_0$  are some functions that depend on the Cartesian components  $\alpha_{\xi,\xi}$ ,  $\alpha_{\eta,\eta}$ ,  $\alpha_{\zeta,\zeta}$ . From this set of equations the physical significance of the five real and independent parameters is clearer:

- $a_0$  is indicating the stretch of  $z'$  axis w.r.t. the  $x'$  and  $y'$  axes.
- $a_2$  is indicating the asymmetry between the lengths of  $x'$  and  $y'$  axes, respectively.
- the three *Euler angles*  $\Theta = (\theta_1, \theta_2, \theta_3)$ . These angles will determine the orientation of the PA system  $(x', y', z')$  with respect to the laboratory-fixed frame  $(x, y, z)$ .

One can now clearly see the advantage of working within the PA system: rotation and shape vibration degrees of freedom can be completely separated. A change

in the Euler angles will result in a pure rotation of the nucleus (without changing its shape), while a change in shape will be affected exclusively by the  $a_0$  and  $a_2$  parameters. If  $a_2 = 0$ , then the nucleus has a shape with axial symmetry around the  $z$  axis (equal axis lengths along the  $x$  and  $y$  directions).

Another way of describing the excitations of quadrupole type is to adopt the parameters introduced by A. Bohr [5]. These two parameters can be viewed as a set of polar coordinates in the space generated by  $(a_0, a_2)$  and they are defined as:

$$\begin{aligned} a_0 &= \beta_2 \cos \gamma , \\ a_2 &= \frac{1}{\sqrt{2}} \beta_2 \sin \gamma , \end{aligned} \quad (2.11)$$

where the numeric factor  $\frac{1}{2}$  was added such that the following relation holds true:

$$\sum_{\mu} |\alpha_{2\mu}|^2 = \sum_{\mu} |\alpha'_{2\mu}|^2 = a_0^2 + 2a_2^2 = \beta_2^2 . \quad (2.12)$$

It is worth mentioning that the Eq. 2.12 is rotationally invariant, having the same value in the laboratory and the principal axes systems.

Now that the shape of the nucleus (i.e., the nuclear surface radius  $R$ ) can be described consistently with via the parameters defined in Eq. 2.11, one can calculate the stretching of the nuclear radius along any of the directions is given in terms of  $(\beta, \gamma)$  as follows:

$$\delta R_k = \sqrt{\frac{5}{4\pi}} \beta \cos\left(\gamma - \frac{2\pi k}{3}\right) . \quad (2.13)$$

#### 2.1.4.1 Axial quadrupole deformations

Using this set of new coordinates, the expression of the nuclear radius for axially quadrupole-deformed nuclei is given as:

$$R(\theta, \varphi) = R_0 (1 + \beta_2 Y_2^0(\theta, \varphi)) . \quad (2.14)$$

In Eq. 2.14, the parameter  $\beta_2$  is called the *quadrupole deformation parameter*, and its value dictates whether the nucleus is *oblate* -  $\beta_2 < 0$  (i.e., a flattened sphere), *prolate* -  $\beta_2 > 0$  (i.e., an elongated sphere, like a rugby ball), or *spherical* -  $\beta_2 = 0$ .

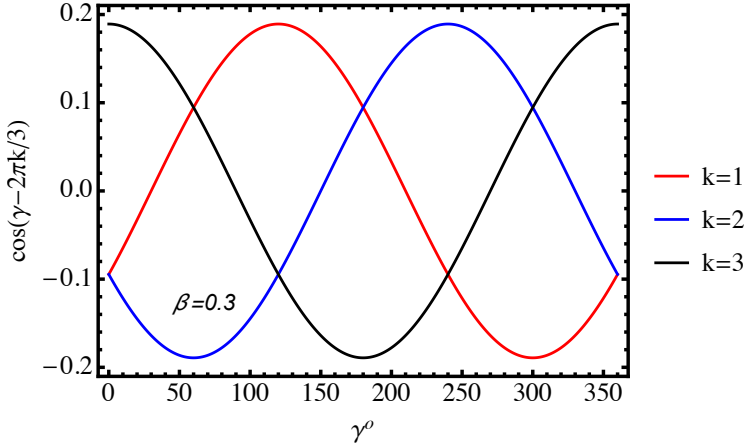


FIGURE 2.2: A graphical representation with the stretching of the nuclear axis  $\delta R_k$  for  $k = 1, 2, 3$ , corresponding to the increase in axis lengths along the  $x$ ,  $y$ , and the  $z$  directions, respectively. The representation used an arbitrary value for the quadrupole deformation  $\beta_2 = 0.3$ . Figure was reproduced according to the calculations done in [3].

The nuclear shapes that are characterized only by  $\beta_2$  (i.e.,  $\gamma = 0$ ) have shapes that correspond to spheroids. These shapes are axially symmetric, meaning that they only have one deformed axis. For the spherical case  $\beta_2 = 0$ , all three axes have the same lengths, meaning that the shape of the nucleus is in fact a sphere.

For the axially-symmetric quadrupole deformations, the parameter  $\beta_2$  can be related to the axes of the spheroid via the formula [3]:

$$\delta R_k = \sqrt{\frac{5}{4\pi}} \beta_2 \cos\left(\gamma - \frac{2\pi k}{3}\right) , \quad (2.15)$$

with  $k = 1, 2, 3$  indices that correspond to each of the three principal axes  $x'$ ,  $y'$ , and  $z'$ , respectively. The stretching of the nuclear axis in a particular direction (denoted by  $k$  in the above formula) varies according to the change in  $\gamma$ , for a fixed value of  $\beta_2$ .

Taking a look at Fig. 2.2, one can see the variations of the three axes with  $\gamma$ . When  $\gamma = 0^\circ$  the nucleus is elongated along the  $z'$  axis, but the  $x'$  and  $y'$  axes are identical (the prolate case) - axial shape. As  $\gamma$  increases, the  $x'$  axis grows, while the other two axes decrease in size, making a region with *triaxial shapes* - all three axes are unequal in magnitude. Symmetry is reached again at  $\gamma = 60^\circ$ , however the  $x'$  and  $z'$  axes are equal this time but longer than  $y'$  axis, making the nucleus look like a flattened shape (the oblate case) - axial shape. This pattern is repeated every  $\gamma = 60^\circ$ , where axial shapes emerge, with alternating prolate/oblate shapes.

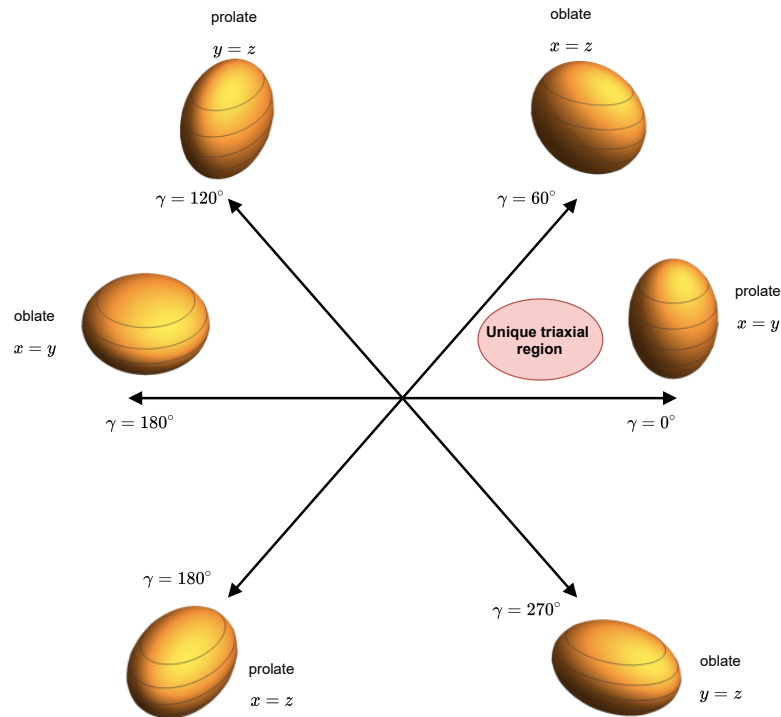


FIGURE 2.3: Beta-gamma plane divided into six regions. The first part, delimited from  $\gamma = 0^\circ$  to  $\gamma = 60^\circ$  can be considered as the representative one, while the others can be reproduced from this interval.

It is possible to summarize the various nuclear shapes that can occur with the help of a diagram within in the  $(\beta, \gamma)$  plane. The repeating pattern of the nuclear shapes is graphically represented in Fig. 2.3. One can see that the oblate axially symmetric shapes that occur at  $\gamma = 60^\circ, 180^\circ$  and  $300^\circ$  are identical, and only the axes naming scheme differs. The triaxial shapes are also repeated each  $60^\circ$ .

Regarding the characteristics of Fig. 2.3, the triaxial regions have basically identical shapes, only the axes orientations are different. Moreover, the associated Euler angles are also different, leading to the conclusion that identical physical shapes - including the space orientation - can be represented by different sets of deformation parameters  $(\beta, \gamma)$  and Euler angles.

#### 2.1.4.2 Non-Axial quadrupole deformations

Besides the nuclei characterized by a *spheroidal* shape, where two of the three principal axes have the same length and the quadrupole deformation parameter

$\beta_2$  is the key parameter that describes this kind of shapes, there are also *triaxial* nuclei (or non-axial deformed nuclei).

The triaxial shapes are defined by the  $\gamma$  degree of freedom: the parameter which describes the asymmetry between the length of the three axis of the nucleus (e.g., it describes a stretching along an axis that is perpendicular to the symmetry axis). The nuclear radius for the axially-asymmetric quadrupole deformations is given by:

$$R(\theta, \varphi) = R_0 \left( 1 + \beta_2 \cos \gamma Y_2^0(\theta, \varphi) + \frac{1}{\sqrt{2}} \sin \gamma (Y_2^2(\theta, \varphi) + Y_2^{-2}(\theta, \varphi)) \right), \quad (2.16)$$

which is different from Eq. 2.14. As it was already mentioned, the values  $\gamma = 0^\circ$  and  $\gamma = 60^\circ$  correspond to symmetric prolate and oblate shapes, respectively. Between these values, the triaxial region exist, with *maximal triaxiality* reached at  $\gamma = 30^\circ$ . The deformation parameters  $(\beta, \gamma)$  are also called the Hill-Wheeler set [6].

In Eq. 2.16, the spherical harmonics are expressed as follows:

$$\begin{aligned} Y_2^0(\theta, \varphi) &= \frac{1}{4} \sqrt{\frac{5}{\pi}} (3 \cos(\theta)^2 - 1) , \\ Y_2^2(\theta, \varphi) &= \frac{1}{4} e^{2i\varphi} \sqrt{\frac{15}{2\pi}} \sin(\theta)^2 , \\ Y_2^{-2}(\theta, \varphi) &= \frac{1}{4} e^{-2i\varphi} \sqrt{\frac{15}{2\pi}} \sin(\theta)^2 , \end{aligned} \quad (2.17)$$

and substituting these terms in  $R(\theta, \varphi)$ , Eq. 2.16 will become [1, 7]:

$$R(\theta, \varphi) = R_0 \left[ 1 + \sqrt{\frac{5}{16\pi}} \beta \left( \cos \gamma (3 \cos \theta^2 - 1) + \sqrt{3} \sin \gamma \sin \theta^2 \cos 2\varphi \right) \right]. \quad (2.18)$$

Regarding the nuclear shapes that were described in Fig. 2.3, the redundancies of the  $(\beta, \gamma)$  variables are:

- for  $\beta_2 > 0$  the nucleus is *prolate* for  $\gamma = 0^\circ, 120^\circ, 240^\circ$ .
- for  $\beta_2 > 0$  the nucleus is *oblate* for  $\gamma = 60^\circ, 180^\circ, 300^\circ$ .

- for  $\gamma = 0^\circ, 180^\circ$ , the symmetry axis is the  $z$ -axis of the intrinsic frame
- for  $\gamma = 120^\circ, 300^\circ$ , the symmetry axis is the  $x$ -axis of the intrinsic frame
- for  $\gamma = 60^\circ, 240^\circ$ , the symmetry axis is the  $y$ -axis of the intrinsic frame

#### 2.1.4.3 Lund Convention

The so-called Lund convention [7] somewhat solves this repetitiveness, by selecting a rotational axis according to the set of rules described below:

- The quadrupole deformation parameter  $\beta_2$  is always positive:  $\beta_2 \geq 0$
- The rotation around the smallest axis ( $s$ -axis) implies the constraint on the triaxiality parameter  $0^\circ \leq \gamma \leq 60^\circ$ .
- The rotation around the longest axis ( $l$ -axis) implies the constraint on the triaxiality parameter  $-120^\circ \leq \gamma \leq -60^\circ$ .
- The rotation around the medium/intermediate axis ( $i$ -axis) implies the constraint on the triaxiality parameter  $-60^\circ \leq \gamma \leq 0^\circ$ .

Fig. 2.4 aims at depicting the mechanism behind the Lund convention. The graphical representations organized in Table 2.1 show the possible nuclear shapes, depending on the number of deformation axes; namely, if there is only one deformation axis, then the nuclear shape is *axial-symmetric* (oblate or prolate) and if there are two deformation axes, then the nucleus is *triaxial* (axially-asymmetric).

#### 2.1.4.4 Alternative description of the quadrupole deformation

Considering the Lund convention and the Eq. 2.15, one can re-write the set of stretching values as follows:

$$\frac{R_x - R_0}{R_0} = \sqrt{\frac{5}{4\pi}} \beta_2 \cos \left( \gamma - \frac{2}{3}\pi \right), \quad (2.19)$$

$$\frac{R_y - R_0}{R_0} = \sqrt{\frac{5}{4\pi}} \beta_2 \cos \left( \gamma - \frac{4}{3}\pi \right), \quad (2.20)$$

$$\frac{R_z - R_0}{R_0} = \sqrt{\frac{5}{4\pi}} \beta_2 \cos \gamma. \quad (2.21)$$

$$(2.22)$$

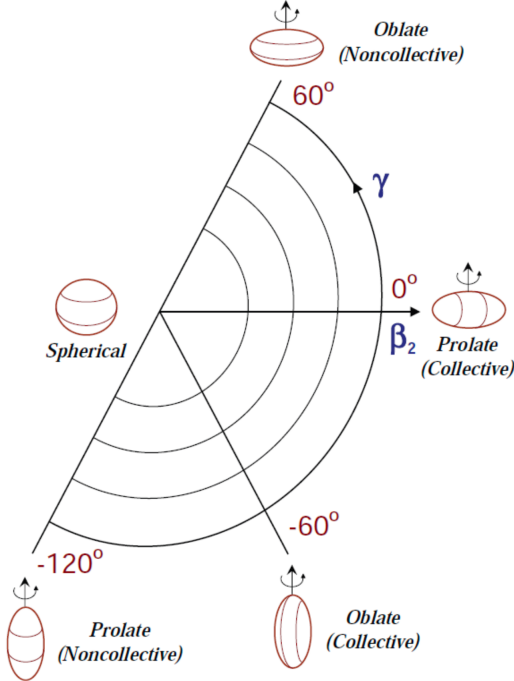


FIGURE 2.4: Representation of the nuclear shapes in the  $(\beta, \gamma)$  plane, using the Lund convention [7] previously discussed. The figure was taken from the work of Matta [8].

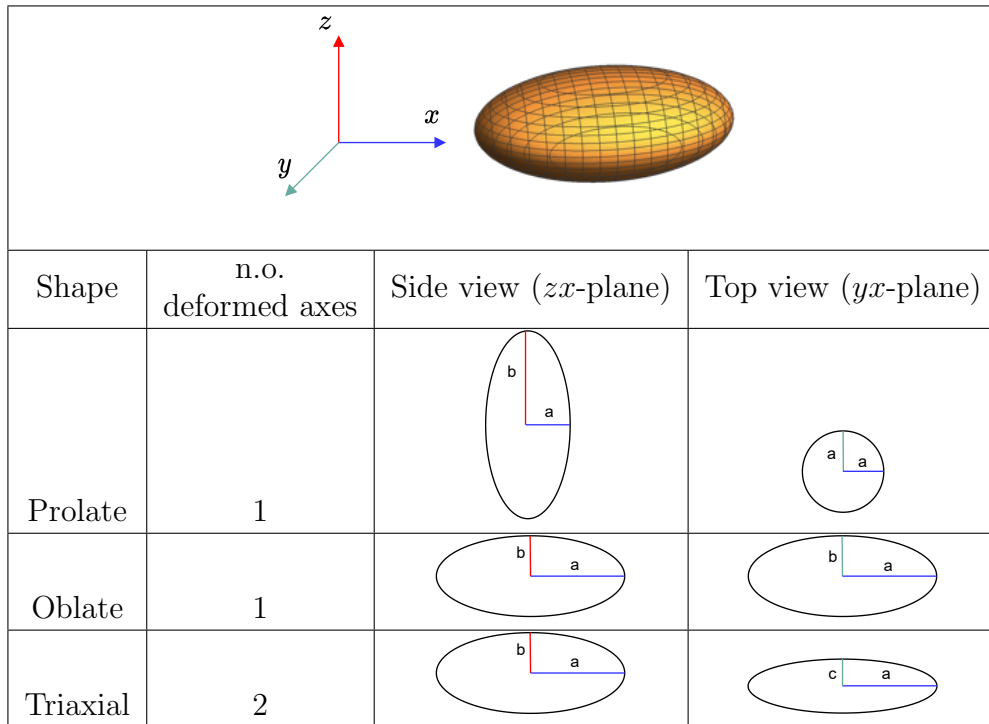
For the axially symmetric deformation (i.e.,  $\gamma = 0$ ), the quadrupole parameter  $\beta_2$  can be derived as follows:

$$\beta_2 = \frac{4}{3} \sqrt{\frac{\pi}{5}} \frac{\tilde{R}}{R_0} , \quad (2.23)$$

where  $\tilde{R} = (R_z - R_x)$  is the difference between the major ( $R_z$ ) and minor ( $R_x$ ) axes of the ellipsoid. This equation for  $\beta_2$  shows how for oblate deformations,  $\beta_2 < 0$  (implying that  $R_z < R_x$ ), while for prolate deformations  $\beta_2 > 0$  (implying that  $R_z > R_x$ ). Within literature, usual values for  $\beta_2$  range from 0.2 - 0.3 (known as *normal deformations*) to 0.4 - 0.6 (known as *superdeformations*).

Another possible description of the nuclear deformation that is specific to small deformations, is given in terms of the parameter  $\epsilon_2$ , with the connection to  $\beta_2$  via the formula [9]:

$$\epsilon_2 \approx \frac{\tilde{R}}{R_0} = \frac{3}{4} \sqrt{\frac{5}{\pi}} \beta_2 = 0.946 \beta_2 . \quad (2.24)$$



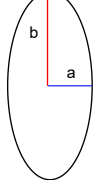
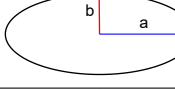
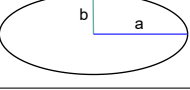
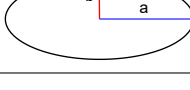
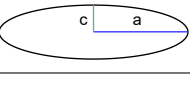
Shape	n.o. deformed axes	Side view ( $zx$ -plane)	Top view ( $yx$ -plane)
Prolate	1		
Oblate	1		
Triaxial	2		

TABLE 2.1: Deformed ellipsoidal shapes of the nuclei. A generic ellipsoid is shown at the top of the table. The parameters  $a$ ,  $b$ , and  $c$  represent lengths of differing magnitude of the nuclear ellipsoid.

### 2.1.5 Nuclear Shapes and Softness

Regarding Table 2.1, a discussion about the implications of the nuclear shapes in terms of some specific phenomena is necessary. Indeed, the shell-model (which will be briefly discussed in the next chapter) considers the motion of the individual nucleons, that are *confined* in nucleonic orbitals, where each nucleon will occupy an orbit with a quantized value of angular momentum. The interpretation of the gamma-ray spectra of different nuclei can be properly described through the excitations if individual nucleons between different orbits, but only for nuclei that are near closed shells. Unfortunately, the same cannot be said about nuclei that lie far from a shell closure, where tools like *Collective Model - C.M.* [1] help understand the properties of these nuclei. One can see that any additional nucleon to the closed shells will imply a departure from the spherical view of a nucleus, with deformations along one of the axes of that nucleus. With the help of C.M., the energy spectrum of many nuclei can be understood and described in terms of 1) a rotation around an axis that is perpendicular to the deformation axis, but also in terms of a 2) motion of the nucleus as a whole (i.e., collective behavior) in tandem

with one coming from a single nucleon (i.e., single-particle behavior). As an example, nuclei in the region  $N = 82$  were extensively studied, and the properties of a given nuclide are not only determined by the specific orbital occupied by valence nucleons (e.g., proton orbitals such as  $s_{1/2}$ ,  $h_{11/2}$  or neutron orbitals such as  $f_{7/2}$ ,  $h_{9/2}$ ), but also the proportion of each shell that is filled with protons and neutrons, respectively. The nuclei in this closed shell  $N = 82$  region are considered as perfect examples of evolutions from the single-particle motion, and the evolution to a collective behavior can be emphasized around the *midshell* at  $N = 104$ . These midshell nuclei have a deformation that is present along only one axis: *axially symmetric*. Every orbital will cause the nucleus to change its shape towards either a prolate or an oblate one. The change in prolate/oblate type of deformation will depend on the value of the quadrupole moment [10], quantity used to evaluate the so-called Nilsson levels [11] (a detailed discussion about the Nilsson orbitals will be made in the following chapter), or Nilsson diagrams: single-particle energies as a function of nuclear deformation. The slope of a Nilsson level is related to the expectation value of the quadrupole moment, via the expression [7]:

$$\frac{de_k}{d\beta} = - \langle j | q | j \rangle \quad (2.25)$$

with  $e_k$  representing the energy of the single-particle state  $|j\rangle$ ,  $\beta$  is the deformation, and  $q$  is the quadrupole operator. Each nucleon that occupies an orbit with a given slope will contribute to an overall deformation: one nucleon that occupies a downward sloping orbital which for positive  $\beta$  will drive the nucleus to a prolate shape, while the other type of nucleon that occupies an upward sloping orbital will drive the nucleus to an oblate shape. The competition between these two polarizing effects will result in the axial asymmetry.

In triaxial nuclei (*axially-asymmetric*), a number of low-lying nuclear configurations can exist, leading to different shapes. When the nucleus has a dynamic degree of triaxiality (via the  $\gamma$  deformation parameter), it is said to be a  *$\gamma$ -soft nucleus*.

The  $\gamma$ -soft nuclei tend to exist when both the protons and neutrons occupy the top and bottom of their shells, respectively. The opposite also holds true [12]. The conditions for  $\gamma$ -soft nuclear deformations are realized, for example, in  $N \approx 90$  nuclei, where the Fermi surfaces are located near the top of the proton shell ( $h_{11/2}$ ) and bottom of the neutron shell ( $i_{13/2}$ ).

It is interesting that a single nucleus does not necessarily holds a single fixed shape. If the potential energy surface (PES) is relatively flat with respect to the triaxiality parameter  $\gamma$  (meaning that there is no constrain with regards to the minimum value of  $\gamma$ ), the shape can oscillate within an interval of deformation. Such a feature characterizes the  $\gamma$ -softness of the nucleus itself.

# Chapter 3

## Nuclear Models

### 3.1 Introduction

In the following, it is worth to make a discussion about the nuclear models that are used by theoreticians in order to describe phenomena that are specific to rotating nuclei and high-spin regime. Since the focus of this work emerges from a *class* of properties that usually apply to the high-spin region (but this does not necessarily also imply a high-energy region), it makes sense to give an insight in the tools that fit the best the underlying effects.

### 3.2 Shell model

The fact that an atomic nucleus can have a structure that behaves rather similarly as its *parent* (i.e., the atom) in terms of changing the number of constituents, has been enforced by the experimental observations that were done across time. The sharp and discrete discontinuities of nuclear properties, such as the nucleon separation energy, point to the fact that nucleus can be explained through the existence of *shells*. Some examples of observations which indicate this are:

- When adding a nucleon to a nucleus, there are certain places where the *binding energy* of the next nucleon becomes considerably smaller than the previous one.

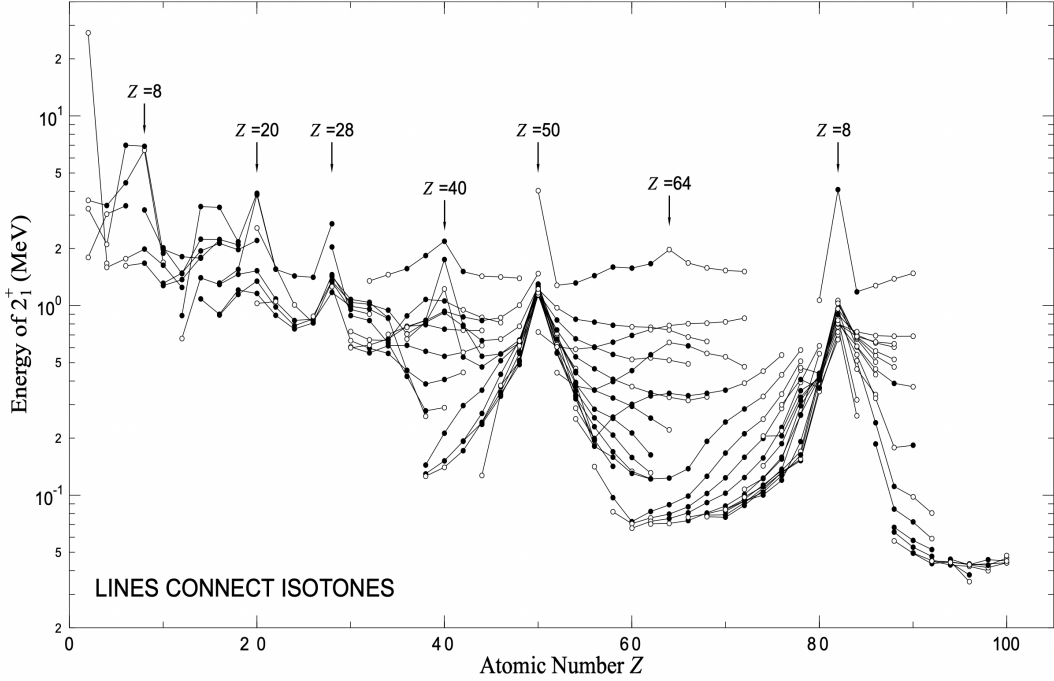


FIGURE 3.1: The first excited energy states  $2^+$  of nuclei with even  $Z$  and  $N$  graphically represented with respect to the proton number. Each line represents a set of isotopes. Figure taken from Ref. [8].

- Separation energies for both the protons and neutrons suffer drastic changes, having strong deviations from the predictions of the semi-empirical mass formula [13], the discontinuities being represented by major shell closures (complete filling) [14].
- The neutron absorption cross-section has a substantial decrease in value at the neutron magic numbers
- Great abundance of nuclides where  $Z$  and  $N$  are magic numbers.

The sudden discontinuities occur at specific values of the proton  $Z$  and neutron  $N$  numbers: these are called *magic numbers*. Currently, these magic numbers correspond to  $Z$  or  $N = 2, 8, 20, 28, 50, 82, 126$ , and they represent the so-called major shells. There are also two *weakly magic numbers*: 40 and 64.

One can examine the values for the first excited states  $2^+$  that are shown in Figs. 3.1, 3.2. Indeed, these values show some peaks, each peak corresponding to a particular magic number. This results are part of the work of Raman et al [15], where the transition probabilities from the ground state to the first-excited  $2^+$  state in even-even nuclei were evaluated.

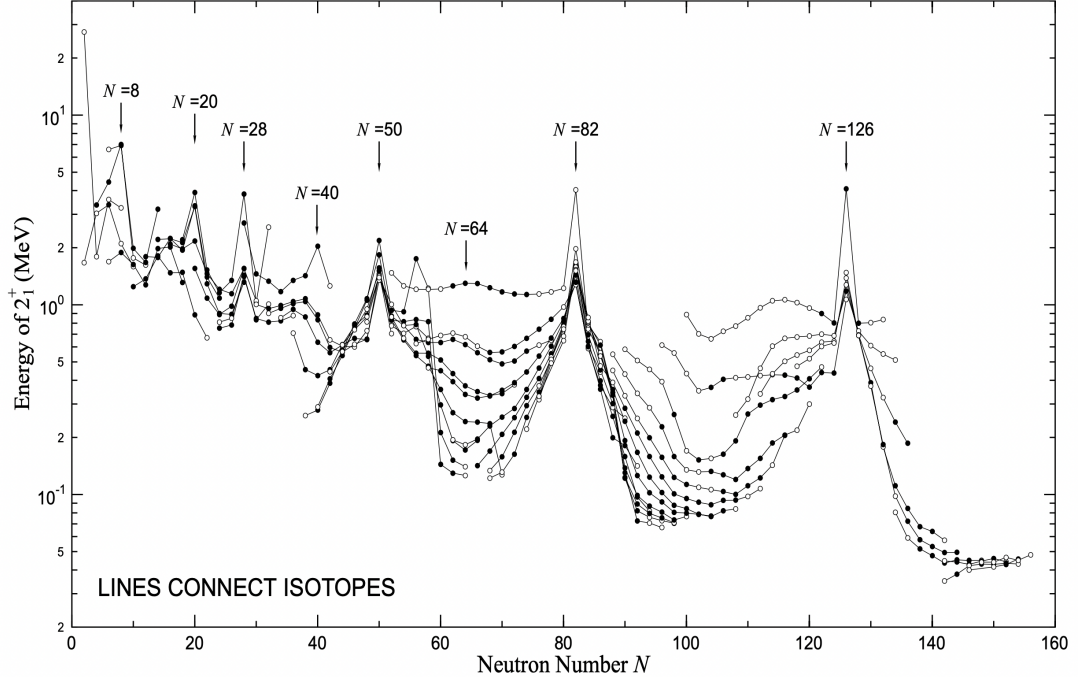


FIGURE 3.2: The first excited energy states  $2^+$  of nuclei with even  $Z$  and  $N$  graphically represented with respect to the neutron number. Each line represents a set of isotopes. Figure taken from Ref. [8].

The shell model starts from the basic assumption that the nucleus is a *mean-field potential*, that is a potential for which the motion of a single nucleon is caused by all the other nucleons (the nucleon is moving inside an average potential generated by all the other constituents of the nucleus). Of course, all the nucleons that are under the influence of such a mean field potential occupy the energy levels which correspond to a series of (sub)shells that agree with the Pauli exclusion principle. Having a general expression for the potential that properly reproduces all the magic numbers (and the observed nuclear properties) is the main goal.

Since the model starts from the concept of independent (non-interacting) particle motion within an average potential, finding each energy will be equivalent of solving the Schrödinger equation:

$$-\frac{\hbar^2}{2m} \nabla^2 \psi_i(r) + V(r) \psi_i(r) = e_i \psi_i(r) \quad (3.1)$$

where  $e_i$  represents the energy (eigenvalue) and  $\psi_i$  represents the wave-function (eigenstates), while  $V(r)$  is the nuclear potential whose expression must be evaluated.

The choice of  $V(r)$  will be dictated by the reproduction of various experimental

data (such as nuclear saturation, scattering, nuclear reactions, and so on). For the motion of an independent particle, an obvious first attempt would be the *simple harmonic oscillator* (SHO), which has the known expression:

$$V(r) = \frac{1}{2}m(\omega_i r)^2 , \quad (3.2)$$

with  $\omega_i$  as the frequency of the basic harmonic-like motion of the particle in the nucleus. With Eq. 3.2, the motion of the nucleon has a straightforward expression:

$$\frac{\hbar^2}{2m}\nabla^2\psi_i(r) + \frac{1}{2}m(\omega r)^2\psi_i(r) = e_i\psi_i(r) . \quad (3.3)$$

This Schrödinger equation has its energy eigenvalues under to form:

$$e_N = \left(N + \frac{3}{2}\right)\hbar\omega , \quad (3.4)$$

where  $N$  is the number of oscillator quanta which describes each major shell (also called the *principal quantum number*). One should keep in mind that such an expression is typical for a three-dimensional and isotropic harmonic oscillator. The principal quantum number  $N$  is furthermore defined as:

$$N = 2(n - 1) + l , \quad (3.5)$$

with  $n$  and  $l$  being the *radial* quantum number and *orbital angular momentum* quantum number, respectively, taking values  $n = 1, 2, 3, \dots$  and  $l = 0, 1, 2, \dots, n - 1$ . In this first approximation, all the levels with the same principal quantum number  $N$  are *degenerate*, with a maximal degeneracy given by  $2(2l+1)$ . However, by using only the SHO term as the expression of  $V(r)$ , only the first three magic numbers are reproduced, meaning that some additional term(s) might be needed in order to consistently obtain the series of magic numbers.

A next step is to use the fact that the experimentally observed short range of the strong nuclear force: the steepness of the SHO can be corrected with an *attractive* term proportional to  $l$ -squared. This acts as a centrifugal term which provides an angular momentum barrier, lifting the degeneracy between the levels with the same principal quantum number  $N$  and different values for the orbital angular momentum  $l$ . This SHO+ $l^2$  step is still not enough though. The last step is to add a so-called *spin-orbit* coupling term of the form  $\vec{l} \cdot \vec{s}$ . This term comes from the

consideration that the nucleon-nucleon interaction has a spin dependence, and the potential depends on the intrinsic spin  $s$  ( $\vec{s}$ ) and the orbital angular momentum  $l$  ( $\vec{l}$ ) of a nucleon. Since  $\vec{j} = \vec{l} + \vec{s}$ , two possible states emerge from a single value of  $l$  (depending on whether  $\vec{s}$  is parallel or anti-parallel to  $\vec{l}$ ). The final expression of the terms SHO+ $\vec{l}^2$ + $\vec{l} \cdot \vec{s}$  will consist in the *Modified Harmonic Oscillator* (HMO).

$$V(r) = \frac{1}{2}(\omega r)^2 + B \vec{l}^2 + A \vec{l} \cdot \vec{s}. \quad (3.6)$$

For the sake of simplicity, the centrifugal term will be denoted within formulas without the vector symbol. Since the intrinsic spin of a nucleon is  $s = 1/2$ , for a given value of  $l$ , there can be two values for the *total angular momentum* (a.m.)  $j = l \pm 1/2$ : one for each spin orientation with respect to the direction of the orbital a.m. Moreover, for each value of  $l = 0, 1, 2, 3, 4, \dots$ , there is a similar notation  $l = s, p, d, f, g, \dots$ , respectively. Regarding the spectroscopic notation, usually, the value of  $j$  is considered as a subscript;  $nl_j$  (for example  $1p_{1/2}$  and  $1p_{3/2}$ ). What it is worth mentioning is that for high enough shells, there can be splittings between  $j + 1/2$  and  $j - 1/2$  that are large enough to lower the  $j + 1/2$  state from one oscillator shell  $n$  to one located below  $n - 1$ . These types of levels are called *intruder states* and they have opposite parity  $\pi = (-1)^l$  with respect to the shell that these levels will occupy.

Going back to the expression of the  $\vec{l} \cdot \vec{s}$  term from Eq. 3.6 and denoting it with  $V_{ls}(r)$ , it is shown by Casten [9] that its contribution to the total potential can be regarded as a surface effect. Due to this, its form can be expressed as a function that depends on the radial coordinate as such [9]:

$$V_{ls}(r) = -a_{ls} \frac{\partial V(r)}{\partial r} \vec{l} \cdot \vec{s}, \quad (3.7)$$

where  $V(r)$  is the expression for a central potential and  $a_{ls}$  is a strength constant.

Now that an expression for the nuclear potential that is able to reproduce all the magic numbers has been formulated, it is also possible to formulate the total energy of a single-particle within the average potential that is generated by all the other nucleons within the nucleus. Thus, the Hamiltonian of this simple system

(the modified oscillator) can be formulated as such:

$$\begin{aligned} H &= -\frac{\hbar^2}{2m}\nabla^2 + V_{\text{SHO}} + (l^2)_{\text{term}} + (\vec{l} \cdot \vec{s})_{\text{term}} = -\frac{\hbar^2}{2m}\nabla^2 + V_{\text{MHO}}, \\ H &= -\frac{\hbar^2}{2m}\nabla^2 + \frac{1}{2}m(\omega r)^2 + Bl^2 + A\vec{l} \cdot \vec{s}. \end{aligned} \quad (3.8)$$

The evolution from each term in the shell-model potential (that is the first approximation as a SHO, then SHO+ $l^2$ , and finally SHO+ $l^2 + \vec{l} \cdot \vec{s}$  or modified oscillator potential) is illustrated in Fig. 3.3, where it can be seen how each extra term introduces a new degeneracy within the energy states, with the complete reproduction of the magic numbers in the third column. Moreover, the *intruder* levels can be observed, where levels with  $j = l + 1/2$  from a particular  $n$  are so low, that they lie below an  $n - 1$  adjacent level.

Another, more realistic potential that can be used in order to reproduce the specific shell model calculation is the so-called Woods-Saxon potential. Because of the short-range character of the strong nuclear force, it is safe to assume that this potential should behave in the same manner as the density distribution of the nucleons. Since for medium and heavy nuclei, the Fermi-like functions (distributions) are the ones that best fit the experimentally measured data, this potential should have the following form [16]:

$$V_{\text{ws}}(r) = -\frac{V_0}{1 + e^{\frac{r-R_0}{a}}}. \quad (3.9)$$

This mean-field potential contains the terms  $V_0$  that represents the depth of the potential ( $\approx 50$  MeV, in order to reproduce the experimental separation energies for the nucleons), the surface thickness  $a$  (also called the diffuseness parameter, giving information about how fast the potential drops to zero) with a value of approximately 0.5 fm, while  $R_0$  is the nuclear radius with  $R_0 = r_0 A^{1/3}$  and  $r_0 = 1.2$  fm. The nature of this potential is of *central type* and, unfortunately, Eq. 3.9 in its pure form is not enough the reproduce the higher magic numbers. As such, the addition of a spin-orbit term, similarly as in the case of MHO potential, is required [17]:

$$V_{\text{total}} = V_{\text{ws}}^{\text{central}} + V_{ls}(r)\vec{l} \cdot \vec{s}. \quad (3.10)$$

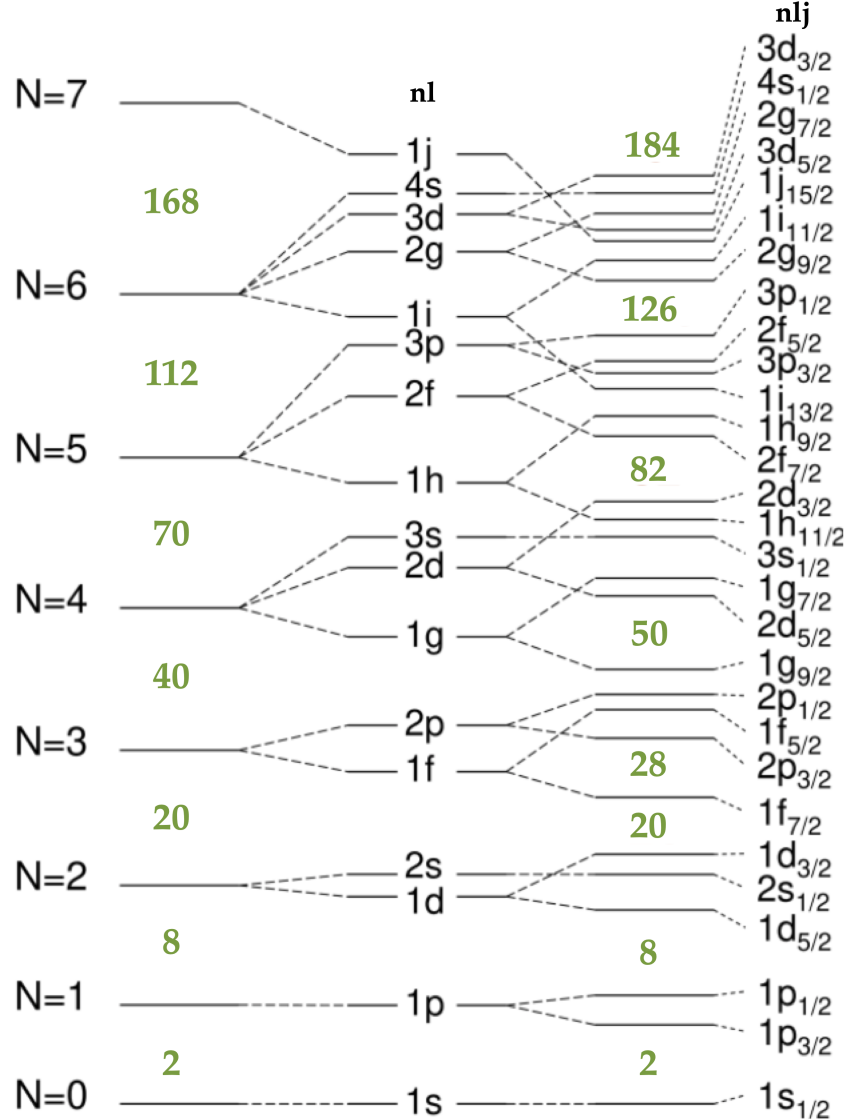


FIGURE 3.3: The energy levels obtained via calculation of the shell model potential using the simple oscillator (SHO), the SHO amended with a centrifugal term  $l^2$ , and finally the modified oscillator (MHO) that contains a spin-orbit term. The ‘correct’ magic numbers are the ones in the right-most column.

Figure is adapted from Refs. [8],[14].

The only good quantum numbers in the case of the WS potential are the total a.m.  $j$  and the parity  $\pi = (-1)^l$ . The expectation value of the spin-orbit term  $\vec{l} \cdot \vec{s}$  can be given as:

$$\langle ls \rangle = \hbar^2 \begin{cases} \frac{l}{2} & \text{for } j = l + \frac{1}{2} \\ -\frac{l+1}{2} & \text{for } j = l - \frac{1}{2} \end{cases}. \quad (3.11)$$

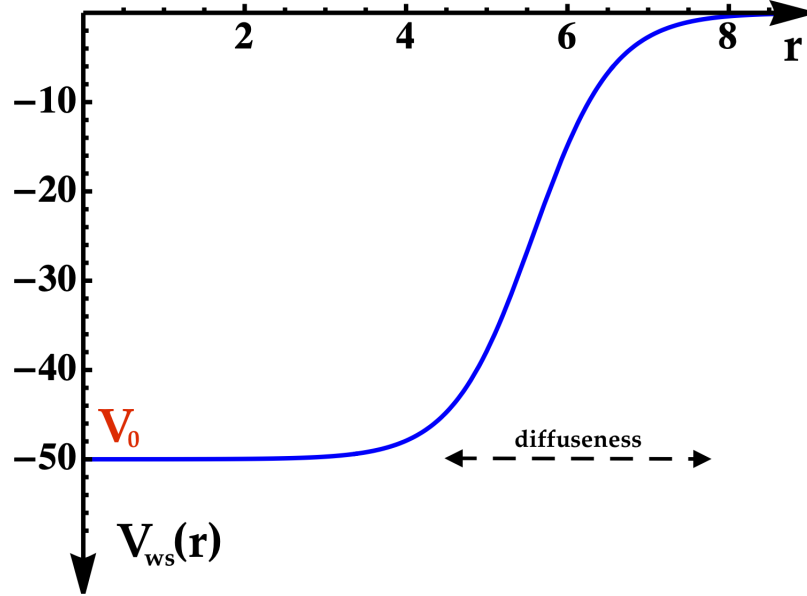


FIGURE 3.4: The shape of the Woods-Saxon potential, defined by Eq. 3.9. The parameters are arbitrarily chosen as:  $V_0 = 50$  MeV,  $R = 5.57$  fm, and  $a = 0.5$  fm.

and the spacing between two levels can be furthermore expressed as [17]:

$$\Delta E_{ls} = \frac{2l+1}{2} \hbar^2 \langle V_{ls} \rangle . \quad (3.12)$$

The experimental evidence points to the fact that  $V_{ls}(r)$  is negative, meaning that states with  $j = l - 1/2$  are shifted higher than  $j = l + 1/2$ . Some characteristics of the WS potential are the following:

1. It increases with the increase of  $R$ , meaning that it has an *attractive nature*
2. It flattens out for large enough  $A$  in the center of the nucleus
3. It rapidly goes to zero as  $R$  increases (given by the diffuseness parameter), indicating its short-range nature
4. When  $R = R_0$  (that is for the nucleons near the surface), a large force towards the center of the nucleus is experienced by the these nucleons.

Fig. 3.4 shows the shape of a typical Woods-Saxon potential. Aiming at a final Hamiltonian which describes the motion of the nucleon within the mean-field

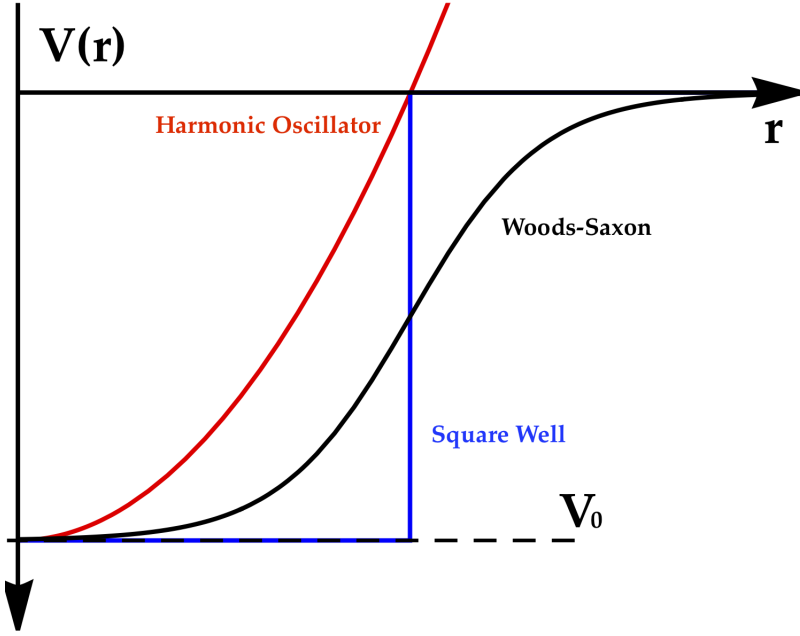


FIGURE 3.5: A schematic representation with the three kind of potentials used to describe the shell model: harmonic oscillator, Woods-Saxon, and for completeness, the square-well.

potential, the formula can be readily obtained:

$$H = -\frac{\hbar^2}{2m} \nabla^2 + V_{ws}^{\text{central}} + (\vec{l} \cdot \vec{s})_{\text{term}}, \quad (3.13)$$

$$H = -\frac{\hbar^2}{2m} \nabla^2 - \frac{V_0}{1 + e^{\frac{r-R_0}{a}}} + A \vec{l} \cdot \vec{s}. \quad (3.14)$$

In addition to the shape of the Woods-Saxon potential, a comparison between it, a SHO, and the square-well-like potential is made in Fig 3.5.

The difference between the pure form of the Woods-Saxon potential and the total potential, where the spin-orbit contribution is amended, can be seen in Fig. 3.6.

So far, the general discussion concerning the nuclear models was for the case where each nucleon is treated as an *independent* particle moving in an average potential (mean-field potential) which represents an *effective* interaction of all the other nucleons with the nucleon under study. However, such an assumption is not accurate enough (especially for the nuclei that lie far away from the closed shells), and this problem should be treated within a *many-body* approach: considering the mutual interaction between the nucleons. These interactions are also called *residual interactions* [9, 18]. With these residual interactions, an accurate depiction of the nucleus might be achieved, and in the following sections, the *Deformed Shell Model*

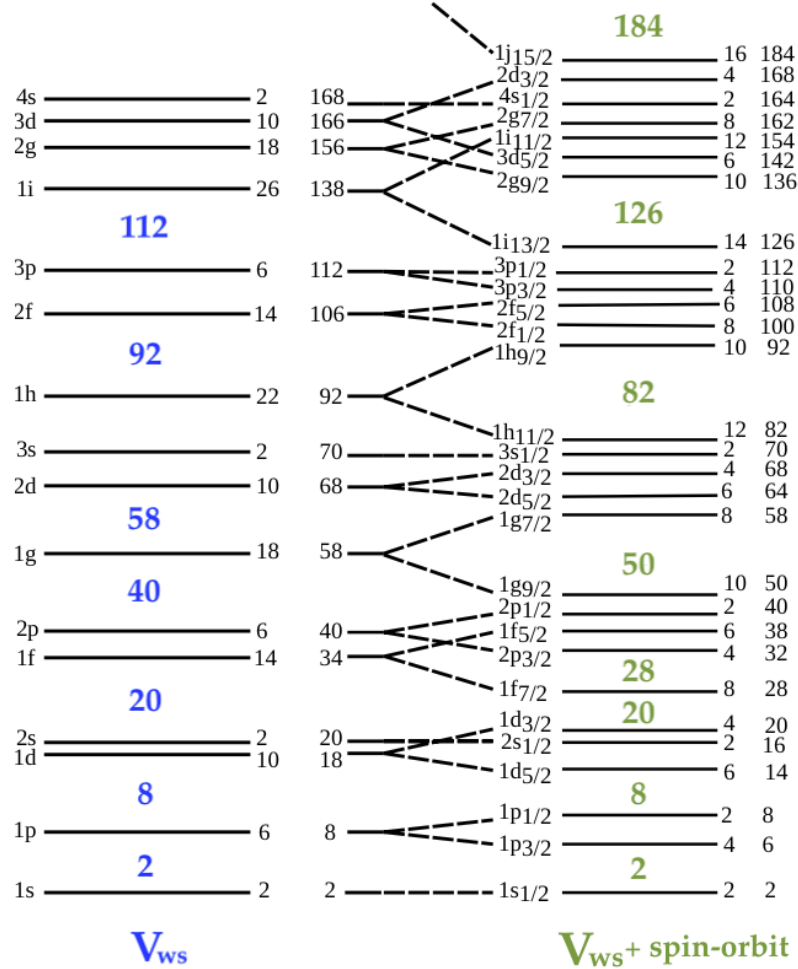


FIGURE 3.6: The left side represents the energy levels calculated for the Woods-Saxon potential given by Eq. 3.9, and the right side shows the single-particle energies with the spin-orbit correction added, as in Eq. 3.10. Figure adapted from Ref. [10].

will be employed, reaching to the famous Nilsson model/theory of describing the nucleus.

### 3.3 Deformed Shell Model

In the previous section, the discussion was focused on an approximate description of the (independent) motion of a nucleon within an average potential. That potential is generated by the interaction of that nucleon with all the remaining

nucleons within the compounding nucleus. Indeed, for spherical nuclei, the model described previously works really well and it is a successful tool in reproducing and predicting the properties of nuclear states, especially if the excited states have nucleonic configurations that are dominated by a single nucleon or a very small number of ‘extra’ nucleons.

For nuclei that are even in both the proton number and the neutron number (i.e., even-even nuclei), the nuclear ground-state has a spin and parity that are properly reproduced by the *spherical shell model*:  $I^\pi = 0^+$ . In a nucleus with complete shells, the *net spin* must be zero while for the nucleus with one nucleon missing from a complete shell closure (a hole), that ground-state spin should equal to the total a.m.  $j$  value of the orbital which that particular hole is occupying. Moreover, the parity of the ground-state for a given nucleus is determined by the orbital a.m. value  $l$ :

$$\pi = (-)^l \rightarrow \begin{cases} +1 & \text{for even-}l \text{ levels} \\ -1 & \text{for odd-}l \text{ levels} \end{cases}. \quad (3.15)$$

For odd-odd nuclei, one can find the ground-state (g.s.) spin and parity via the coupling of the spin and parity of the last two valence nucleons [14, 18]. The coupling rules that are allowed in the odd-odd nucleus were determined more than 50 years ago by Gallagher et al. [19]:

$$I = j_p + j_n \text{ if } j_p = l_p \pm \frac{1}{2} \text{ and } j_n = l_n \pm \frac{1}{2}, \quad (3.16)$$

$$I = |j_p - j_n| \text{ if } j_p = l_p \pm \frac{1}{2} \text{ and } j_n = l_n \mp \frac{1}{2}. \quad (3.17)$$

### 3.3.1 Deformed Shell Model - Nilsson Model

The idea that some nuclei are deformed in their ground-state was enforced experimentally a long time ago by measuring quantities such as density distributions, nuclear quadrupole moments [9] and so on. The non-spherical shapes are given by the existence of nucleonic configurations that lie away from the major shell closure. In Chapter 2 the description of the nuclear shapes was treated, using the well-known formula for the parametrization of the nuclear radius in terms of the collective coordinates (see Eq. 2.1), resulting in the known nuclear shapes:

*spherical, axially-symmetric* (that is prolate or oblate), and *axially-asymmetric* (or triaxial).

Developed by Nilsson in 1955 [20] for treating the *deformed nuclei* proved to be a big pillar within the nuclear community, especially for the study of medium and heavy nuclei. In essence, this tools is a modified shell model which allows for deformations to be taken into account by the use of the *anisotropic harmonic oscillator* (AHO). Similarly as for the basic shell model, the goal is to obtain an expression for the single-particle energies of a nucleon. The basic Hamiltonian corresponding to this kind of system is shown below [18]:

$$H = H_0 + a_1 \vec{l} \cdot \vec{s} + a_2 l^2 , \quad (3.18)$$

where  $H_0$  is a Hamiltonian for the AHO. The general expression for this kind of oscillator is of the form:

$$H_{\text{AHO}} \equiv H_0 = -\frac{\hbar^2}{2m} \nabla^2 + \frac{1}{2} m(\omega_x^2 x^2 + \omega_y^2 y^2 + \omega_z^2 z^2) . \quad (3.19)$$

In the general expression of the single-particle Hamiltonian, the constants  $a_1$  and  $a_2$  are usually determined via adjustments to the experimental results. It can be seen that the centrifugal-like term  $l^2$ , which simulates a flattening of the oscillator potential, and the  $\vec{l} \cdot \vec{s}$  term are still present here, as it was the case for the spherical shell model. However, the explicit form of Eq. 3.18 is as follows:

$$\begin{aligned} H_{\text{Nil}} = & -\frac{\hbar^2}{2m} \nabla^2 + \frac{1}{2} m(\omega_x^2 x^2 + \omega_y^2 y^2 + \omega_z^2 z^2) - 2\kappa\hbar\omega_0(\vec{l} \cdot \vec{s}) \\ & - 2\kappa\hbar\omega_0\mu(l^2 - \langle l^2 \rangle_N) . \end{aligned} \quad (3.20)$$

Obviously, the parameters  $\kappa$  and  $\mu$  act as strength parameters for the spin-orbit coupling term and the centrifugal term, respectively. The last term is a correction, which was originally considered as  $\mu l^2$ , but it was pointed by Gustafson et al. [21] that the shift in energy is way too large for big values of  $N$  (principal quantum number). As a result, taking the current expression for the correction term helps to compensate. The three *oscillator frequencies* are chosen to be inversely proportional to the semi-axis lengths of the deformed ellipsoid (denoted by  $a_x$ ,  $a_y$ , and  $a_z$ ) such that:

$$\omega_r = \omega_0 \frac{R_0}{a_r} , \quad r = x, y, z . \quad (3.21)$$

For the spherical case, the oscillator frequency  $\hbar\omega_0$  is set to  $41A^{-1/3}$  MeV (calculation for this value arise from the shell model with SHO [18]). For the axially-symmetric case, one can choose the  $z$ -axis as symmetry axis, implying that the oscillator frequencies along the  $x$  and  $y$  axes are equivalent (that is  $\omega_x = \omega_y \equiv \omega_{\perp}$ ).

Following the calculations done in [18], one can express the two relevant oscillator frequencies in terms of a deformation parameter  $\epsilon_2$  (whose dependence on the quadrupole deformation parameter  $\beta_2$  has been shown in Eq. 2.24) as such:

$$\omega_{\perp}^2 = \omega_0^2 \left(1 + \frac{2}{3}\epsilon_2\right) , \quad (3.22)$$

$$\omega_z^2 = \omega_0^2 \left(1 - \frac{4}{3}\epsilon_2\right) . \quad (3.23)$$

Moreover, a dependence on the deformation parameter itself is employed for the frequency  $\omega_0$  that appears in the expressions for  $\omega_{\perp}$  and  $\omega_z$ , respectively:

$$\omega_0 = \left(1 - \frac{4}{3}\epsilon_2^2 - \frac{16}{27}\epsilon_2^3\right)^{-1/6} , \quad (3.24)$$

where  $\bar{\omega}_0$  can be considered a constant written as  $\bar{\omega}_0 = (\omega_x\omega_y\omega_z)^{1/3} = \text{const}$  (coming from the harmonic oscillator at zero deformation and also considering the conservation of the nuclear volume).

The energy eigenvalues  $\epsilon_q$  for the nucleonic state  $\psi_q$  belonging to a deformed nucleus can be determined within the Nilsson model by solving the Schrödinger equation associated to each nucleon in particular:

$$H_{\text{Nil}}\psi_q = \epsilon_q\psi_q , \quad (3.25)$$

where the index  $q$  denotes a set with all the relevant quantum numbers. This set is also called the *asymptotic quantum numbers*, and they are used to specify a *Nilsson orbital*. The well-known notation is as follows (still considering the  $z$ -axis as the symmetry axis):

$$\Omega^{\pi} [Nn_z\Lambda] . \quad (3.26)$$

- $\Lambda$  is the projection of the particle's orbital a.m. along the symmetry axis (component of  $l$  along  $z$ )

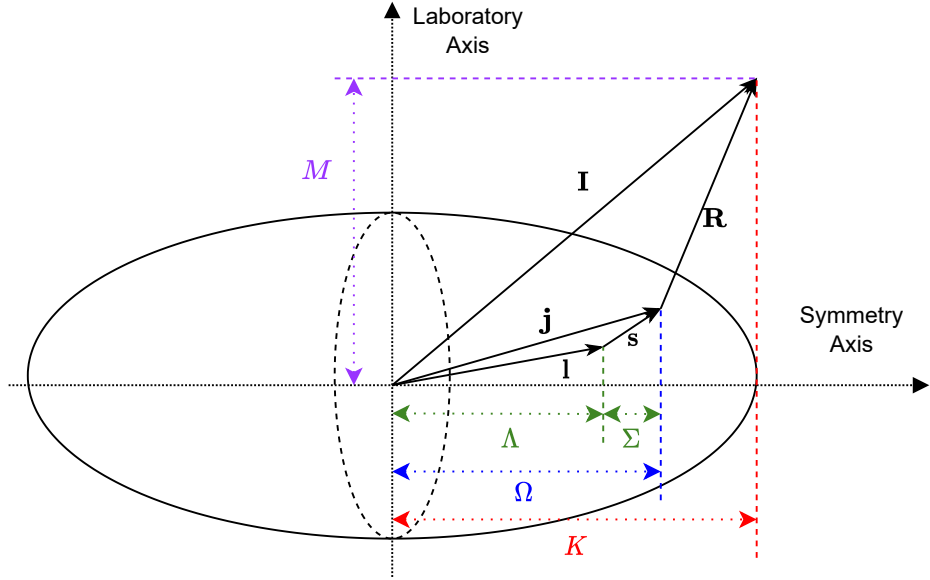


FIGURE 3.7: A schematic drawing that shows the geometrical interpretation of the Nilsson asymptotic quantum numbers (see text). This figure is inspired from Ref. [22]

- $N$  the principal quantum number of the major shell. It also determines the parity as  $\pi = (-1)^N$ , making the notation from Eq. 3.26 somewhat redundant in terms of explicitly specifying it
- $n_z$  is the number of oscillator quanta along the symmetry axis. More precisely, it gives the number of nodes for the wave-function of that particle along the direction of the  $z$ -axis
- $\Omega$  is the projection of the particle's total a.m. along the symmetry axis (i.e.,  $\mathbf{j}$ ). Moreover, the projection of the intrinsic spin of a nucleon onto the symmetry axis can have the values  $\Sigma = \pm \frac{1}{2}$ , so that  $\Omega = \Lambda + \Sigma = \pm \frac{1}{2}$ .

Fig. 3.7 shows the geometrical meaning of the asymptotic quantum numbers for the Nilsson model. Indeed, for a single nucleon orbiting a deformed core, the vector  $\mathbf{R}$  represents the angular momentum of a *rotating nucleus* (having a collective character, since it emphasizes the motion of the nucleus as a whole), the vector  $\mathbf{I}$  represents the total a.m. of the entire nucleus,  $\mathbf{j}$  is the total a.m. of the single-particle (that is  $\mathbf{j} = \mathbf{j} + \mathbf{s}$ ). However, two more quantum numbers should be mentioned: the projection of the total a.m.  $\mathbf{I}$  onto the symmetry axis, denoted by  $K$ , and the projection of the same vector onto the laboratory axis, referred to as  $M$ .

Regarding the quantum numbers sketched in Fig. 3.7, there is an important aspect which needs to be specified about the two projections  $K$  and  $\Omega$ , respectively, since it would make the understanding of the orbital motion of nucleons more concise. Indeed, it is clear that compared to the spherical case, where different orientations are irrelevant to the energy spectrum of nucleons, here in the deformed case, different directions in space lead to different energies. The orientation is in fact specified by the *magnetic sub-state* of the nucleon, i.e., the projection of the total angular momentum on the symmetry axis. This projections is denoted by  $\Omega$  for the single-particle, however, because the rotational angular momentum  $\mathbf{R}$  in the axially deformed is perpendicular to the symmetry axis for low-lying states, then it will have no contribution to  $K$ , meaning that one can use  $\Omega$  and  $K$  interchangeably.

### 3.3.2 Single-particle states in deformed nuclei

It is instructive to go into detail about the quantum numbers defined in Eq. 3.26 since the orbits which characterize the nucleons with such numbers help to point out the nature of nuclear deformations that take place.

The quantum numbers  $N$ ,  $n_z$  and  $\Lambda$  are good quantum numbers only when the nuclear deformation is large, meaning that  $\epsilon$  (or equivalently  $\beta$ ) tends to infinity: also the reason why they are called asymptotic quantum numbers. However, the numbers  $\Omega$  and  $\pi$  remain good quantum numbers even for low and moderate deformations for the nucleus. It should be noted that if  $N$  is even, then  $(\Lambda + n_z)$  is also even. Similarly, if  $N$  is odd, then the sum of the other two quantum numbers must also be odd [9].

Since the eigenvalues of the Hamiltonian  $H_{\text{Nil}}$  ultimately depend on the deformation parameter  $\epsilon$ , each nucleon will have an orbit (energy) that is deformation dependent. At no deformation (i.e., the spherical case), all the energy levels for a single-particle state will have a  $2j + 1$  degeneracy. This translates to the fact that all  $2j + 1$  possible orientations of  $\vec{j}$  are equivalent, when referring to any arbitrary axis of choice. On the other side, when the potential is deformed, this will no longer hold: the energy levels in the deformed potential will depend on the spatial orientation of the orbit itself: the energy depends on the component of  $\vec{j}$  along the symmetry axis of the core.

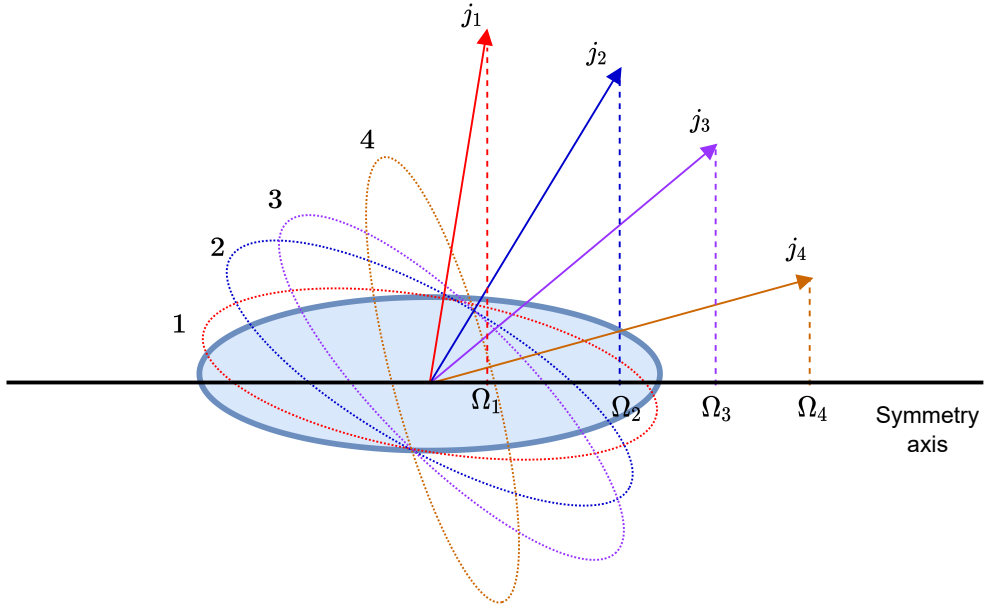


FIGURE 3.8: A simple sketch showing the single-particle orbits for the  $j = 7/2$  nucleonic state, along the symmetry axis for a *prolate* deformation. The actual projections are  $\Omega_1 = \frac{1}{2}$ ,  $\Omega_2 = \frac{3}{2}$ ,  $\Omega_3 = \frac{5}{2}$ , and  $\Omega_4 = \frac{7}{2}$ . The figure was inspired from Ref. [14].

As an example, a nucleon from the  $f_{7/2}$  shell will be considered. This nucleon can have eight possible components for  $\vec{j}$ , this is the range  $\Omega = [-\frac{7}{2}, \frac{7}{2}]$ . Because of the reflection symmetry for nuclei for either of the two possible directions of the symmetry axis, the positive components of  $\Omega$  will have the same energy as the negative ones: leading to a degeneracy of the levels. Now, the single-particle  $f_{7/2}$  state will split up into four new states when deformation emerges:  $\Omega = \frac{1}{2}, \frac{3}{2}, \frac{5}{2}, \frac{7}{2}$  and all have negative parity. In Fig. 3.8 an illustration with the different orbits of the odd particle is given, for both the prolate deformed nuclei as well as for oblate ones. Similarly, the orbits of the same state are pictorially represented in Fig. 3.9.

From Figs. 3.8 - 3.9, it can be seen that the first orbit (denoted by orbit 1) lies closest to the core in the prolate case, while in the oblate case this is true for orbit 4. This plays the role in the interaction strength, meaning that for the prolate case, the orbit 1 will interact the strongest with the *core*, while in the oblate case, it is the orbit 4 which has the strongest interaction with the bulk core. Moreover, the strength of interaction indicates the magnitude of the energies for each projection: the stronger the interaction between the orbit and the core, the more tightly bound these states are and lie lower in energy. For prolate deformations, the orbits with smallest  $\Omega$  ‘prefer’ to lie lower in energy (interacting strongly with the core). For

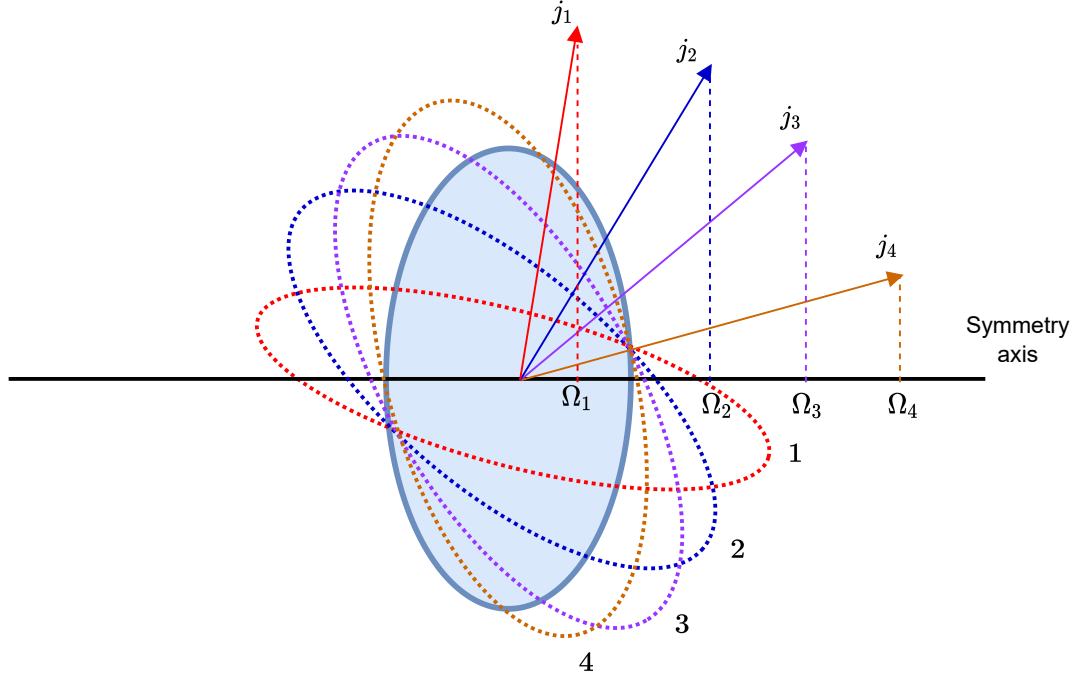


FIGURE 3.9: A simple sketch showing the single-particle orbits for the  $j = 7/2$  nucleonic state, along the symmetry axis for a *oblate* deformation. The actual projections are  $\Omega_1 = \frac{1}{2}$ ,  $\Omega_2 = \frac{3}{2}$ ,  $\Omega_3 = \frac{5}{2}$ , and  $\Omega_4 = \frac{7}{2}$ . The figure was inspired from Ref. [14].

oblate deformations, the situation is opposite: orbits with the maximal  $\Omega$  have the strongest core interactions and therefore lie lowest in energy.

Another way of looking at the coupling of the single-particle with the bulk core can be given in terms of overlaps of their corresponding wave-functions (eigenstates). Indeed, a nucleon lying in the lowest  $\Omega$  orbit will have a *maximum* wave-function overlap with a prolate core. On the other hand, nucleons lying in the highest  $\Omega$  orbits will have maximum overlap of the wave-function with an oblate core. The overlap gives the overall binding energy between the two systems (i.e., core and particle) as explained in the previous paragraph. Discussion about the wave-function overlap and the nuclear density distribution [23, 24] will be made in the following chapters.

The induced degeneracy due to deformation for a particle state  $l_j$  is shown in Fig. 3.10, for the same example of the nucleon with the orbit  $f_{7/2}$ .

Obviously, the sketch shown in Fig. 3.10 is just an instructive example, and it does not represent an accurate description of the single-particle energies for deformed nuclei. In fact, if the potential is deformed, the quantum numbers  $l$  and  $j$  are not

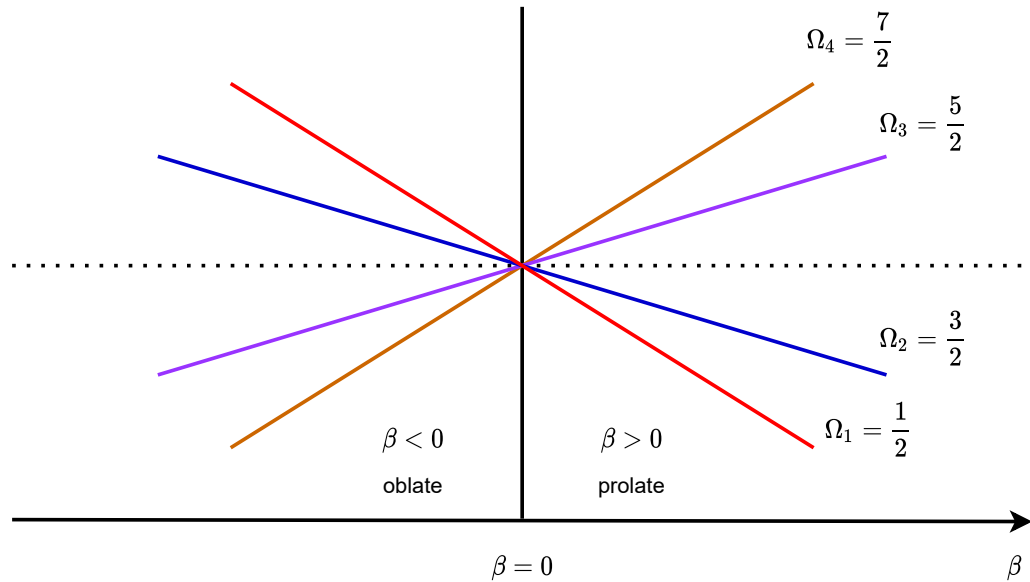


FIGURE 3.10: The effect of deformation for the particle state  $f_{7/2}$ . It can be seen that indeed, as it was mentioned within the text,  $\Omega_1$  component lies lowest in energy for the oblate deformation, and  $\Omega_4$  component lies the lowest in energy for an oblate deformation.

valid anymore (that is, the angular momentum is no longer a constant of motion for non-spherical potentials). A proper description of the single-particle orbits are represented by the so-called *Nilsson diagrams*, where the energy for each state is represented as a function of the deformation parameter. Remember that the energies are in fact the eigenvalues of the Schrödinger equation associated to the initial Nilsson deformed Hamiltonian (see Eq. 3.25).

The spectrum of one-particle orbits plays an invaluable role within the nuclear structure and the study of deformed nuclei: the picture of one-particle motion in deformed potential works for deformed nuclei much better than the case of single-particle motion in spherical potentials for spherically shaped nuclei. Multiple quantitative analyses have been performed on experimental data of well-deformed (especially odd- $A$ ) nuclei, from light ( $^{25}\text{Mg}$ ,  $^{25}\text{Al}$ ) to heavy ( $^{169}\text{Tm}$ ,  $^{175}\text{Yb}$ ,  $^{177}\text{Yb}$ ) [25]. Examples with this kind of diagrams are shown in Figs. 3.11 - 3.12.

It can be seen that each state within a Nilsson diagram is represented as a solid line or a dashed line, depending on its parity (remember that the parity quantum number is given by  $(-1)^N$  or, equivalently, by  $(-1)^l$ ). The labelling from the Figs. 3.11 - 3.12 is consistent with the one defined in the previous subsection.

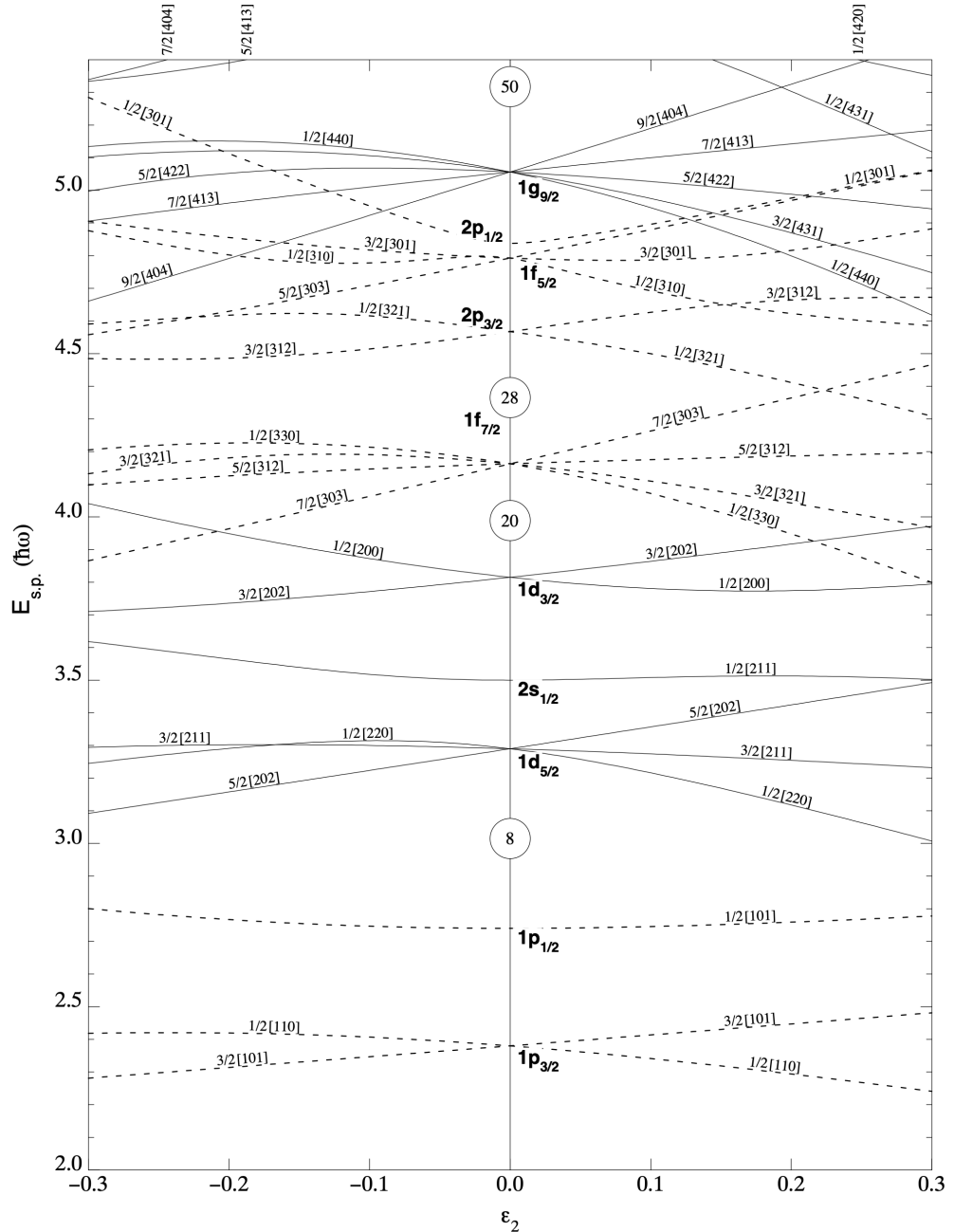


FIGURE 3.11: A Nilsson diagram for protons or neutrons, with  $Z$  or  $N \leq 50$ . Picture reproduced from Ref. [11].

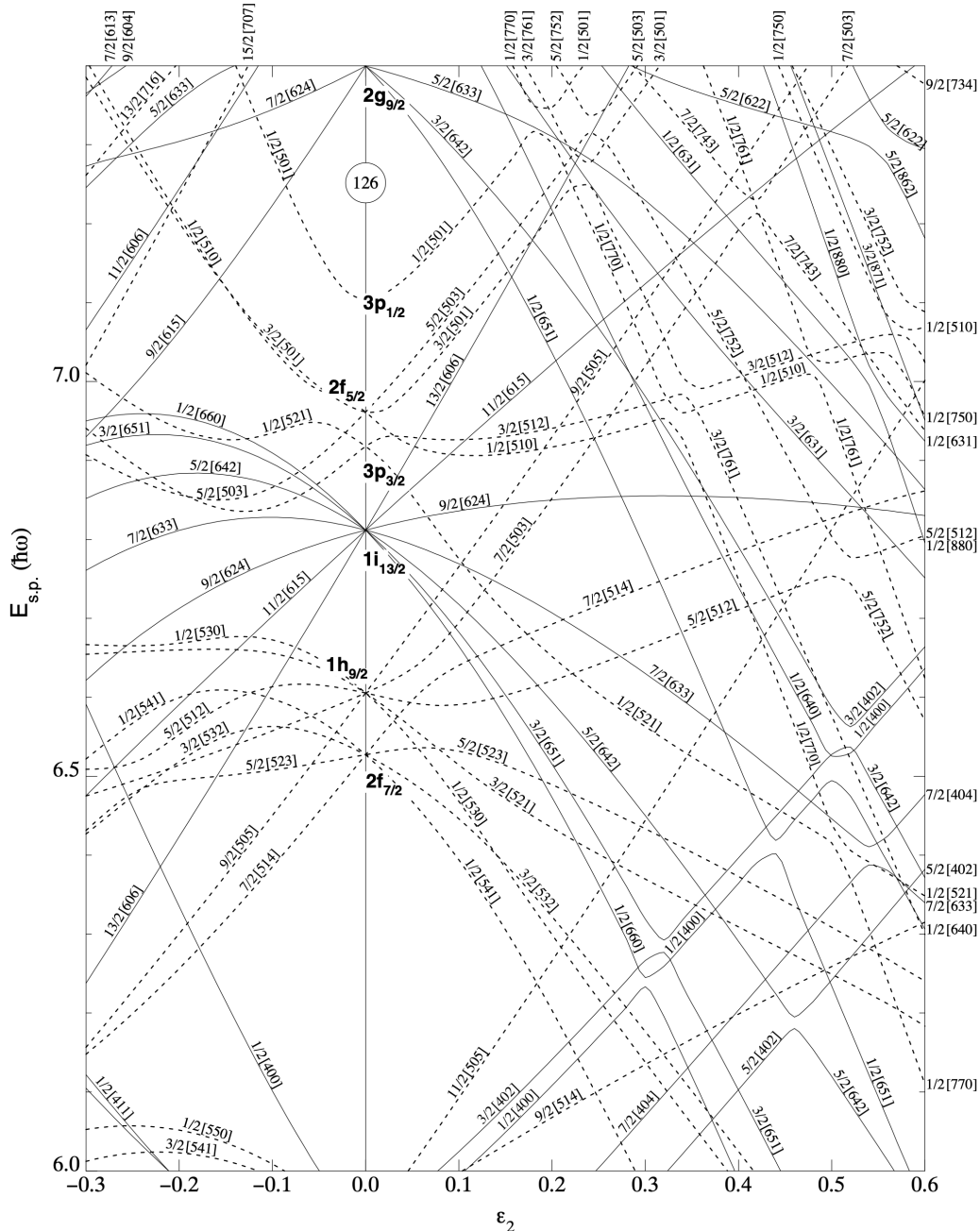


FIGURE 3.12: A Nilsson diagram for neutrons, with  $82 \leq N \leq 126$ . Picture reproduced from Ref. [11].

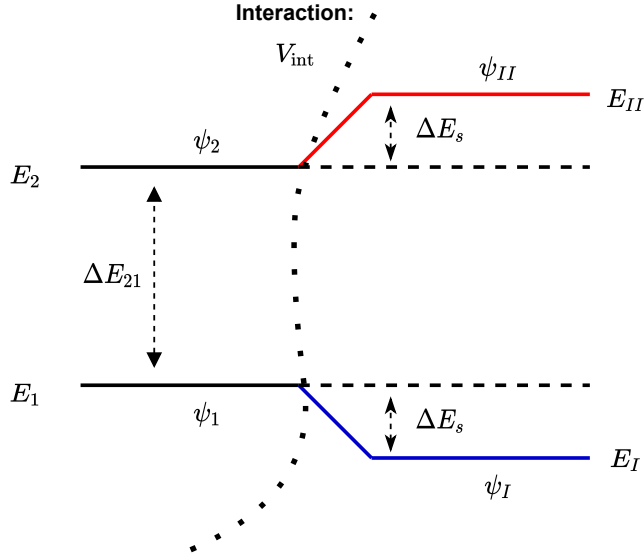


FIGURE 3.13: Defining the mixing between two different states, with two corresponding energies and wave-functions. Interaction is illustrated via the curved line and  $V_{\text{int}}$  term.

Another important aspect which can be seen in the Nilsson diagrams (for some orbits) is the ‘crossing’ between states with different quantum numbers. In order to fully understand this concept, it is instructive to go into detail about *two-state mixing*.

### Two-state mixing

In the work of Casten [9], an analytical approach is given for treating the mixing of two different states (energy levels). It starts from the basic idea of two initial levels, each with its corresponding energy  $E_1$  and  $E_2$ , and their associated wave-functions (denoted here with  $\psi_1$  and  $\psi_2$ ). Any interaction between them results in the mixing matrix element  $\langle \psi_1 | V_{\text{int}} | \psi_2 \rangle$ , where  $V_{\text{int}}$  is the arbitrary interaction between the states. This is sketched in Fig. 3.13.

This problem can be solved by finding the final energies and wave-functions, this being done via the diagonalization procedure of a  $2 \times 2$  matrix, where the main diagonal contains the two energies and off-diagonal terms represent the interaction itself. The final states will be denoted here with  $(E_I, \psi_I)$  for the energies and  $(\psi_I, \psi_{II})$  for the wave-functions. As a general rule, the mixing depends on the initial separation  $\Delta E_{21} = (E_2 - E_1)$  and the matrix element  $\langle \psi_1 | V_{\text{int}} | \psi_2 \rangle$ . Given a large spacing, the effect of a given matrix element will be quenched. Moreover, even for

a small matrix element, it can introduce a large mixing if the energy separation between the states is small (that is, the unperturbed states are lie close in energy).

A reduction from these two parameters can be performed, obtaining a single universal mixing expression that is valid for any arbitrary interaction and any initial spacing. As a first step, one should define the ratio between the spacing of the unperturbed states ( $\Delta E_{21}$ ) and the strength of the matrix element:

$$R = \frac{\Delta E_{21}}{V_{\text{int}}} . \quad (3.27)$$

With this quantity, the newly perturbed energies  $E_I$  and  $E_{II}$  are readily obtained [9]:

$$E_I = \frac{1}{2}(E_1 + E_2) + \frac{\Delta E_{21}}{2} \sqrt{1 + \frac{4V_{\text{int}}^2}{\Delta E_{21}^2}} , \quad (3.28)$$

$$E_{II} = \frac{1}{2}(E_1 + E_2) - \frac{\Delta E_{21}}{2} \sqrt{1 + \frac{4V_{\text{int}}^2}{\Delta E_{21}^2}} . \quad (3.29)$$

Even more useful would be to find the amount by which each energy is shifted after the interaction. This is denoted in Fig. 3.13 by  $\Delta E_S$  and its expression depends on  $\Delta E_{12}$  as such:

$$|\Delta E_S| = |E_{II} - E_2| = |E_I - E_1| = \frac{\Delta E_{21}}{2} \left[ \sqrt{1 + \frac{4}{R^2}} - 1 \right] . \quad (3.30)$$

The two perturbed wave functions are as follow:

$$\begin{aligned} \psi_I &= \alpha\psi_1 + \beta\psi_2 , \\ \psi_{II} &= -\beta\psi_1 + \alpha\psi_2 , \end{aligned} \quad (3.31)$$

where the two amplitudes  $\alpha$  and  $\beta$  must verify the condition  $\alpha^2 + \beta^2 = 1$  and:

$$\beta = \frac{1}{\left\{ 1 + \left[ \frac{R}{2} + \sqrt{\frac{R^2}{4} + 1} \right]^2 \right\}^{1/2}} \quad (3.32)$$

It is noteworthy to point out that the amplitude  $\beta$  is in fact a function that only depends on  $R$  (i.e., the ratio between the unperturbed energy splitting and the

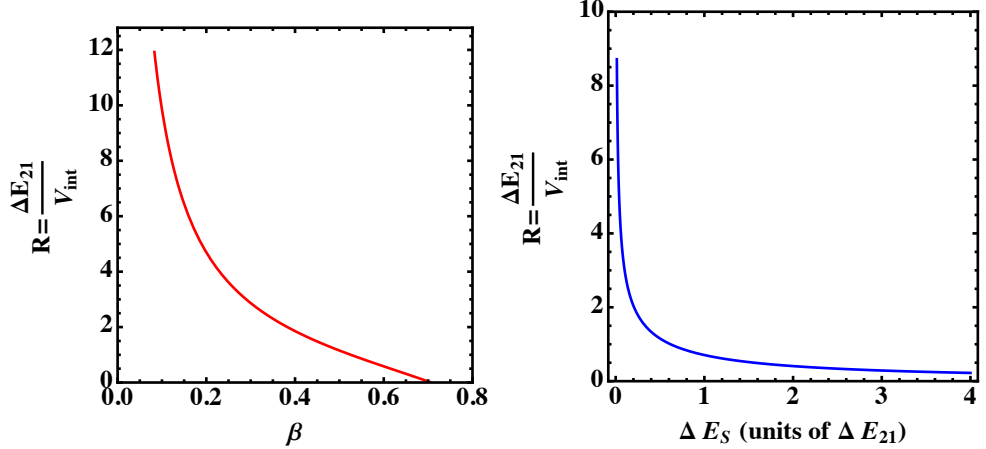


FIGURE 3.14: **Left:** The dependence of  $R$  (see text) on the mixing amplitude  $\beta$ . **Right:** The dependence of  $R$  (see text) on the energy shift of the perturbed states ( $\Delta E_S$ ).

interaction strength). Similarly, by dividing the shift in energy  $\Delta E_S$  to the initial splitting  $\Delta E_{21}$ , one will obtain an expression that is independent of the initial level spacing:

$$\frac{|\Delta E_S|}{\Delta E_{21}} = \frac{|E_{II} - E_2|}{\Delta E_{21}} = \frac{|E_I - E_1|}{\Delta E_{21}} = \frac{1}{2} \left[ \sqrt{1 + \frac{4}{R^2}} - 1 \right] \quad (3.33)$$

The importance of these formulae will be now emphasized through a numerical example. First of all, the evolution of the ratio of the unperturbed shift and the interaction can be graphically represented as a function of the small mixing amplitude  $\beta$  by the use of Eq. 3.32. The graphical representation is shown in Fig. 3.14. Following this analysis, also in Fig. 3.14 the shape of  $R$  as a function of the energy shift of the perturbed states can be visualized.

For an arbitrary case where two initial states are separated by, say  $\Delta_{21} = 0.07$  MeV, and they become *perturbed* via the interaction with a strength  $V_{\text{int}} = 0.03$  MeV, this gives a value of  $R = 3.5$  and, moreover, the mixing amplitude is  $\beta = 0.256$ . The two states will both be shifted by only  $\Delta E_S = 5.31$  keV (accounting for about 7.6% of the initial separation). Indeed, for this particular example, the perturbation results in an energy shift that is rather small compared to the initial state spacing.

Besides the numerical example discussed above, there are also two extremely important limiting situations when two states interact via a perturbation. The first one is the so-called *strong mixing limit*, when the two initial states are degenerate

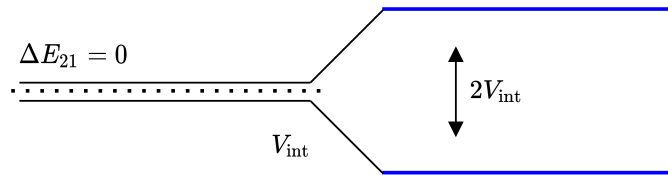


FIGURE 3.15: The *strong mixing* limit for two energy levels that are interacting via a perturbation. The initial two levels are degenerate, such that their splitting is null.

(i.e., there is practically no spacing between them and  $\Delta_{21} = 0$ ). In this situation, the analytical expressions from Eq. 3.30 fail to provide a quantitative analysis, but from Eq. 3.29 a small adjustment of the expression will give rise to the following:

$$E_{I,II} = \frac{1}{2} [(E_1 + E_2) \pm 2V_{\text{int}}] = E_0 \pm V_{\text{int}}, \quad (3.34)$$

where the initial (common) energy of the two degenerate states is denoted by  $E_0$ . The above equation indicates the important fact that the energy shift which the two states suffer via the perturbation is only given by the *mixing matrix element*. This means that the final separation energy for a two-state isolated system can never be closer than twice the interaction strength ( $2V$ ). In the degeneracy case, the values for  $\beta$  and  $\alpha$  are readily obtained: ( $\beta = \alpha = \frac{1}{\sqrt{2}} = 0.707$ ), such that the states are completely mixed. Consequently, the mixed wave-functions of two (initially) degenerate states do not depend on the strength  $V_{\text{int}}$  between them. The limiting case of *strong mixing* of two degenerate levels is sketched in Fig. 3.15.

The second limiting case is called *weak mixing limit*, corresponding to a very large value of  $R$  (meaning that the initial separation of the states is very large compared to the magnitude of the interaction itself). The shift in energy of the perturbed states in this case is given by:

$$\frac{|\Delta E_S|}{\Delta E_{21}} = \frac{1}{R^2}. \quad (3.35)$$

A graphical representation for the weak mixing is shown in Fig. 3.16.

As a final step in the analysis of the two-state mixing, it is worth mentioning a corner-case which will help to get a better grasp of the Nilsson orbitals. Consider two states (say  $\psi_1$  and  $\psi_2$ ) whose energies are parametrized in terms of some argument  $c_{\text{nuc}}$  which is relevant for the nuclear structure of that system (e.g.,  $c_{\text{nuc}}$  could be a quadrupole deformation and the two initial states are in fact Nilsson

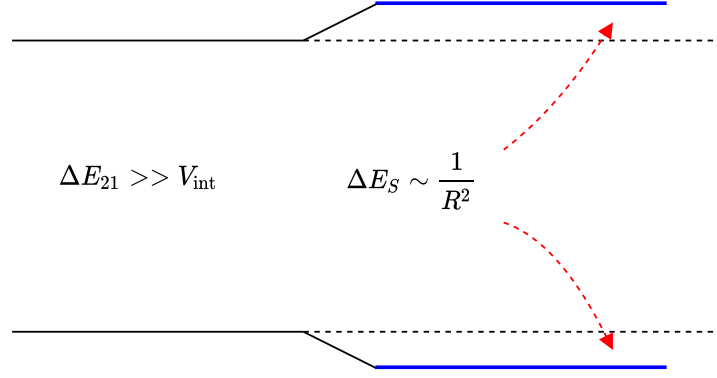


FIGURE 3.16: The *weak mixing* limit for two energy levels that are interacting via a perturbation. The interaction strength is much smaller than the initial spacing between states, resulting in a very small energy splitting  $\Delta E_S$ .

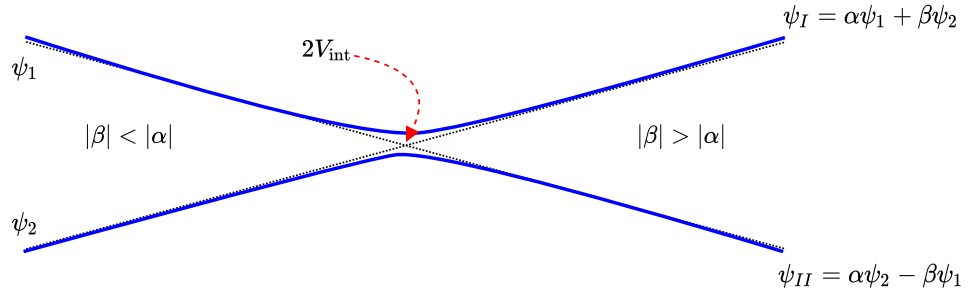


FIGURE 3.17: A sketch showing the concept of *non-crossing* between two states. Arrow represents the closest point at which the two states can interact with each other (i.e., the inflection point).

orbits). The remarkable ‘feature’ of this hypothesis is that if there indeed exists mixing between the two states, they can never cross each other. The two mixed states will always repel and they can never be closer than twice the mixing matrix element  $V_{\text{int}}$  after mixing occurs. In Fig. the behavior of non-crossing for the mixed states is sketched. The point at which the two states are the closest to each other represents the case when the wave-functions contain similar admixtures of each of the initial states (unperturbed). The *inflection point* can be seen in Fig. 3.17, where the behavior of the final states  $\psi_I$  and  $\psi_{II}$  can be seen.

## Nilsson orbitals

With the concept of two-state mixing clearly depicted, it is instructive to go further into the Nilsson orbitals and their significance. Recalling Fig. 3.10, the splitting of a  $j$  orbital into  $j + 1/2$  magnetic sub-states can be viewed as a set of orbitals (energies) where the nucleon orbits around the bulk nucleus with an orbit that

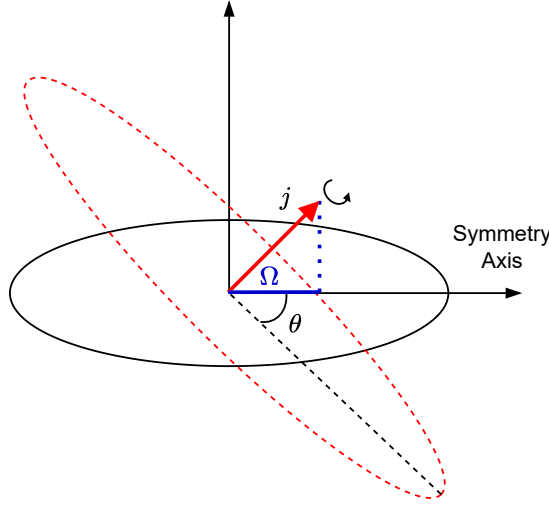


FIGURE 3.18: The orbit of a single particle orbiting the deformed nucleus, defined by the projection of the particle's a.m.  $\Omega$  (on the symmetry axis) and the tilting angle  $\theta$ . Figure inspired from Ref. [9]

has a certain *tilt* angle  $\theta$  (see the orbits depicted in Figs. 3.8 and 3.8). The tilting angle is conceptually showed in Fig. 3.18, where a magnetic sub-state with given  $\Omega$  is shown. For that particular orbit, the angle is given by the expression [9, 14]:

$$\begin{aligned} \sin \theta &= \frac{\Omega}{j}, \\ \theta &= \arcsin\left(\frac{\Omega}{j}\right). \end{aligned} \quad (3.36)$$

The change of  $\theta$  is rather slow for low  $\Omega$  projections, while rapid changes take place at high  $\Omega$  values. As a numerical example, the change in  $\theta$  is studied for the orbits  $j = \{9/2, 11/2, 13/2\}$ , with their corresponding projections. The evolution with  $\Omega$  for different orbits can be seen in Fig. 3.19.

The simplistic shapes within the splitting of an orbital  $j$  into multiple sub-states (see Fig. 3.10) emerge from the considerations regarding the change in tilting angle  $\theta$  and the observation that the difference in energy is rather slight (high) depending on low (high)  $\Omega$  values.

Based on this discussion, it is clear that a full Nilsson diagrams is constructed with the configuration mixing of different  $j$  values, configuration which is superimposed on state-splitting via the  $\Omega$  projections. With this idea, one can state that *no two*

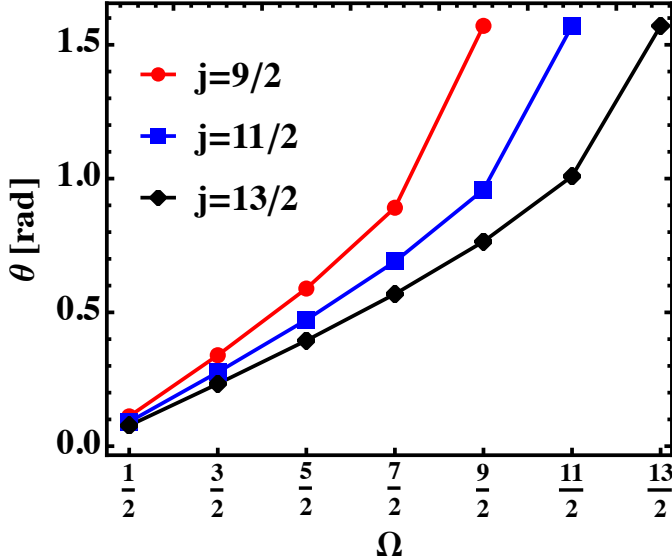


FIGURE 3.19: The change in  $\theta$  with increasing values of  $\Omega$ , for given orbitals  $j$ .

lines in the Nilsson diagram with similar  $\Omega$  values can cross each other. As two such orbits come close to each other, they must repel as shown in Fig. 3.17. Explaining the behavior of the lines that appear in the Nilsson diagrams 3.11 - 3.12 is straightforward: each line represents a Nilsson state, starting out in a straight line and then sloping downward or upward, depending on the angle of the orbit relative to the bulk nucleus. The *curving* of an orbit starts when it approaches another level with the same quantum number  $\Omega$  and parity  $\pi$ . Thus, the structure of any Nilsson diagram relies on three main features [9]:

- the  $\Omega$  splitting
- repulsion between two levels
- single-particle shell model energies

Taking a closer look at the second Nilsson diagram previously shown (see Fig. 3.12), there are two orbits within the 82-126 neutron shell that can be analyzed in terms of *mixing*:  $f_{7/2}$  and  $h_{9/2}$ . Obviously, the lack of deformation implies a degeneracy of these orbits, but when deformation occurs, splitting kicks in. The angle of the orbital orientation  $\theta$  depends on the ratio  $\frac{\Omega}{j}$  (recall formula  $\theta = \arcsin \frac{\Omega}{j} \approx \frac{\Omega}{j}$  for low  $\Omega$ ). Small tilting angles will occur due to i) small values of  $\Omega$  or ii) high  $j$ . As a result, the energies for the orbits  $\Omega = 1/2, 3/2, 5/2$  belonging to the  $h_{9/2}$  shell are decreasing in energy faster with deformation than those from  $f_{7/2}$  orbit. Consequently, the different rates of decrease of the Nilsson

energies will overcome any small spherical energy separation  $f_{7/2} - h_{9/2}$ , making the orbits with low  $\Omega$  to approach each other: mixing becoming more pronounced. But as discussed in the section devoted to *two-state mixing*, two orbits defined by the same quantum numbers cannot cross each other, so they will repel, leading to the *inflection point*. The points can be seen, for example, when looking at the  $\Omega = 5/2$  and  $\Omega = 7/2$  orbits, corresponding to  $f_{7/2}$  and  $h_{9/2}$ , respectively.

Lastly, an alternative form of the Nilsson Hamiltonian should be expressed, taking into consideration the already studied nuclear radius (see Eq. 2.1 which describes the shape of the nuclear surface) and the fact that until now, only the *quadrupole* effects have been relevant to the discussion about deformed potentials in nuclei. Indeed, for quadrupole deformations, the nuclear radius can be simplified to:

$$R(\theta, \varphi) = R_0 (1 + \beta Y_2^0(\theta, \varphi)) . \quad (3.37)$$

The single-particle Hamiltonian can be written in the general form, starting from the expression Eq. 3.20:

$$\begin{aligned} H_{\text{Nil}} = & -\frac{\hbar^2}{2m} + \frac{1}{2}m(\omega_0 r)^2 - \frac{4}{3}\sqrt{\frac{\pi}{5}}m(\omega_0 r)^2\epsilon Y_2^0(\theta, \varphi) - 2\kappa\hbar\omega_0(\vec{l} \cdot \vec{s}) \\ & - 2\kappa\hbar\omega_0\mu(l^2 - \langle l^2 \rangle_N) . \end{aligned} \quad (3.38)$$

The expression for the oscillator frequencies were already given (defined as functions of the deformation parameter  $\epsilon$ ), and they keep the same form (see Eqs. 3.23 - 3.24). It is worth mentioning that both forms of  $H_{\text{Nil}}$  are equivalent, and allow to describe the structure of the deformed nuclei in the limits of large deformations (via Eq. 3.20) and small deformations (via Eq. 3.38). Within literature, the two parameters  $\kappa$  and  $\mu$  have usually values around 0.06 for the former and (0  $\sim$  0.7) for the latter. As previously shown, the relationship between the  $\epsilon$  and  $\beta$  deformation parameters is given by  $\epsilon = 3/4\sqrt{5/\pi}\beta$ .

When the deformations are small,  $j$  is a good quantum number, and the Eq. 3.38 represents a Hamiltonian for the AHO (which it was discussed) plus a *perturbation* that is proportional to  $\epsilon r^2 Y_2^0$ . One can consider the eigenstates of the Hamiltonian as some states labelled by the quantum numbers  $Nlj$  and  $m$  typical to the spherical case. Casten shows that if the angular part  $Y_2^0$  is treated as a perturbation, it is

possible to obtain a shift in energies relative to  $\epsilon = 0$  [9]:

$$\Delta E_{Nljm} = -\frac{4}{3}\sqrt{\frac{\pi}{5}}m\omega_0^0\epsilon \langle Nljm| r^2 Y_2^0 | Nljm \rangle . \quad (3.39)$$

Furthermore, one can perform a separation of the radial and the angular parts while using the known relation for a harmonic oscillator potential:

$$\frac{1}{2}m\omega_0^2 \langle Nljm| r^2 | Nljm \rangle = \frac{1}{2}\hbar\omega_0 \left( N + \frac{3}{2} \right) , \quad (3.40)$$

and, together with the evaluation of the matrix elements for spherical harmonics, the final expression for the energy shift at small deformations is:

$$\Delta E_{Nljm} = -\frac{2}{3}\hbar\omega_0 \left( N + \frac{2}{3} \right) \epsilon \frac{[3K^2 - j(j+1)] [ \frac{3}{4} - j(j+1) ]}{(2j-1)j(j+1)(2j+1)} , \quad (3.41)$$

with the projection of the total a.m. on the  $z$  axis replacing the projection  $m$ . Based on Eq. 3.41, the following properties for a Nilsson diagram (within the small deformation regime) emerge:

- There is a  $K^2$  dependence for the energy shifts
- The quadrupole deformation parameter (albeit  $\epsilon$  or  $\beta$ ) shows a clear linear dependence for  $\Delta E_{Nljm}$
- Another linear dependence for the shifts is induced by the principal (oscillator) quantum number  $N$ .
- When the deformation parameter is positive, there are more downward sloping orbits than upward ones. (Example discussed below)

For a value of  $j$  greater than  $1/2$ , the terms  $[3K^2 - j(j+1)]$  and  $3/4 - j(j+1)$  are negative, resulting in the following types of orbits: [14]:

$$\text{downward sloping: } K < \sqrt{\frac{j(j+1)}{3}} = \frac{j}{1.8} \approx 0.65j , \quad (3.42)$$

$$\text{upward sloping: } K > 0.65j . \quad (3.43)$$

It was already shown that the angular orientation (i.e., the tilting angle  $\theta$ ) of an orbit is given by  $\theta = \arcsin(K/j)$ . Checking to see for what value of  $\theta$  the

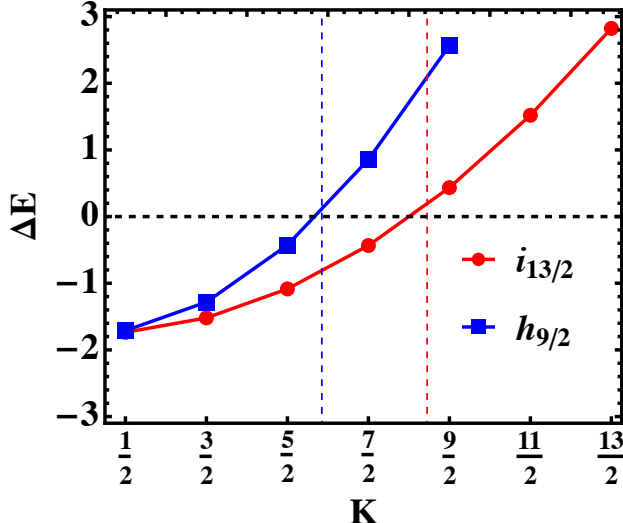


FIGURE 3.20: The energy shift  $\Delta E$  for two orbits:  $h_{9/2}$  and  $i_{13/2}$  for a given deformation  $\epsilon = 0.22$ . The dashed vertical lines (colored) represent the value for  $K$  where the ‘change’ from downward sloping curves to upward sloping curves takes place (that is  $K \approx 0.65j$ ). This is just an illustrative example inspired from the discussion regarding single-particle orbits in Ref. [9]

ratio  $K/j = 0.65$  corresponds to, this will lead to  $\theta = 40^\circ$ . Consequently, the physical implication is that any larger *tilt* of an orbit within a prolate quadrupole deformation is energetically unfavorable. In Fig. 3.20 two different  $j$  orbits, namely  $h_{9/2}$  and  $i_{13/2}$  are studied in terms of their energy shifts according to Eq. 3.41. It can be seen that indeed, there are more downward sloping orbitals, since the quadrupole deformation parameter has been set to a positive value  $\epsilon = 0.22$ .

There is another important physical consequence emerging from the four main characteristics mentioned above, based on the principal quantum number  $N$ . The dependence on  $N$  will imply that the slopes of any Nilsson energy level will be *steeper* as  $N$  has large values. As such, heavier nuclei will tend to deform much easier than lighter ones. The explanation for the influence of large  $N$  on the steepness was done in Refs. [1, 9, 14]. Shortly, a nucleon belonging to a high oscillator shell will have a large average radius (the expectation value of  $r^2$  was done in Eq. 3.41 via the expression  $\langle r^2 \rangle = (N+3/2)$  [18]). As the nucleus deforms, the density distribution of the nuclear matter will approach that orbit. The effect on the orbiting nucleon to decrease its energy rapidly as the nuclear matter comes closer to the orbit is due to the *attractive* nature of the nuclear force itself. Clearly, this effect is less obvious for a particle in a lower oscillator shell that is already very close to the rest of the nuclear matter.

The centrifugal  $\vec{l}^2$  and spin-orbit  $\vec{l} \cdot \vec{s}$  terms from Eq. 3.38 will become negligible in the limit of *large deformation*, such that the Nilsson Hamiltonian will reduce to the known AHO-like form. In this special case, the motion will separate into *independent* oscillations in the direction of the symmetry axis and the perpendicular plane (i.e., in the direction of  $z$ -axis and  $xy$  plane). Consequently, the good quantum numbers for this kind of situation are the  $n_z$  and  $(n_x + n_y)$  oscillator quantum numbers. Since the eigenvalues for a one-dimensional (and, implicitly for the three-dimensional) harmonic oscillator are established, the energy spectrum for single-particle orbits in the regime of large  $\epsilon$  (or, equivalently  $\beta$ ) will be given by:

$$E_{n_x, n_y, n_z} = \hbar\omega_x(N - n_z + 1) + \hbar\omega_z\left(n_z + \frac{1}{2}\right). \quad (3.44)$$

The remarkable feature of the Hamiltonian which corresponds to this set of eigenvalues is its invariance to rotations about the  $z$  axis. The projections for the particle's orbital and spin a.m. are constants of motion. As it was previously discussed, the sum of the two projections  $\Lambda$  and  $\Sigma$  is indeed  $\Omega$  or equivalently  $K$  in the case of  $\vec{R}$  being perpendicular to the  $z$ -axis.

With this, the description of the Nilsson Deformed Model is clear enough for understanding it and also be able to justify its importance within the rest of the present work. It will be shown that based on the so-called Particle-Rotor-Model [1, 26], it plays a crucial role in determining the Hamiltonians that are specific to the phenomena (and implicitly the nuclei) of interest.

### 3.4 Collective Model

Although the previous single-particle model is able to successfully treat many nuclei (e.g., those which are lie near closed shells), the single-nucleon motion within a (deformed) potential is not enough to describe for example: nuclear fission, values for quadrupole moments of multiple deformed nuclei [27] or lifetime measurements that through single-particle calculations fail to reproduce experimental data on some gamma-ray transitions (of electric quadrupole type) [28].

The collective model is one of the most ‘complete’ tools in describing the nuclear phenomena across the chart of nuclides. It brought tremendous progress within

nuclear community in order to validate but also predict nuclear behavior in the high-spin limit for example. A major feature of this model is the introduction of the so-called *rotational bands*, characteristic of deformed nuclei which will be discussed in detail later on, since it is of crucial interest to this work.

Developed by Bohr and Mottelson [1, 29] more than 50 years ago the Nuclear Collective Model, it is based on the Liquid-Drop-Model (which formulated by Niels Bohr [30]). Moreover, the predictions for nuclear deformation made by Rainwater [31] played another fundamental role in the model's development. The basic assumption within this model is that the nuclear density distribution can be approximated as a droplet of nuclear matter which has shape-specific degrees of freedom. This nuclear droplet is also capable of vibrating and rotating (remember the discussion from Chapter 2, where the nuclear radius was described in terms of some *collective coordinates*: the coordinates dictate the shape evolution with time, letting the entire shape to vibrate and rotate.)

### 3.4.1 Bohr Hamiltonian

As a first step, the concept of a nuclear liquid drop is used to construct the Hamiltonian of the problem. The droplet is said to exhibit excitations shape (or surface) oscillations which have a dynamical character. These shape oscillations are illustrated in Fig. 3.21, where one can interpret that as a vibrating nucleus with a spherical equilibrium shape. Since the collective coordinates are time-dependent, at each moment in time, the nuclear radius  $R$  at moment  $t$  will locate a point on the surface in the direction given by the radial coordinates  $\theta, \varphi$ .

By using Eq. 2.1 which characterizes the *vibrations* of a nuclear surface (via the collective coordinates  $\alpha_{\lambda\mu}$ ), one can give the expression of an initial Hamiltonian of *collective* nature as:

$$H_{\text{coll}} \equiv T + V = \frac{1}{2} \sum_{\lambda\mu} \left[ B_\lambda \left| \frac{d\alpha_{\lambda\mu}}{dt} \right|^2 + C_\lambda |\alpha_{\lambda\mu}|^2 \right], \quad (3.45)$$

Hamiltonian which is in fact both invariant under rotation and time reversal [32]. The real numbers  $B_\lambda$  and  $C_\lambda$  represent *inertial* and *stiffness* parameters for the nuclear matter. The spectrum of such a Hamiltonian after a canonical quantization (see calculations in Ref. [4] or [18]) will have a harmonic-like structure, depending

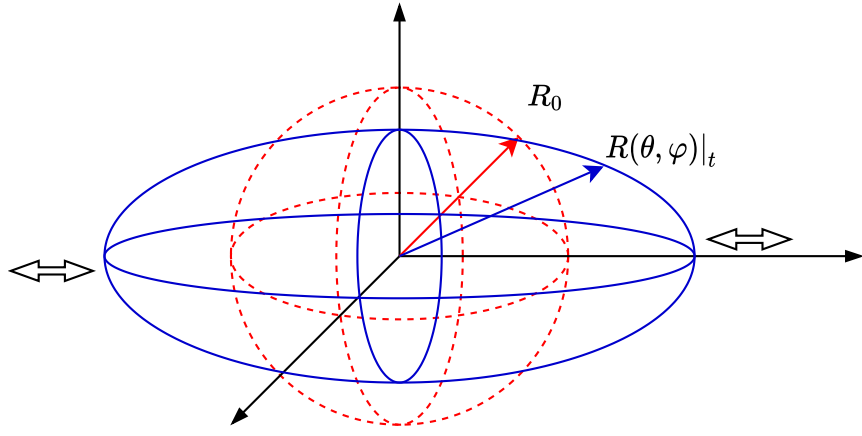


FIGURE 3.21: The vibration of a nucleus whose equilibrium shape is a spheroid, with nuclear radius  $R_0$  (*average nuclear radius*) and the nuclear radius at a different moment in time.

on the value of  $\lambda$ . Indeed, by looking at the expression from Eq. 3.45 one can see that it can be brought to a form:

$$H_{\text{coll}}^{\text{osc}} = \frac{p^2}{2m} + \frac{1}{2}kr^2 , \quad (3.46)$$

which is typical to a harmonic oscillator Hamiltonian. The frequency of oscillation of such a Hamiltonian is given by the relation  $\omega = \sqrt{k/m}$ . The vibrations can now be understood in terms of a sum of harmonic oscillator frequencies, where each frequency is given by  $\lambda$ :

$$\omega_\lambda = \sqrt{\frac{C_\lambda}{B_\lambda}} . \quad (3.47)$$

The inertia term  $B_\lambda$  (also called the *mass parameter*) has the following expression [4]:

$$B_\lambda = \frac{\rho m R_0^5}{\lambda} = \frac{3}{4\pi\lambda} Am R_0^2 , \quad (3.48)$$

showing a quadratic dependence with the average nuclear radius. With these ingredients, one can sketch a form of  $H_{\text{coll}}$  similar to Eq. 3.46 in the following manner:

$$H_{\text{coll}} = \sum_{\lambda\mu} \hbar\omega_\lambda \left( N_{\lambda\mu} + \frac{1}{2} \right) , \quad (3.49)$$

where indeed, the typical harmonic oscillator spectrum should be expected for the final collective spectra of nuclei.

The recipe for further manipulation of the Bohr's collective Hamiltonian from Eq. 3.45 is quite a lengthy process [1, 4], with several considerations that are beyond the scope of the current work. Shortly, for the quadrupole deformed nuclei, the expression of the potential term  $V$  will be a function that depends on the parameters  $(\beta, \gamma)$ , potential that is defined as a quadratic approximation in the vicinity of a deformed minimum point  $p_0|_{\min} = (\beta, \gamma_0)$ . This starts from the general assumption that the nucleus has the deformation  $p_0$  in the ground state, and the excitations are rotations and small oscillations around this *equilibrium* deformation point. Thus  $V(\beta, \gamma)$  can be written as:

$$V(\beta, \gamma) = \frac{1}{2}C_{20}(\alpha_{20}(\beta, \gamma) - \alpha_{20}^2)^2 + \frac{1}{2}C_{22}(\alpha_{22}(\beta, \gamma) - \alpha_{22}^0) . \quad (3.50)$$

Choosing the body-fixed axis as a reference system makes the calculations much easier, since the system's axes coincide with the principal axes of the ellipsoid itself. Assuming such a coordinate system and an ellipsoid which possesses axial symmetry, one can write the kinetic term  $T$  of the Hamiltonian as a sum of a *rotational* and a *vibrational* part.

$$T = T_{\text{vib}} + T_{\text{rot}} . \quad (3.51)$$

The equations for the two sub-terms are thoroughly demonstrated in Ref. [33]. Their expressions are given in terms of the deformation parameters  $(\beta, \gamma)$ , the mass parameters  $B_2$  (for the quadrupole deformations) and the stiffness parameters  $C_2$ . Thus, the vibrational term is:

$$T_{\text{vib}} = \frac{1}{2}B_2(\dot{\beta}^2 + \beta^2\dot{\gamma}^2) , \quad (3.52)$$

and the rotational term is:

$$T_{\text{rot}} = \frac{1}{2}\sum_i \mathcal{I}_i \omega_i^2 , \quad (3.53)$$

where the index  $i = 1, 2, 3$  suggests each of the three principal axes of the ellipsoid (this notation is different from the previous notations  $x, y, z$  and it will always suggest the body-fixed system). In the expression of  $T_{\text{rot}}$ , two crucial physical

quantities arise, namely the angular velocities around each body-fixed axis and the functions  $\mathcal{I}_k$  that will eventually play the role of *moments of inertia*. However, it is important to analyze the functions  $\mathcal{I}_k(\beta, \gamma)$  in order to better understand what kind of nature the nucleus exhibit in its rotational and vibrational motion. Ref. [4] shows that:

$$\mathcal{I}_k = 4B_2\beta^2 \sin^2 \left( \gamma - \frac{2\pi}{3}k \right) . \quad (3.54)$$

In the case of fixed deformation (that is  $\beta$  and  $\gamma$  do not change), then the rotational kinetic term represents the energy of a rotor with the moments of inertia  $\mathcal{I}_{1,2,3}$ , i.e., a *pure rotor*. When the deformation parameters are changing, the rotational and vibrational degrees of freedom will become coupled by the deformation dependence of  $\mathcal{I}_k$ , leading to a situation that is not specific to a pure rotor. In fact, the functions  $\mathcal{I}_k$  will not represent the moments of inertia (MOI) for a rigid rotor anymore. However, a comparison between  $\mathcal{I}$ , the rigid-like  $\mathcal{I}_k^{\text{rig}}$  MOI, and irrotational-like MOI  $\mathcal{I}_k^{\text{irr}}$  is done experimentally, from determinations of the energy spacing between the first excited states. The last two quantities have the following expressions [4, 5]:

$$\mathcal{I}_k^{\text{rig}} = \frac{2}{5}mAR_0^2 \left( 1 - \sqrt{\frac{5}{4\pi}\beta \cos \left( \gamma - \frac{2\pi}{3}k \right)} \right) , \quad (3.55)$$

$$\mathcal{I}_k^{\text{irr}} = \frac{3}{2\pi}mAR_0^2\beta^2 \sin^2 \left( \gamma - \frac{2\pi}{3}k \right) . \quad (3.56)$$

The dependence of the two types of MOI on the triaxiality parameter  $\gamma$  (and fixed  $\beta$ ) can be seen in Fig. 3.22. The differences between the irrotational-like and rigid MOI are as follow:

- The irrotational MOI vanish when the ellipsoid has axial symmetry
- $\mathcal{I}^{\text{irr}}$  is much more sensitive to the deformation  $\beta$ , while the rigid MOI have most of the contribution coming from a typical rigid sphere-like MOI
- Determinations of the *experimental* MOI for well-deformed nuclei show that the irrotational MOI is smaller by a factor of almost 3 than the experimental values. Moreover, the rigid MOI show a factor of 2 larger than the

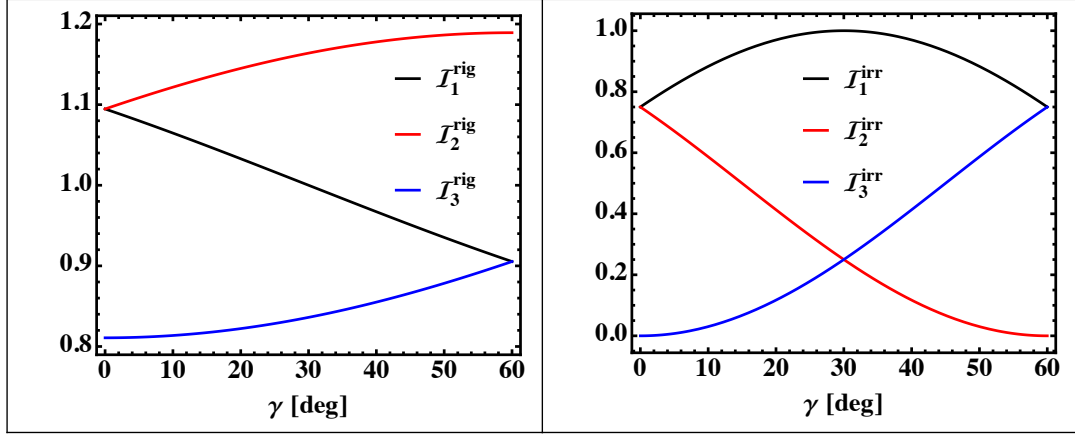


FIGURE 3.22: Comparison between the irrotational-like and the rigid-like MOI defined in Eq. 3.56 that are typical for a rigid rotator or the irrotational motion of a fluid. The deformation parameter  $\beta$  is 0.3. Note the vanishing of the irrotational MOI when axial symmetry is present.

experimental values:

$$\mathcal{I}^{\text{irr}} < \mathcal{I}^{\text{exp}} < \mathcal{I}^{\text{rig}}, \quad (3.57)$$

suggesting that the *real* flow structure within a nucleus is neither irrotational, nor like a rigid rotator.

### 3.4.2 Nuclear Vibration

The energy scheme is composed of levels that are built from these oscillator frequencies. The absorption or emission of vibration-like energy quanta (i.e., phonons) that a nucleus can do (passing to a higher or a lower level) will be in terms of dipole, quadrupole, octupole, etc. vibrating phonons. These excitations will contribute to building the entire spectrum of the nuclei, starting with the ground state: resulting in the so-called *vibrational bands*. Since the the quadrupole effects are of interest within the current work, the vibrational spectrum specific to quadrupole  $\lambda = 2$  phonons can be seen in Fig. 3.23.

A general rule that is used to construct such vibrational bands is related to the concept of *symmetrized states*. Since the excited quanta are represented by phonons (identical bosons) which have integer angular momentum (e.g.,  $\lambda = 2$  for the quadrupole vibrations) the only spin states than can be observed in such spectra

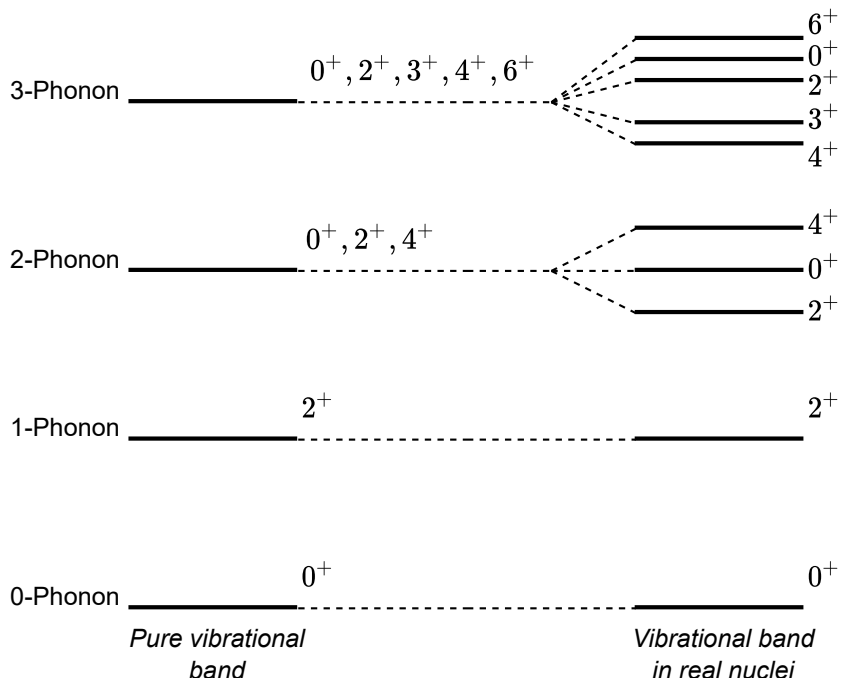


FIGURE 3.23: An illustrative example with vibrational bands that are built as excitations of multiple phonons on a ground state. The left side contains an ideal harmonic vibrator, with the degenerate spin states indicated for each level. Right side contains the non-degenerate vibrational levels that exist in nuclei. Keep in mind that the each phonon level is built as multiple excitations of a *quadrupole phonon*.

are the ones for which the final angular momenta couple to give symmetric combinations. This is the reason why in the energy state created by exciting the ground state  $0^+$  with two phonons, only the states  $0^+, 2^+, 4^+$  appear; the spin states  $1^+$  and  $3^+$  do not give symmetric combinations. A more generic method for determining which sequence of spins can be obtained by coupling angular momenta of vibrational phonons can be seen in Ref. [4].

A quantity which is often used within the measurements of nuclear properties is the ratio between the second and the first excited states within a band. These ratios are usually denoted by  $E(4^+)/E(2^+)$  (the state  $4^+$  belongs to the triplet phonon state depicted in Fig. 3.23), and the theoretical value for the vibrational model gives a value of 2. However, some experimental results point out to a value close to 2.2 for nuclei below  $A = 150$ , and a constant value of 3.3 for  $150 < A < 190$  (refer to Fig. 3.33). It should be noted that for the latter case, the value of the ratio is specific to another kind of nucleonic motion: *rotation*, which will be discussed in the following section. Example of experimental *vibrational bands* for several even- $A$  nuclei are shown in Fig. 3.24.

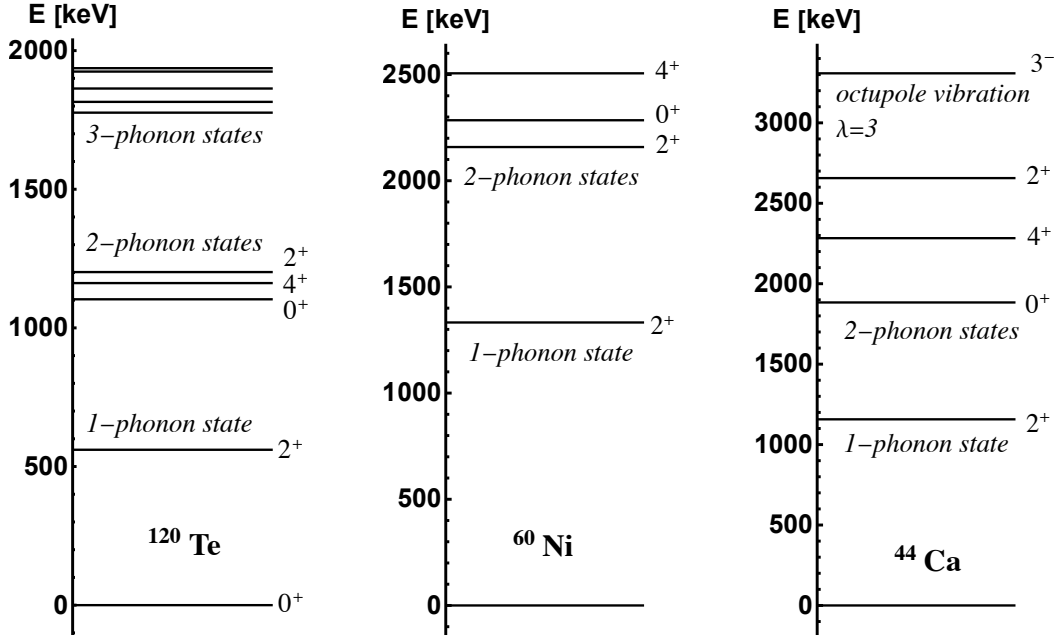


FIGURE 3.24: Vibrational bands in even- $A$  nuclei. **Left:** The experimental energy levels for  $^{120}\text{Te}$ , showing a vibrational structure for this nucleus. The triplet states that correspond to two excited quadrupole phonons can be seen, together with the quintuplet formed by adding three phonons to the  $0^+$  ground state. Experimental data is taken from [34]. **Middle:** The experimental data for  $^{60}\text{Ni}$ . For simplicity, only the first two phonon states are represented. Experimental data for this nucleus was taken from Ref. [35]. **Right:** The experimental data for a vibrational-like structure in  $^{44}\text{Ca}$ . Data is taken from Ref [36]. For the last spectrum, one can observe an energy level coming from the vibrational motion corresponding to an *octupole* mode ( $\lambda = 3$ ).

There can also be vibrational bands in odd- $A$  nuclei. Indeed, if one considers the nucleus as a spherical even-even core plus an extra nucleon, the *final* nuclear states are formed by coupling an individual  $j$  orbit with the vibrational states of the core. In the case of odd- $A$  nuclei, one can take the case of  $^{63}\text{Cu}$ , which has the ground state  $3/2^-$ . The g.s. for this nucleus is given by the last *uncoupled* nucleon that occupies a shell. In fact, for this particular nucleus, it is the  $2p_{3/2}$  proton that will give the final spin and parity of the nucleus. The vibrational spectrum which arises here can be explained by coupling the aforementioned proton with the even- $A$  core of  $^{62}\text{Ni}$ . Indeed, by taking a  $2^+$  vibrational phonon from the even nucleus, then the (odd-proton)+(phonon) system can generate a sequence of energy states that are given by the angular momenta coupling rules (i.e., negative parity states with  $I = 1/2, 3/2, 5/2, 7/2$  will be formed). This kind of particle-core coupling that generates sequences of bands will be relevant later on, when discussing the formalism of this work. The energy levels depicted in Fig. 3.25

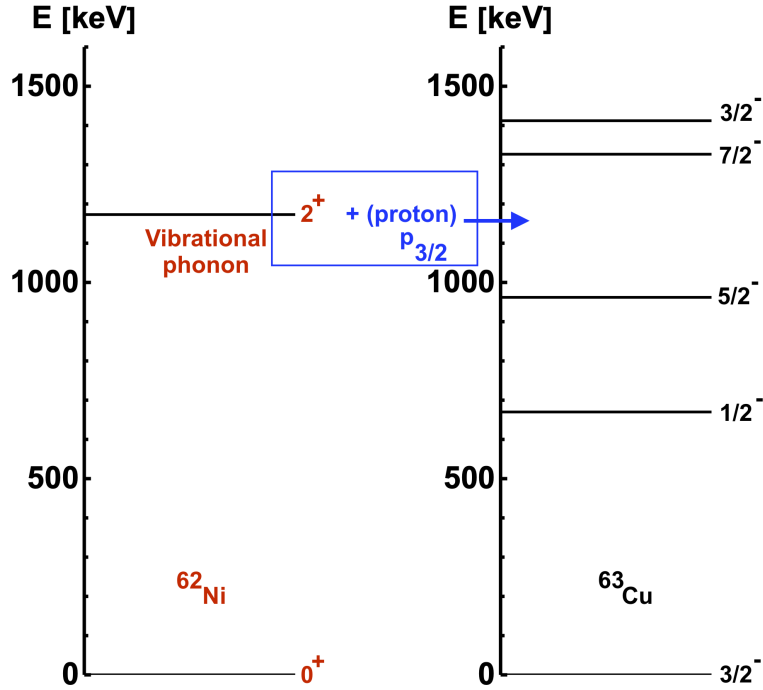


FIGURE 3.25: The experimental data of the vibrational states in  $^{63}\text{Cu}$ . The  $2^+$  phonon state in  $^{62}\text{Ni}$  is also shown for a clearer picture. The experimental data for  $^{62}\text{Ni}$  was taken from Ref. [37] and for  $^{63}\text{Cu}$  was taken from Ref. [38]. The blue rectangle tries to emphasize that the states quadruplet is formed by the coupling of odd proton to the  $2^+$  vibrational state from the neighboring nucleus.

show the particle-core coupling effects on the vibrational structure in odd-mass nuclei.

Since the quadrupole vibrations carry an angular momentum of 2 units, there can be two types of vibrations in a deformed nucleus: one which corresponds to  $K = 0$  and one for  $K = 2$ . For  $K = 0$  the vibrational motion is called  $\beta$ -vibration, and this induces small fluctuations in the quadrupole deformation parameter, but it preserves the axial symmetry of the nucleus (the vibration is aligned with the deformed axis).

The second type of vibration (for  $K = 2$ ) is called the  $\gamma$ -vibration which is responsible for fluctuations in the triaxiality parameter  $\gamma$ . A qualitative description for such an oscillation can be explained in terms of a physical object such as an American football [14]: if one pictures a nucleus with such a shape, then  $\gamma$ -vibrations will result in the simultaneous pushing and pulling of the ball on its sides, while

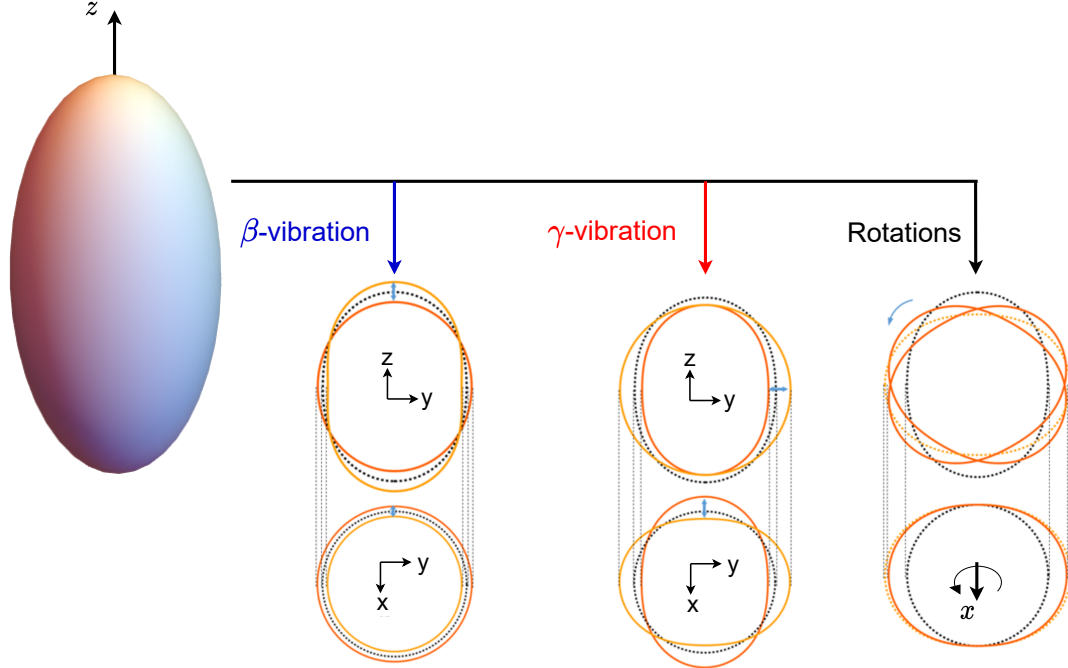


FIGURE 3.26: A sketch which shows the two types of vibrations in nuclei. The initial nucleus in this example is of prolate type. Each mode of vibration is visualized from the side-view and top-view, respectively. This figure was inspired (and also contains graphical elements) from Ref. [33]

the former vibrational mode will correspond to continuous pushing and pulling on the ends of the football. An illustration which aims at explaining the geometrical meaning of the  $\beta$  and  $\gamma$  vibrations in nuclei can be seen in Fig. 3.26.

### 3.4.3 Nuclear Rotation

The quantization procedure for the collective Hamiltonian is a tedious procedure which can be followed in the work of Corrigan et al. [39]. However, the only interest is for the rotational-kinetic term from  $H_{\text{coll}}$ . This term is called the *rotational energy*, and its expression is given by:

$$\hat{T}_{\text{rot}} = \frac{\hat{I}_1^2}{2\mathcal{I}_1} + \frac{\hat{I}_2^2}{2\mathcal{I}_2} + \frac{\hat{I}_3^2}{2\mathcal{I}_3}. \quad (3.58)$$

The three operators that appear in Eq. 3.58 are in fact the projections of the total angular momentum  $\mathbf{I}$  on the body-fixed axes (see Fig. 3.27 for reference). Note that throughout the text, the angular momentum will be interchangeably represented with an arrow or just by bold letters.

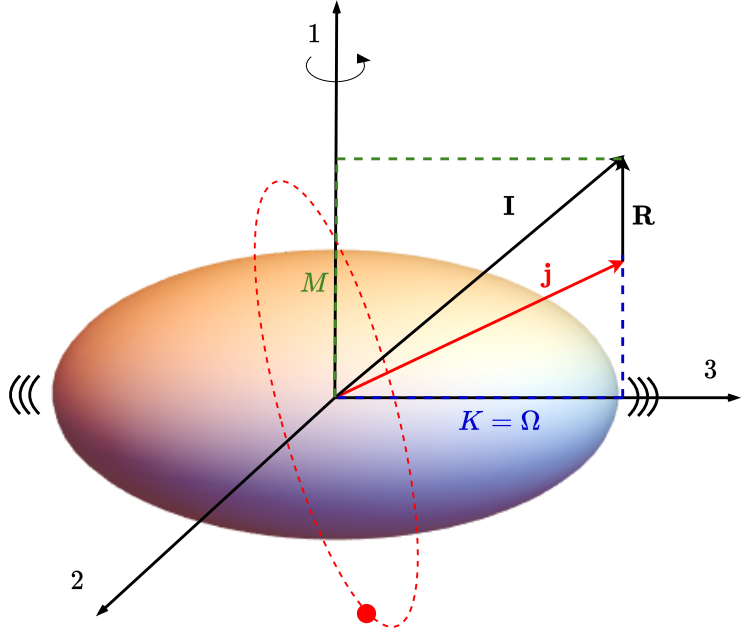


FIGURE 3.27: The coupling of the collective angular momentum with the angular momentum of a single-particle, for an axially deformed nucleus that is rotating about an axis perpendicular to the deformation axis.

An important conclusion which comes out from the work of Bohr and Mottelson [5] (also see discussion in Ref. [3]) is that no rotations are possible for spherical nuclei nor for axially deformed nuclei which are rotating about the symmetry axis. Consequently, a prior deformation (e.g., of quadrupole type) and a rotating axis which does not coincide with the symmetry one are required for the appearance of rotational levels. Indeed, every nucleus which contains energy states that are generated by the rotational motion has these bands due to the rotation about an axis that is different from the symmetry axis, and its shape is either axially-symmetric or axially-asymmetric [25].

A nucleus can generate angular momentum in two ways:

1. collectively, via combined rotations and vibrations of the nuclear droplet (the rotation+vibration spectrum of a nucleus will be shown in the next section)
2. single-particle excitations: unpaired nucleons can rearrange themselves in such a way that they account to the nuclear spin

The coupling of the rotational angular momentum  $\mathbf{R}$  of the droplet with the single-particle angular momentum of a valence nucleon  $\mathbf{j}$  can be seen in Fig. 3.27.

Based on the expression of  $T_{\text{rot}}$  from Eq. 3.53, its quantized form given in Eq. 3.58, and the coupling scheme depicted in Fig. 3.27, it is possible to construct a Hamiltonian that corresponds to rotating nucleus which has no valence particle. More precisely, the  $\mathbf{j}$  term is neglected, such that only the pure collective motion of a nucleus is emphasized ( $\mathbf{I} = \mathbf{R}$ ). This approximation is however only valid for even-even nuclei and for the low-lying states [18, 26]:

$$H = H_{\text{rot}} + H_{\text{intr}} = \sum_i \frac{\hbar^2}{2\mathcal{I}_i} R_i^2 , \quad (3.59)$$

where the second term  $H_{\text{intr}}$  represents some effects coming from the internal structure of the rotator itself. However, most of the time these terms can be neglected, leading to a rather simple energy spectrum for the even-even nuclei:

$$E_{\text{rot}}(I) = \frac{\hbar^2}{2\mathcal{I}_{\perp}} I(I+1) . \quad (3.60)$$

In the above expression, the MOI  $\mathcal{I}_{\perp}$  corresponds to an axis that is perpendicular to the symmetry axis (i.e., either 1-axis or the 1-axis) of the ellipsoid. In the case of axial symmetry both moments are equivalent, such that the general notation  $\mathcal{I}_{\perp}$  is made. As an observation, since there is no single-particle contribution, the quantized angular momentum  $I$  (or spin) is equivalent to  $R$ . The spectrum defined by Eq. 3.60 leads to energy spacings  $\propto I(I+1)$ , which is also met in the molecular spectra. The ground-state will always be the state  $0^+$ , and due to the mirror symmetry that is required for the wave-functions describing the even-even nuclei [4], every other excited state will be represented by an even value of the spin:  $2^+, 4^+, \dots$ . The ratio  $E(4^+)/E(2^+)$  for these bands is 3.33 (as it was previously mentioned). This is indeed the best signature for the rotational phenomena in nuclei, indicating a clear presence of deformation + rotational motion. In a previous work by the current team (Raduta et al.) [40], some spectra of even-even  $^{158}\text{Er}$  were studied and agreement with the observed experimental data was impressive. The energy spectra obtained from Eq. 3.60 has a classical counterpart which is known within literature as the *symmetric top*. Fig 3.28 shows some examples of rotational bands in even mass nuclei, where the  $K^p i = 0^+$  band head is the ground-state, and every excited state has  $\Delta I = 2$  units of angular momentum.

However, the spectra of a simple rigid rotator assumes that the projection  $K$  of the total angular momentum for the ground-state of even-even nuclei is  $K = 0$ . So

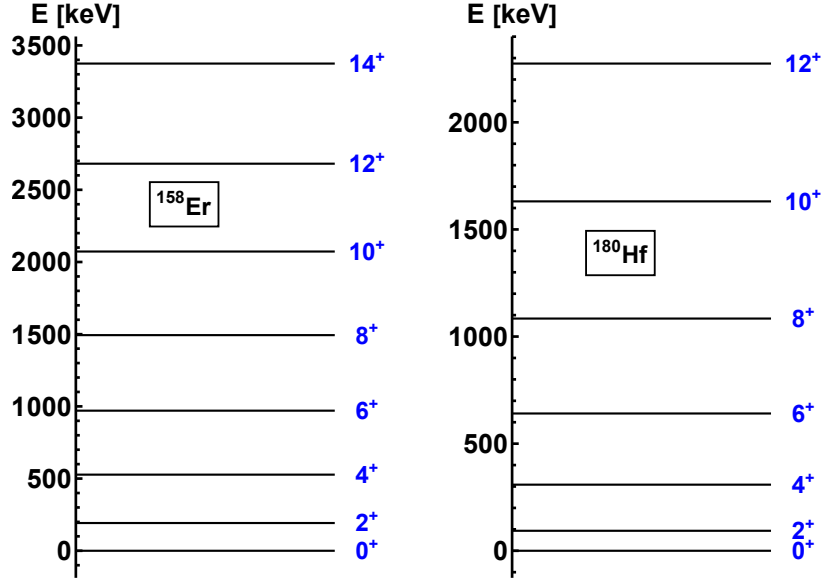


FIGURE 3.28: Experimental data showing the rotational bands in even-even nuclei. Note the spacing between the states that increases with  $I$  via the rule from Eq. 3.60. Experimental data are taken from Refs. [41, 42] for each nucleus.

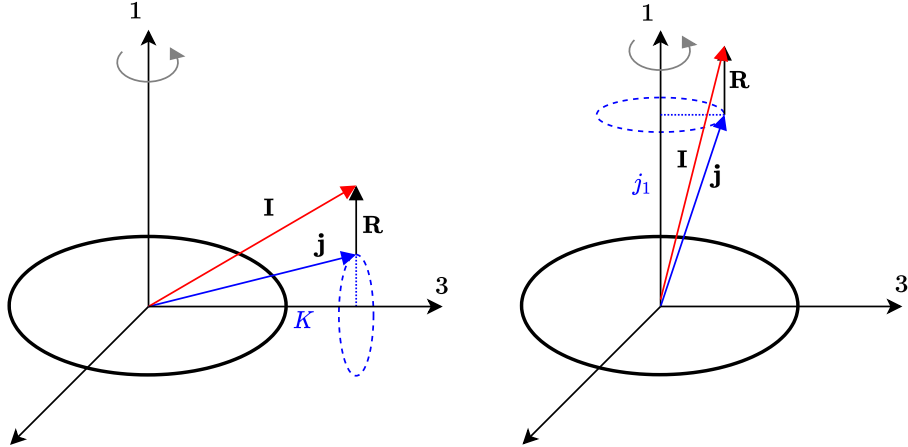


FIGURE 3.29: A sketch with the geometrical interpretation of the two ways a nucleus can exhibit rotational bands: Deformed Aligned Bands (**left**) and Rotation Aligned Bands (**right**). See text for explanations. The projections of the single-particle's total a.m. on the deformation and rotation axes are denoted with  $K$  and  $j_1$ , respectively.

the next step is to consider more general cases of nuclear rotation. There are two general cases of rotational bands that can occur, and both require the coupling scheme of a rotor with a valence nucleon, such that the angular momentum will be  $\mathbf{I} = \mathbf{R} + \mathbf{j}$  (so both situations will correspond to odd- $A$  nuclei). The two situations are called *Deformation aligned bands* and *Rotation aligned bands* [43]. Graphical representation with both rotational schemes can be seen in Fig. 3.29.

## Deformation Aligned Bands

This case is also referred to as *strong-coupling* limit [29] since the particle's a.m. is tightly coupled to the deformation axis (i.e., the symmetry axis). The general Hamiltonian will be:

$$H_{\text{rot}} = H_0 + H_{\text{coupl}} , \quad (3.61)$$

where  $H_0$  is the already discussed operator containing the squared components  $I_k$  of  $\mathbf{I}$  and the extra *coupling term* represents the Coriolis force [18]. The Coriolis effect is reflected by the coupling of the collective motion of the nucleus to the odd nucleon's motion. Despite that, it can be neglected at small rotations.

The projection of the particle's a.m. on the symmetry axis is a good quantum number, and if  $\mathbf{R}$  is pointing in a direction that is perpendicular to the deformation axis, then  $\Omega = K$ , meaning that the energy spectrum will be given by:

$$E_{\text{rot}}(I) = \frac{\hbar^2}{2\mathcal{I}_{\perp}} [I(I+1) - K(K+1)] , \quad (3.62)$$

or more formally:

$$E_{\text{rot}}(I) = \frac{\hbar^2}{2\mathcal{I}_{\perp}} [I(I+1) - K^2] + E_0(K) . \quad (3.63)$$

The rotational band will be constructed on the ground-state  $E_0(K)$ , where total spin  $I$  will be composed of a sequence  $I = K, K+1, K+2, \dots$  and  $K \neq \frac{1}{2}$ . Consequently, this situation will lead to rotational bands where the difference between two consecutive states is only one unit of angular momentum. It should be pointed out that odd- $A$  nuclei can have multiple rotational bands that are built on different values of  $K$ .

For  $K = \frac{1}{2}$ , the band structure will follow:

$$E_{\text{rot}}(I) = \frac{\hbar^2}{2\mathcal{I}_{\perp}} \left[ I(I+1) + a(-)^{I+\frac{1}{2}} \left( I + \frac{1}{2} \right) \right] . \quad (3.64)$$

The nature of  $(-1)^{I+1/2}$  will be explained for *Rotation Aligned Bands*. Moreover, the term  $a$  is called the *decoupling parameter* [18], and it can be determined from the first two experimental energy levels. Experimental data which point out the

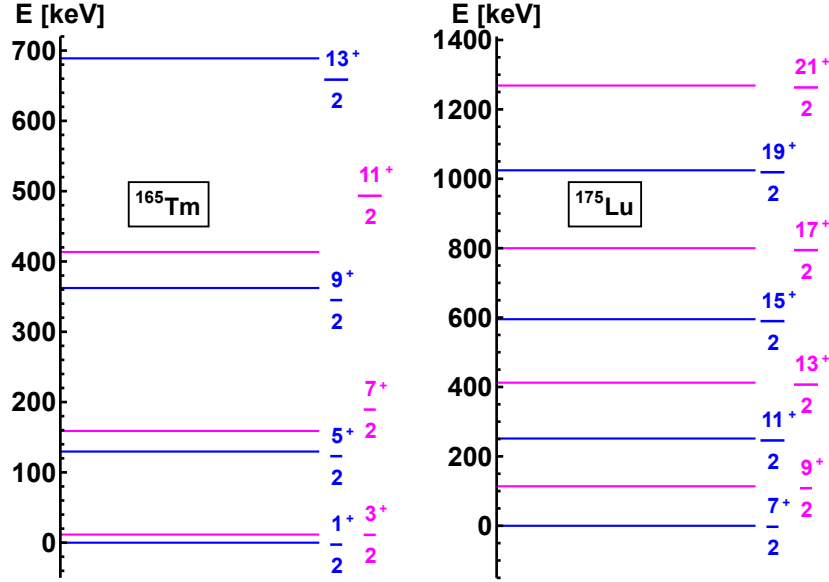


FIGURE 3.30: Rotational bands in odd- $A$  nuclei with the  $K$  quantum number equal to  $K = 1/2$  (**left**) and  $K \neq 1/2$  (**right**).

presence of rotational bands with  $K = 1/2$  and  $K \neq 1/2$  are shown in Fig. 3.30, for two odd- $A$  nuclei.

### Rotation Aligned Bands

This situation is also called the *decoupling limit* [1] and it leads to the apparition of *decoupled bands*. Here the total angular momentum is more aligned to the axis of rotation, and its maximum projection is along this axis. This is usually happening at high-spins, meaning strong rotational motion, which makes the angular momentum of the odd-particle to depart from the symmetry axis and align more and more with the direction of rotation (through the Coriolis effect). As such, the coupling term  $H_{\text{coupl}}$  from  $H_{\text{rot}}$  is not neglected here:

$$H_{\text{rot}} = \frac{\hbar^2}{2I_{\perp}} (\mathbf{I}^2 + \mathbf{j}^2 - 2\mathbf{I} \cdot \mathbf{j}) . \quad (3.65)$$

It is usually preferred to work with the *raising* and *lowering* operators which correspond to the angular momentum operator:  $\mathbf{I}_{\pm} = \mathbf{I}_1 \pm i\mathbf{I}_2$  (equivalently can

be done for  $\mathbf{j}$ ), bringing  $H_{\text{rot}}$  to the following expression:

$$H_{\text{rot}} = \frac{\hbar^2}{2\mathcal{I}_{\perp}} \hat{I}^2 + \frac{\hbar^2}{2\mathcal{I}_{\perp}} \hat{j}^2 - \frac{\hbar^2}{\mathcal{I}_{\perp}} K^2 + H_{\text{Coriolis}} , \quad (3.66)$$

$$H_{\text{Coriolis}} = -\frac{\hbar^2}{2\mathcal{I}_{\perp}} (\mathbf{I}_+ \mathbf{j}_- + \mathbf{I}_- \mathbf{j}_+) . \quad (3.67)$$

It is worth pointing out that the effect of the Coriolis term is to couple bands which differ in  $K$  quantum number with one unit, effect which is negligible at high deformations and low spins (since the single-particle motion is tightly bound to the bulk nucleus) while at very high rotations (spins) it becomes significant. Consequently, the Coriolis effect most probably occurs in prolate nuclei for an ‘almost empty’  $j$ -shells and oblate nuclei for an ‘almost full’  $j$ -shell.

When the single-particle angular momentum is orienting itself to the direction of rotation, the projection of  $\mathbf{j}$  can be denoted by  $j_1$  (keeping a consistency with Fig. 3.27). The spectrum of the decoupled bands will be:

$$E_{\text{rot}}(I) = \text{const.} + \frac{\hbar^2}{2\mathcal{I}_{\perp}} (I - j_1)(I - j_1 + 1) , \quad (3.68)$$

where the coupling terms have been embedded in the constant term. This leads to a spin sequence  $I = j_1, j_1 + 2, j_1 + 4 \dots$ , which differs from the previous case via the constant  $2\hbar$  angular momentum difference of two consecutive levels.

In order to understand the terms  $(-1)^{I+1/2}$  from Eq. 3.64, it is required to describe the wave-function corresponding to the particle-core system. Indeed, using the specific quantum numbers  $I, K, M$  with their meaning explained in Fig. 3.27, the wave-function will be written as a combination of rotational (the Wigner  $D_{MK}^I$  functions) and single-particle components [26, 44]:

$$\Psi_{MK}^I = |IMK\rangle = N [\phi_K D_{MK}^I + (-)^{I+K} \phi_{-K} D_{M-K}^I] , \quad (3.69)$$

where  $N$  is the normalization constant, usually having the value  $N_I = \sqrt{\frac{2I+1}{16\pi^2}}$ . This linear combination of states with  $K$  and  $-K$  induces a degeneracy and it is due to the invariance of such a system with respect to rotations by  $\pi$  around the rotational axis [1, 45]. The factor  $(-)^{I+K} \equiv \alpha$  is called the *signature* and it reflects whether a system is invariant or not to such a rotation. More precisely, the

*signature quantum number* is given as [46]:

$$\alpha_I = \frac{1}{2}(-)^{I-\frac{1}{2}}, \quad (3.70)$$

for a state of spin  $I$  in an odd- $A$  nucleus, resulting in the favored states having  $\alpha_{\text{favored}} = \frac{1}{2}$  and the unfavored states having  $\alpha_{\text{unfavored}} = -\frac{1}{2}$ .

Depending on the signature, the nuclear states can be divided into two sets: one that follows  $I = K, K+2, K+4, \dots$  and  $I = K+1, K+3, K+5, \dots$ . This is the reason why for the decoupled bands, one can regard them as an ‘initial’ rotational band  $I, I+1, \dots$  that is ‘broken’ apart in two sequences: one that is favored and one that is unfavored (opposite signature). An example is a nucleus with odd- $A$ , where the favored bands have spins  $I_{\text{favored}} = \frac{1}{2}, \frac{5}{2}, \frac{1}{2}, \dots$ , while their unfavored *partner* bands have spins  $I_{\text{unfavored}} = \frac{3}{2}, \frac{7}{2}, \frac{11}{2}, \dots$  and opposite signature (also known as *signature partners*). In fact, taking a closer look at the rotational bands specific to odd- $A$  nuclei shown in Fig. 3.30, each consecutive level is a state with different signature, meaning that each ‘group’ of colors classifies into a set of favored (blue) and unfavored (magenta) states.

This divided set of partner bands also has some characteristics that can be observed throughout experimental measurements. Firstly, the splitting of the two branches implies that the favored states will generally have lower excitation energy than their unfavored partners. This is also proved by the expression of the rotor energy given in Eq. 3.64, where the decoupling parameter will cause an upward (downward) shift in energy for states with  $I = 1/2, 5/2, 9/2, \dots$  ( $I = 3/2, 7/2, 11/2, \dots$ ), depending whether  $a$  is positive (negative). The experimental data shown in Fig. 3.31 shows how the favored partner lies lower with respect to its unfavored partner bands, each having the corresponding spin sequence  $\Delta I = 2$  for intraband states and  $\Delta I = 1$  for interband states. Such spectra are very often met in the decay schemes for odd-mass nuclei in which the rotational motion is governed by the (core+particle) coupling scheme.

### 3.4.4 Superimposed Rotations and Vibrations

Up until now, the two types of nuclear motion, namely the collective rotations and vibrations were discussed separately. The small vibrations of the nuclear surface lead to the presence of band structures constructed via the quadrupole phonons

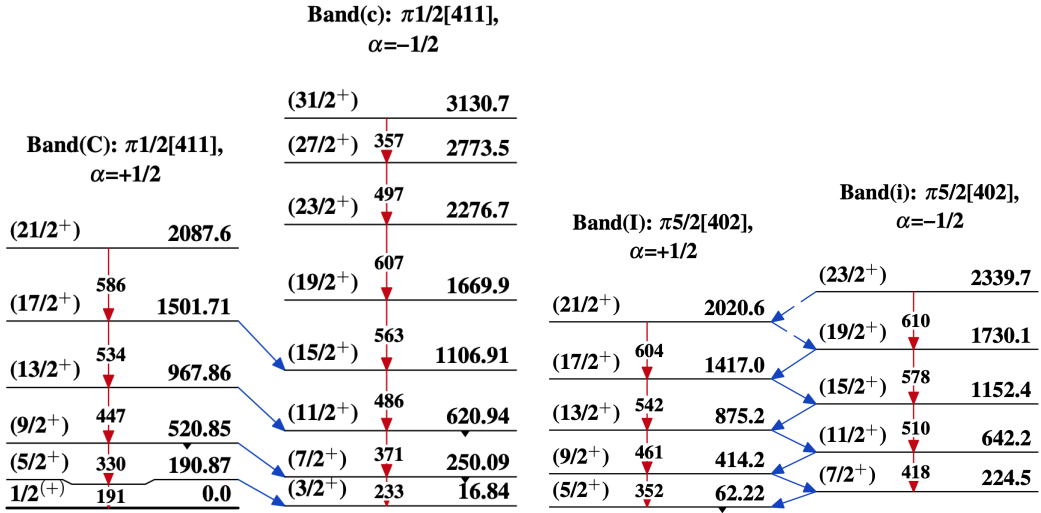


FIGURE 3.31: Experimental level schemes for  $^{163}\text{Lu}$  showing pairs of signature partner bands. **Left:** the two bands are built on a proton with  $j = 1/2$  and positive parity. **Right:** sequences built on a proton with  $j = 5/2$  with the same parity. The Nilsson quantum numbers are defined for each band. Note the spin difference between each state, as described in text. Also note the lower energies for the favored states. Interband transitions are marked with the blue arrows. The experimental data is from Ref. [47] and the level schemes were taken from Ref. [48].

carrying  $\lambda = 2$  units of angular momentum. The collective nature of the nucleus together with effects coming from the coupling a core to a valence nucleon also showed that some rotational band structures can appear in nuclei.

The proper picture of a rotating deformed nucleus consists of a stable *equilibrium shape* that is determined by the *rapid internal motion of the nucleons* within the nuclear potential and their entire distribution doing a *slow rotation*, such that it has negligible effect on the nuclear structure or on the individual nucleonic orbits.

Besides the two (separated) degrees of freedom for the nuclear system (i.e., collective rotation and vibrations), the two types of motion can be superimposed on each other, leading to specific spectra of the nuclei. One can describe this spectra starting from the expression of the *Collective Bohr's Hamiltonian* (remember calculations presented in Eqs. 3.45, 3.50, 3.52, and 3.53):

$$H_{\text{coll}} = T + V = T_{\text{vib}} + T_{\text{rot}} + V \quad (3.71)$$

Following the calculations from [33], a separation of the Hamiltonian terms in

three main components will be made: one associated to the  $\beta$ -vibration, one for  $\gamma$ -vibrational mode, and the third term is the rotation of a rigid rotor characterized by a total spin  $I$  and well-defined MOI  $\mathcal{I}$ . The total energy will generate the spectrum [4, 33]:

$$E_{n_\beta n_\gamma IK} = \hbar\omega_\beta \left( n_\beta + \frac{1}{2} \right) + \hbar\omega_\gamma \left( n'_\gamma + \frac{1}{2}|K| \right) + \frac{\hbar^2}{2\mathcal{I}} [I(I+1) - K^2] . \quad (3.72)$$

Note the two harmonic-like solutions making the vibrational mode present within the energy formula. The two ‘frequencies’ are given in terms of the stiffness and inertia parameters [33]:

$$\omega_\beta = \sqrt{\frac{C_0}{B_2}}, \quad \omega_\gamma = \sqrt{\frac{C_2}{B_2}}, \quad (3.73)$$

and the two quantum numbers are as follows:

$$n_\beta = 0, 1, \dots, \quad n'_\gamma = 2n_\gamma + 1, \quad n_\gamma = 0, 1, \dots . \quad (3.74)$$

The allowed values for the quantum numbers are as:

$$K = 0, 2, 4, \dots ,$$

$$I = \begin{cases} K, K+1, K+2, \dots & \text{for } K \neq 0 \\ 0, 2, 4, \dots & \text{for } K = 0 \end{cases} . \quad (3.75)$$

Consequently, the spectrum of a typical nucleus in which both vibration and rotation occurs has bands that are characterized by the set of quantum numbers  $K, n_\beta, n_\gamma$ , where the excited states follow the  $\propto I(I+1)$  rule. This collective spectrum is exemplified in Fig. 3.32. The main bands are:

1. the ground-state band, having states with even  $I$ , where excitation energies are constructed from the rotor term
2. the  $\beta$  band, starting above the g.s. band with  $\hbar\omega_\beta$  and containing only even spins
3. the  $\gamma$  band, corresponding to  $K = 2$  (as explained in a previous section). It is distinguished from the  $\beta$  band because it starts with  $2^+$  as first state and it contains both odd and even spins.

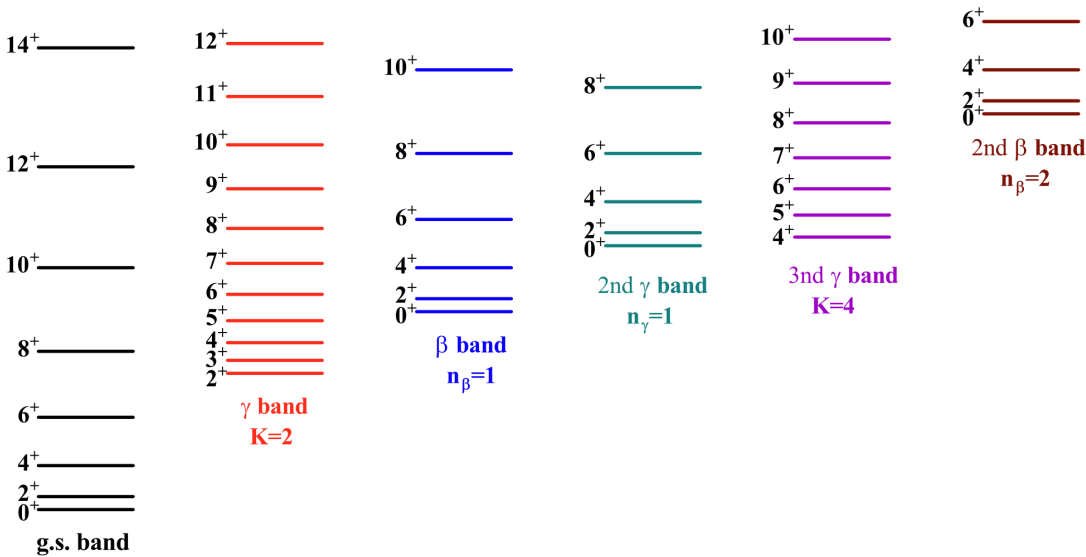


FIGURE 3.32: The energy spectrum specific to the *Rotation-Vibration* collective model. Each quantum number is also shown at the bottom of the bands. This figure is taken from Ref. [33].

4. the higher-level bands are the  $n_\gamma = 1$  and  $K = 4$  bands for  $\gamma$ -vibrational mode, and the  $\beta$  band with  $n_\beta = 2$ .

### 3.4.5 Collective Quantities

In this section, some important quantities will be described since their meaning is strictly related to the collective nature of nuclei. Indeed, one can understand nuclear deformation, energy spectra, and behavior with respect to spin of nuclei by studying quantities such as *rotational frequencies*, *moments of inertia*, *quadrupole moments*, and so on. As it will be shown, the values of such physical observables will point out, for example, if some nuclei experience large deformations, or if rotation causes the nucleus to exhibit excited states. Moreover, the comparison with experimental data for these quantities can help validate some assertions that are initially made, which is usually the crucial test of new models and frameworks that are developed by the nuclear physics community.

#### R - Energy Ratio

As discussed before, the energy ratio between the first excited  $4^+$  state to the first excited  $2^+$  state is a very good test for checking whether a nucleus ‘tends’ to

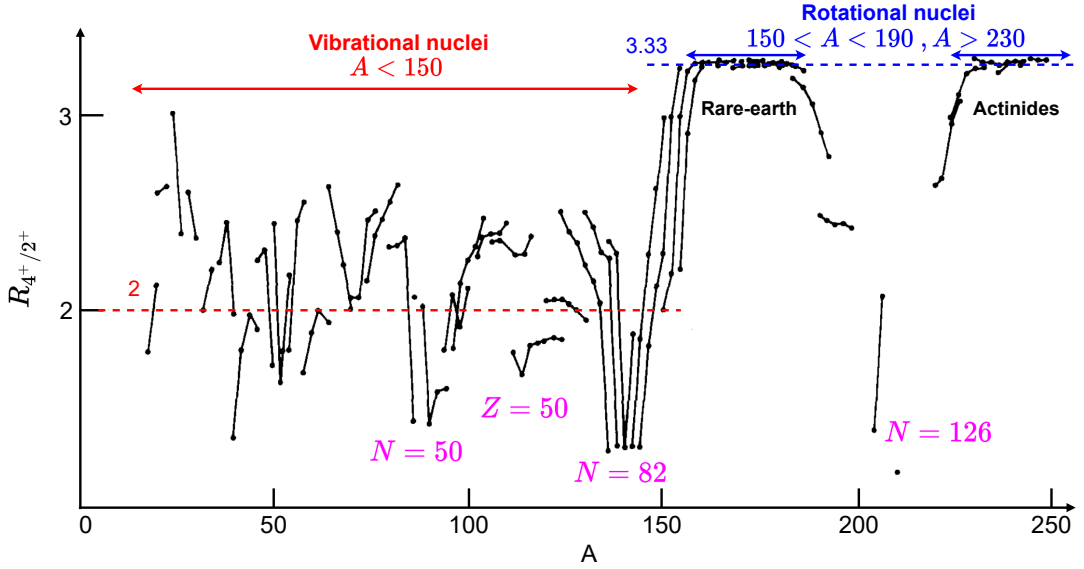


FIGURE 3.33: The experimental ratio  $R_{4+}/2^+$  in even- $Z$  and even- $N$  nuclei. Each line is connecting sequences of isotopes. Note the two important values for  $R_{4+}/2^+$ , namely 2 and 3.33 given for a perfect vibrational nucleus and a pure rotator, respectively. Text with magenta color marks the magic numbers for  $Z$  or  $N$ . This plot was adapted from Ref. [9].

show rotational or vibrational structures (i.e., spectra). Casten et al. [9] shows the evolution of this ratio across the mass number  $A$ , and a classification between *vibrational* vs. *rotational* character can be made. Fig. 3.33 contains the ratio  $R_{4+}/2^+$ .

### Rotational Frequencies

In the classical limit, the kinetic energy of a rotating object is described as a quadratic variation of the angular frequency  $\omega = l_{\text{cls.}}/\mathcal{I}$  (frequency of rotation around a particular direction) in the following way:

$$E = \frac{1}{2}\mathcal{I}\omega^2 , \quad (3.76)$$

which can also be given in terms of the angular momentum  $l_{\text{cls.}}$ , such that the final energy becomes  $E_{\text{cls.}} = l_{\text{cls.}}^2/(2\mathcal{I})$ . Quantum mechanically, it was shown that  $l^2$  is usually expressed as  $\hat{l}_{\text{quantum}}^2 = \hbar^2 I(I + 1)$ .

Bengtsson et al. [49] calculated the so-called Routhians (single-particle energies within the rotating frame of reference) and they found a *canonical relation* between

the energies and rotational frequencies:

$$\omega = \frac{dE(I)}{dI_x}, \quad (3.77)$$

where the term  $I_x$  is called the *aligned angular momentum*, and usually it denotes the experimental spin of every state minus a reference value (see Harris [50]). The signature property discussed previously (giving sequences with  $\Delta I = 2$ ) plays a pivotal role in determining  $I_x(I)$ , since the projection  $K$  of the angular momentum onto the deformation axis must be taken into account:

$$I_x(I) = \sqrt{\left(I + \frac{1}{2}\right)^2 - K^2}, \quad (3.78)$$

which for the  $K = 0$  bands reaches the simplified form  $I_x^2 = (I + \frac{1}{2})^2$ . The value of  $K$  is typically the band-head's angular momentum [49, 51].

A more concise definition for the quantity  $\omega(I)$  is related to the transition between two consecutive states  $I + 1 \rightarrow I - 1$  within a rotational band: a unique value of  $\omega$  is attributed to the spin  $I$ , which is defined as a mean value of the two angular momenta from the corresponding transition. Such a construction will yield a set of discrete points  $\omega(I)$ , and one can obtain a ‘continuous’ function  $\omega(I)$  together with its inverse  $I(\omega)$ , thus making the term  $I$  from Eq. 3.78 to be in fact  $I(\omega)$ .

The rotational frequency is used to represent many quantities which characterize collective motion and nuclear deformation. For example, representing the total angular momentum  $I$  (or the aligned one  $I_x$ ) as a function of  $\Omega$  can check whether multiple bands have the same nature. Moreover, as it will be shown in the following section, representing the MOI as function of  $\omega$  will also get an insight on the intrinsic structure of the nucleus and the coupling schemes involved in the occurrence of the excited spectra. Another interesting feature that is present in high-spin spectra of some nuclei is the so-called *backbending* phenomena, where due to the Coriolis effect, nucleons can suffer a de-pairing, leading to their angular momentum to orient along the rotational axis, thus leading to a sharp increase in the MOI [4, 52]. These kind of effects are correlated to high deformation, increased rotation, and change in the nucleonic alignment.

## Moments of Inertia

This is a crucial quantity which describes the degree of deformation for the nucleus (rotational ellipsoid), since the asymmetry between the three MOI dictates the shape of the nuclear matter (remember discussion from Chapter 2). It was already mentioned that it is possible to retrieve an *experimental* value for a moment of inertia by inferring the energy spacing between consecutive levels of a collective spectrum. A classification of types of MOI was done in Eq. 3.56, where the dependence of  $\mathcal{I}$  on the deformation parameters (and even the mass parameter  $B_\lambda$  that originates from the initial Bohr Hamiltonian 3.45) was shown.

In order to get values for MOIs from the experimental data, two quantities are required: the spins and energies of two consecutive levels within an excited spectrum. The most general expression for the MOI can be written as [53]:

$$\mathcal{I} = \frac{\hbar^2}{2} \left( \frac{dE}{dJ(J+1)} \right)^{-1}, \quad (3.79)$$

where the classical angular momentum  $J$  is related to its quantum equivalent via the correction  $J = I + 1/2$  (see Eq. 3.78). Practically, the derivative can be expressed in terms of the aligned angular momentum  $I_x$  defined above.

Moreover, there are two types of MOI which give information about the structure of nuclei with respect to spin: *kinematic MOI* and *dynamic MOI*. The kinematic MOI is given by [54]:

$$\mathcal{I}^{(1)} = \frac{\hbar I_x}{\omega} = \hbar^2 I_x \left( \frac{dE}{dI_x} \right)^{-1}. \quad (3.80)$$

One can see why the aligned angular momentum is important, since its variation w.r.t. the energies lead to theoretical determinations of the kinematic MOI. From the observed intraband  $E2$  transitions one can extract the (kinematic) moment of inertia via the rule:

$$\mathcal{I}^{(1)}(I - 1) = \hbar^2 \frac{2I - 1}{E_\gamma(I, I - 2)}, \quad (3.81)$$

where  $E_\gamma(I, I - 2)$  represents the energy difference between two consecutive levels  $E(I)$  and  $E(I - 2)$ . The dependence on  $I$  for this type of MOI makes its experimental determination to require some spin assignments to each state of the excited

spectrum. On the other hand, the dynamic moment of inertia is expressed as [54]:

$$\mathcal{I}^{(2)}(I) = \hbar \frac{dI_x}{d\omega} = \hbar^2 \left( \frac{d^2 E}{dI_x^2} \right)^{-1}, \quad (3.82)$$

while  $\mathcal{I}^{(2)}$  expressed in terms of the energy differences has the following form:

$$\mathcal{I}^{(2)}(I) = \hbar^2 \frac{4}{\Delta E_\gamma(I)} = \hbar^2 \frac{4}{E_\gamma(I+2, I) - E_\gamma(I, I-2)}. \quad (3.83)$$

Note that any calculations for the dynamical MOI does not require prior knowledge about the spin assignments of the energy states. These two types of MOI are usually represented as function of the rotational frequency  $\omega$ . Since the total spin  $I$  can be expressed as a function of rotational frequency, plotting the kinematic/dynamic MOI as function of angular momentum is also preferred. In the present work, these quantities are of high interest (graphical representations for different nuclei will be shown in a future chapter), their relative behavior will help characterize bands with similar nucleonic structure.

An alternative description of the quantitative analysis of these MOI can be done through the so-called *ab* formula [54, 55], where the energies corresponding to the rotational spectrum are parametrized as:  $E(I) = a \left( \sqrt{1 + bI(I+1)} - 1 \right)$ . Fitting the experimental data will produce a set of parameters ( $a, b$ ) that will be used to get expressions for the kinematic and dynamic MOI:

$$\mathcal{I}^{(1)} = \mathcal{I}_0 \left[ 1 - \frac{(\hbar\omega)^2}{a^2 b} \right]^{-1/2}, \quad (3.84)$$

$$\mathcal{I}^{(2)} = \mathcal{I}_0 \left[ 1 - \frac{(\hbar\omega)^2}{a^2 b} \right]^{-3/2}, \quad (3.85)$$

with the factor  $\mathcal{I}_0$  defined as the *band-head* moment of inertia:  $\mathcal{I}_0 = \frac{\hbar^2}{ab}$ . In fact, such an approach of determining the MOIs of several odd- $A$  nuclei will consist in a future work of the same team.

As mentioned, the sharp or abrupt irregularities of the MOI with respect to the increase in rotational frequency is known as backbending. The Figs. 3.34–3.35 show some experimental data in which the quantity  $\frac{2\mathcal{I}}{\hbar^2}$  as function of the squared rotational frequency is graphically represented.

Indeed, by looking at the evolution of  $\mathcal{I}$ , some sharp increases are noted, and usually these are attributed to the centrifugal stretching in the rotational model

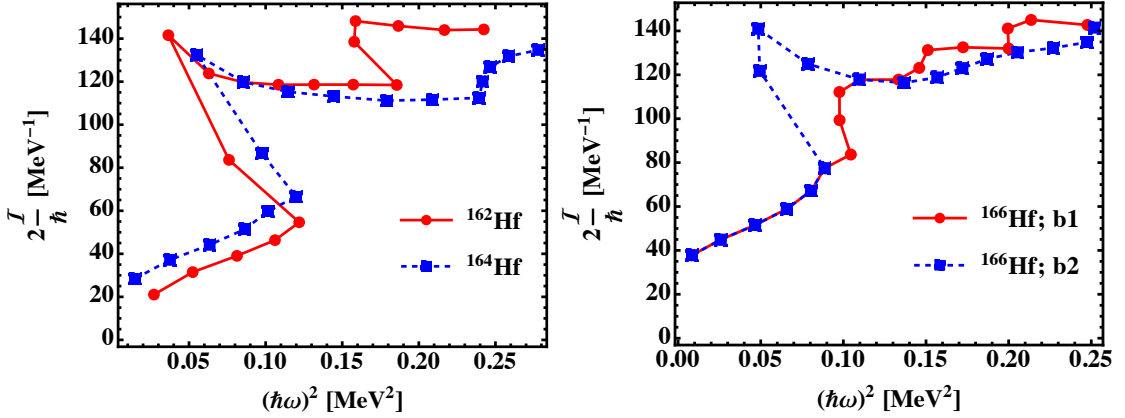


FIGURE 3.34: The moment of inertia as a function of rotational frequencies for three even-even nuclei. **Left:** The MOI for  $^{162,164}\text{Hf}$  nuclei, with their corresponding rotational ground-state bands. **Right:** The MOI for the first two rotational bands in  $^{166}\text{Hf}$ . Experimental data for these two nuclei are taken from Ahmad et al. [53].

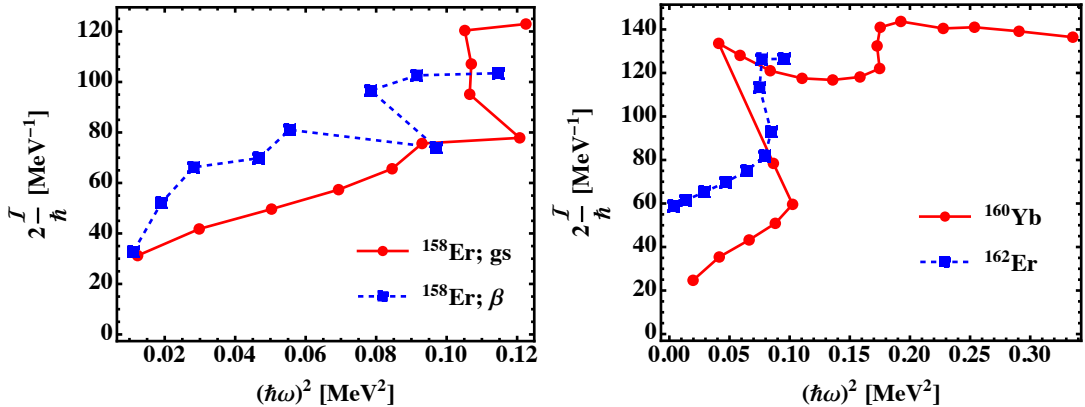


FIGURE 3.35: **Left:** The MOI for  $^{158}\text{Er}$  nucleus, with the ground-state band  $K^\pi = 0^+$  and the  $\beta$ -vibrational band with the same quantum numbers. Experimental data taken from [41]. **Right:** The MOI for  $^{160}\text{Yb}$  compared with  $^{162}\text{Er}$ . Experimental data taken from [56] ( $A = 158$ ) and [57] ( $A = 162$ ).

[58]. Moreover, the constant increase in  $\mathcal{I}$  is considered to happen due to the slow and constant quenching of the pairing correlations between nucleons (as already discussed in terms of the Coriolis effect at high spin) [59]. The abrupt changes are explained as rapid phase transitions of the nucleonic matter [60] exclusively due to the Coriolis Anti Pairing effect (example for some even-even nuclei in Ref. [61]). On the other hand, backbending can be also explained via the ‘band crossing’ of two intersecting bands which have different moments of inertia, and due to the same *non-crossing* effect which was explained in the two-state mixing, they only approach each other as much as the interaction strength allows [4]. Nevertheless, it is clear that theoretical investigations point out the reduction of pairing correlations that will affect the MOI values at low spin values, then alignment of

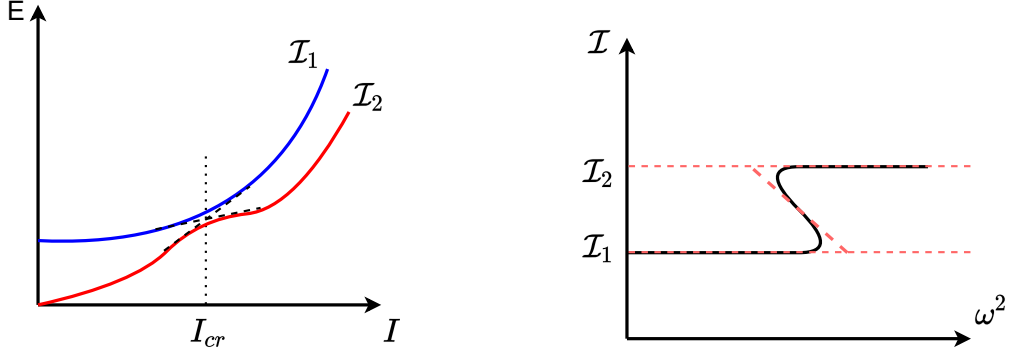


FIGURE 3.36: An illustrative example with two bands that are interacting with each other, leading to backbending. This sketch was inspired from the work of Ring et al. [4].

nucleons will eventually cause backbending [62, 63]. The band crossing is shown in Fig. 3.36. This phenomenon starts from the idea of two bands with different moments of inertia: if one analyzes the plot of the energies w.r.t. the angular momentum  $I$ , at one point (a *critical value* for  $I$ ), the second band would intersect the first one, crossing it. But such a thing is forbidden, so there will be a change in behavior for the parabolas (left side plot from Fig. 3.36), causing a simultaneous increase in total angular momentum and decrease in rotational frequency. This change in behavior is superimposed with the change in structure of the bands themselves, making the sharp transition possible. For small interaction strength between the two bands, the backbending will be quite ‘strong’, while for large values the transition region is very broad, making the backbending non-occurring.

Usually, the graphical representation of the MOI (kinematic or dynamic) as function of  $\omega$  (or, equivalently,  $I$ ) is useful when comparing multiple excited states for the same nucleus. By their ‘arrangement’ (behavior w.r.t. rotational frequency or spin), one can determine if bands belong to the same intrinsic structure, or if their deformed nature is similar. For example, after spin and parity assignments of each energy state within the collective spectra of the odd- $A$  nucleus  $^{163}\text{Lu}$ , it is of interest to see how many sequences have *normal deformation*, which single-particle + core couplings are preferred, if the bands have enhanced (strong) deformation, and so on. In the following chapters, a detailed overview with the evolution of the kinematic and dynamic MOI as a function of rotational frequencies for odd- $A$  around  $A \approx 160$  nuclei will be made, since it plays a major role in the study of highly deformed nuclei.

## Electric Quadrupole Moment

One of the most important indicators of stable nuclear deformation is a large value for the *electric quadrupole moment* [25]. The most general expression for the intrinsic quadrupole moment of a nucleus which is rotating about its  $z$ -axis is given in terms of its *charge density distribution*:

$$Q_0 = \int (3z^2 - r^2) \rho(r)_{\text{charge}} dv . \quad (3.86)$$

This shows how the nuclear charge distribution inside the nucleus is a crucial indicator of deformations. Note this  $z$  notation for a rotating axis is used here just for consistency with the textbook expression of  $Q_0$  [9]. Indeed, a relationship between the deformation parameter  $\beta$  and the quadrupole moment itself can be approximated (in second order of  $\beta$ ) as:

$$Q_0 = \frac{3}{\sqrt{5\pi}} R^2 Z \beta (1 + 0.16\beta) , \quad (3.87)$$

where  $R$  is given as  $R = R_0 A^{1/3}$ . For the  $\beta$  values that correspond to proper deformed nuclei (i.e.,  $\beta \approx 0.3$ ), higher order terms are not necessary. Remember that  $\beta$  describes the eccentricity of the deformed ellipsoid (albeit prolate or oblate), while the difference between prolate and oblate shapes is that for prolate (oblate) case there is an extension in one (two) direction and a squeezing in the other two (one). Depending on the value of  $\beta$ , the quadrupole moments for nuclei will be positive (indicating a stable prolate deformation) and negative (for stable oblate deformations). Fig. 3.37 shows some experimental values for some nuclei within the rare earth region.

In order to understand the behavior of  $\beta$  shown in Fig. 3.37, some shell model considerations need to be taken into account. Firstly, when deformation kicks in, the individual  $j$  orbits within a major shell are nearly empty, resulting in positive values for the quadrupole moments of the nucleons from these orbits. With increasing deformation, large and positive values  $Q(\beta)$  are present. Furthermore, as the shells start to fill, contributions from individual  $j$  orbits to the total quadrupole moment will accumulate, making its value to decrease, vanish, and eventually becoming negative near the shell closure.

The *observed* quadrupole moment (measured, also known as spectroscopic) can be obtained via a transformation to the laboratory frame applied to  $Q_0$ , meaning

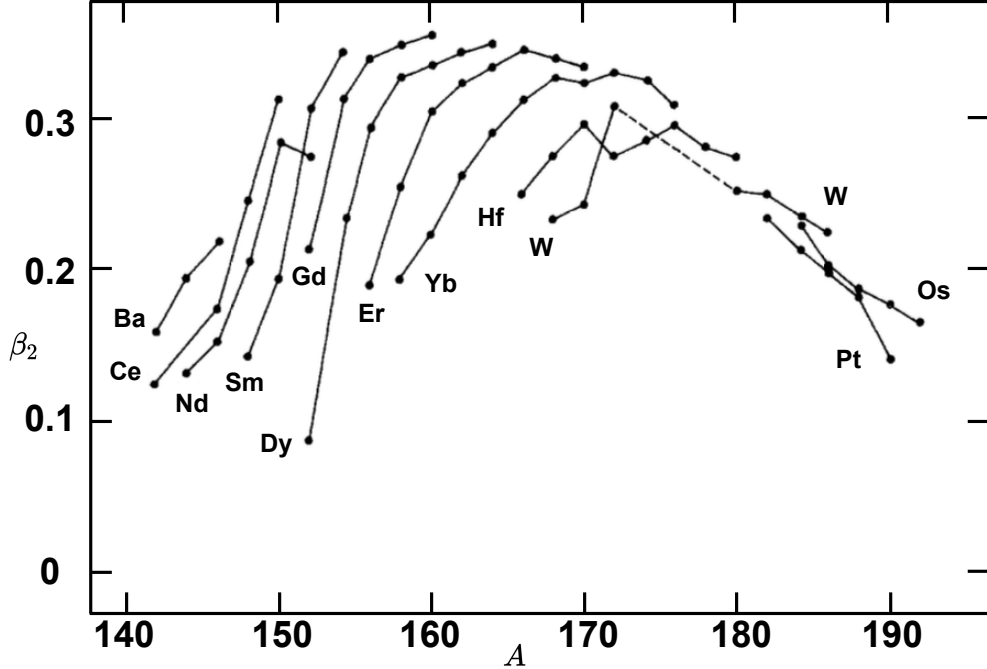


FIGURE 3.37: Experimental values for the quadrupole deformation parameter  $\beta_2$  as a function of the mass number  $A$  for a few isotopes. The values of  $\beta_2$  were determined from the experimental values  $B(E2; 0_i^+ \rightarrow 0_f^+)$ . Experimental data points were taken from Ref. [14].

that the spectroscopic quadrupole moment has the result [9]:

$$Q_{\text{spec}} = Q_0 \left[ \frac{3K^2 - I(I+1)}{(I+1)(2I+3)} \right] , \quad (3.88)$$

where the quantum number  $K$  is again the projection of  $I$  onto the symmetry (deformation) axis. The dependence of  $Q_{\text{spec}}$  on  $K$  and  $I$  emphasizes the fact that the *observed* shape of the rotating nucleus is not equivalent to the shape in the intrinsic frame of reference.

Remarking the fact that when prolate nucleus rotates about an axis that is perpendicular to the symmetry axis, the *averaged* density distribution of the nuclear matter will look more like an oblate shape (see Fig. 3.38 for a clearer picture). As a result, when the intrinsic quadrupole moment is positive, the observed one will have a negative value: for the condition  $I(I+1) > 3K^2$  taken from Eq. 3.88.

Another important quantity that can be used as a ‘test’ for collectivity and deformation within nuclei is the  $E2$  transition probability (of electric quadrupole type). This is because the ground state of even-even nuclei is  $0^+$  and the first excited state (typically  $2^+$ ) can only decay via the electric quadrupole interaction (as  $E2$

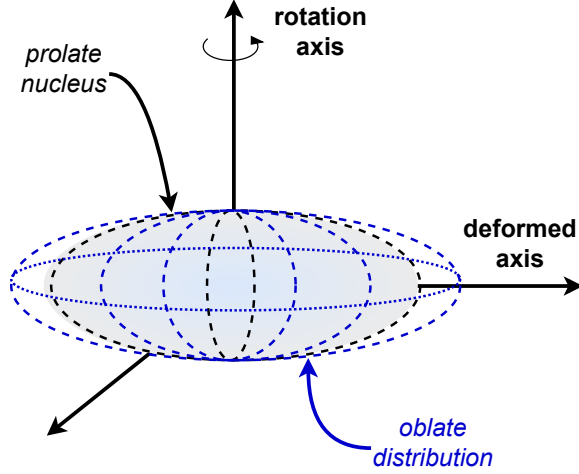


FIGURE 3.38: An example which aims at depicting an average flattened (oblate) density distribution that is generated by the rotation of a prolate nucleus. As the ‘initial’ prolate nucleus with its nuclear density is distributed along the deformed axis exhibits rotation, the rotated shape will generate an averaged oblate disk along the rotation axis. This is why the observed quadrupole moment will have a negative sign if  $Q_0 > 0$ .

radiation [9]), meaning that deformation effects can be understood from these low-lying transitions. The general expression for calculating a transition ‘strength’ is given in terms of the initial and final states [8]:

$$B(E2; I_i \rightarrow I_f) = \frac{1}{2I_i + 1} |\langle \Psi_f | \mathcal{M}(E2) | \Psi_i \rangle|^2 , \quad (3.89)$$

where the two wave-functions represent the initial and final state, respectively, and  $\mathcal{M}(E2)$  is the quadrupole transition operator. In fact, Eq. 3.89 tells that the reduced transition probabilities can be extracted from the ‘matrix elements’ of the electric quadrupole operator. Equivalently, the reduced quadrupole transition probability  $B(E2)$  can be given in terms of the Clebsch-Gordan coefficients [1]:

$$B(E2; I_i \rightarrow I_f) = \frac{5}{16\pi} e^2 Q_0^2 |\langle I_i K 20 | I_f K \rangle|^2 , \quad (3.90)$$

where the coefficient can also be written as  $\langle I_i K 20 | I_f K \rangle \equiv C_{K0K}^{I_i 2 I_f}$ . In the case of  $0^+ \rightarrow 2^+$ , the reduced transition probability will be given by:

$$B(E2; 0^+ \rightarrow 2^+) = \frac{5}{16\pi} e^2 Q_0^2 . \quad (3.91)$$

From the quadratic dependence of the intrinsic quadrupole moment on  $\beta$ , large values of  $\beta$  that are specific to deformed nuclei ( $\beta \approx 0.3$ ) will lead to values for

$B(E2)$  which are one-two orders of magnitude higher than those specific to nearly spherical nuclei ( $\beta \approx 0.05$ ). Such a systematic is the main cause why higher  $B(E2)$  values indicate large nuclear deformations.

In nuclei, usually the valence nucleons are causing some core polarizations, which as a result will affect the ‘final’ electric quadrupole moment. In fact, the single-particle quadrupole moment is given by the following expression:

$$Q_{\text{sp}}(j) = -\frac{2j-1}{2j+2} \frac{e_{\text{eff}}}{e} \langle r^2 \rangle . \quad (3.92)$$

The need for an *effective charge*  $e_{\text{eff}}$  is discussed in [64]. The mean squared radius corresponds to the radial function of the nucleon within that  $j$  orbital. Due to the nuclear energy being minimal (when discussing stable deformation) only if the overlap of the core with the valence particle is maximal, a particle+core interaction will produce an oblate polarization, driving the nucleus to a final oblate deformed state. The opposite is true for the hole+core coupling (see discussion made in [65]).

An interesting characteristic which emerges from Eq. 3.92 is the fact that besides even-even nuclei with  $I = 0$ , odd- $A$  nuclei the total spin  $I = \frac{1}{2}$  will be zero. The experimental data from Fig. 3.39 show the magnitude of  $Q$  which would correspond to the value given by Eq. 3.92. One can see sharp increase with the nucleonic number for some nuclei (e.g.,  $^{175}\text{Lu}$  or  $^{167}\text{Er}$ ) but also very strong decrease to negative values (e.g., the isotope  $^{123}\text{Sn}$ ). These alternations between positive (prolate) and negative (oblate)  $Q$  values are also located near the magic numbers. Moreover, one should note that for the cases when the odd-particle is a neutron, the nucleus still exhibits a quadrupole moment that is different from zero, meaning that not only the last nucleon will be responsible for the quadrupole moment [18].

The experimental data for the measured  $Q_{\text{spec}}$  values (the spectroscopic quadrupole moment in units of *barn*) for the lowest  $2^+$  states of even- $Z$  and even- $N$  nuclei is also graphically represented in Fig. 3.40, where both positive and negative values are observed. As already explained, a negative value for  $Q_{\text{spec}}$  (say for example  $Q_{\text{spec}} = -2$  b, for nuclei with stable permanent deformation which belong to the mass range  $150 \leq A \leq 190$ ) will correspond to an intrinsic quadrupole moment  $Q_0 = 7$  b. This will correspond to a quadrupole deformation parameter  $\beta \approx 0.29$ . Such values indicate substantial eccentricities of the nuclear matter.

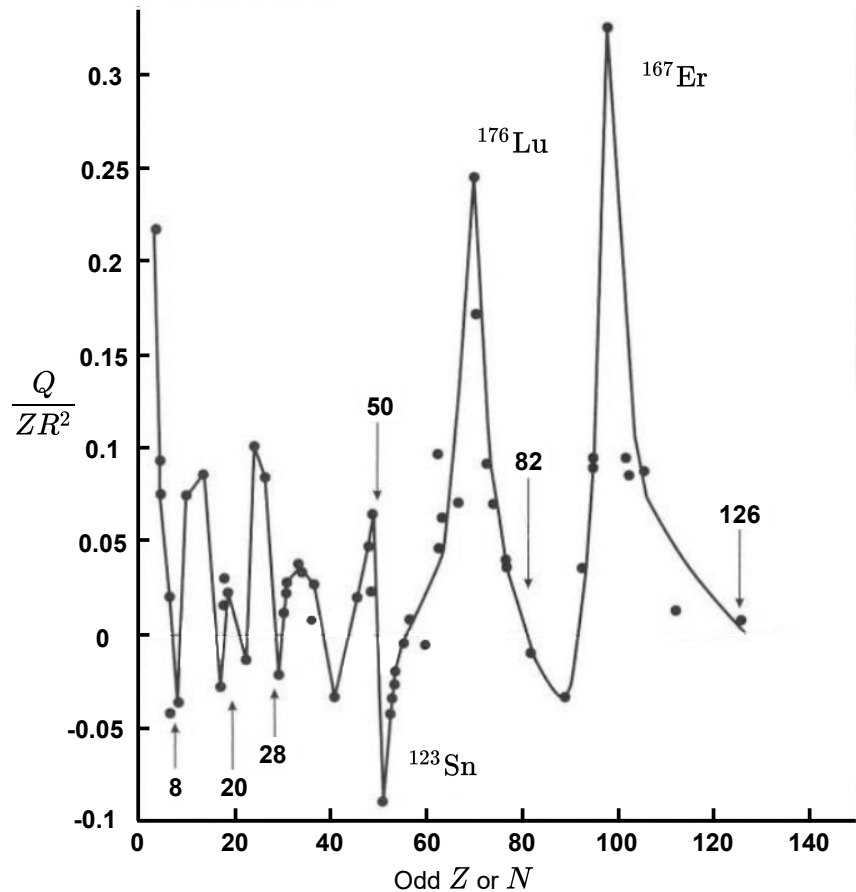


FIGURE 3.39: The measured quadrupole moments, given in units of  $ZR^2$ , as a function of the odd proton and neutron numbers  $Z,N$ , respectively. Experimental data are taken from Ref. [18].

With this, all the requirements for going to the next step are met, where a discussion about the loss of symmetry in nuclei will take place. The phenomena associated with lack of any axial symmetry - *nuclear triaxiality* - that are present in some deformed (stable) nuclei will be also shown.

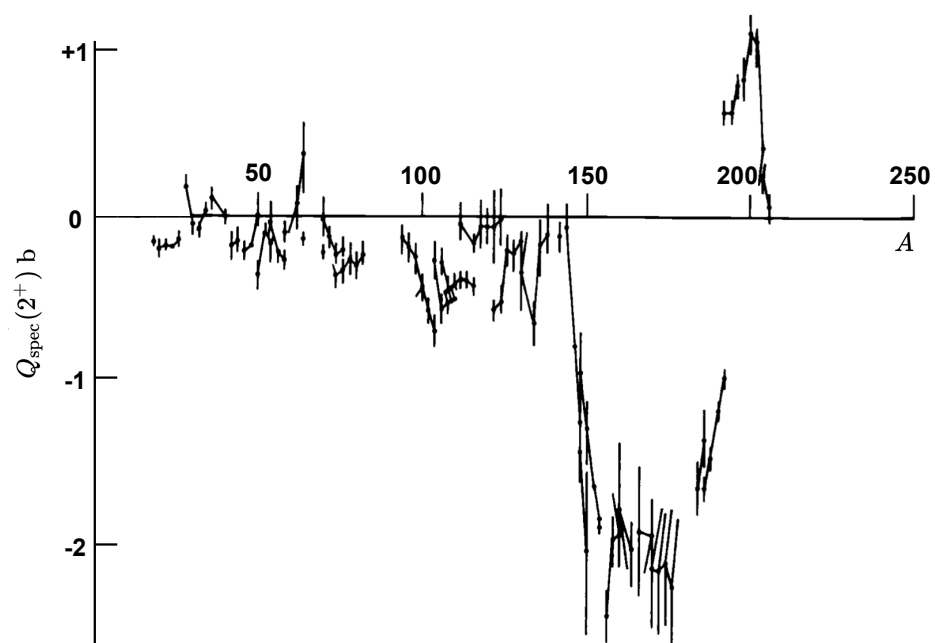


FIGURE 3.40: The measured quadrupole moment  $Q_{\text{spec}}$  as defined in Eq. 3.88 for the first excited  $2^+$  states in even-even nuclei. The lines between data-points connect the isotope sequences. The figure was reproduced with the experimental data from [14].

# Chapter 4

## Triaxial Nuclei and Their Signatures

In the following chapter, some theoretical background that is necessary for understanding triaxiality will be presented, with examples from literature and also some results obtained by this team. It is also instructive to realize why the nuclear community focuses their attention to the highly deformed nuclei, and moreover, nuclei which depart so much from the spherical shapes that they become *triaxial*.

Presenting the theoretical formalism that is used to describe triaxial nuclei, and mention the *fingerprints* of nuclear triaxiality is that last step before diving into the recently developed framework for odd- $A$  nuclei which the team created, and showing the results.

### 4.1 Non-axial nuclei

The discussion regarding excitation energies of a rigid rotator from the previous chapter was focused on pure rotators or nuclei with axially symmetric shapes (i.e., prolate or oblate). Remember that deformation is still required in order to define a collective spectra with rotational character. Moreover, the relevant quantities that are involved in the rotational motion for a deformed nucleus are the moments of inertia corresponding to the principal axes of the deformed ellipsoid:  $\mathcal{I}_{1,2,3}$ , and within previous calculations, two moments of inertia were supposed to be identical.

Even though calculations are performed with the rigid-like MOI or the irrotational-like, their dependence on the deformation parameters  $\beta_2$  and  $\gamma$  is present (recall expressions given in Eq. 3.56). Taking a closer look at their evolution with  $\gamma$ , one can see that indeed, identical MOI can only occur at certain values (see Fig. 3.22). As such, the nuclei can be regarded (when referring to their ground state) as such:

- **Spherical:** all MOI are identical and no deformations are present
- **Axially-symmetric:** two identical MOI and only the  $\beta_2$  parameter plays a role in the collective phenomena of these nuclei
- **Triaxial (Axially-asymmetric):** all three MOI are different (usually one of them is very large when compared to the other two), the quadrupole deformation parameter as well as the triaxiality parameter  $\gamma$  are present

Now, across the chart of nuclides, most of the isotopes are either spherical either symmetric in their ground state [66], but triaxial shapes might also occur as ground-state [67]. The apparition of triaxial nuclei implies some kind of ‘stability’ on the  $\gamma$ -parameter, since a dynamical character of the triaxiality will indicate some transitional states rather than nuclear stability. Indeed, a rigid (fixed) value for  $\gamma$  is required around the minimal region of the potential energy surface such that triaxial stable nuclei can exist. Thus, one can distinguish between the  $\gamma$ -soft nuclei in which this parameter has a dynamical character and the  $\gamma$ -rigid ones, which could in fact exhibit stable triaxial deformation [68]. Even more interesting are the structures which occur at very large values of quadrupole deformation  $\beta_2$  and  $\gamma$  in the vicinity of  $\approx 30^\circ$  (where maximal triaxiality occurs). It will be shown that these last nuclei will lead to band structures that are called *Triaxial Strongly Deformed* bands (TSD for short) [69, 70].

Concluding, the triaxial nuclei are a special class of nuclei in which there is an asymmetry between the moments of inertia (given by a  $\gamma$  value within the corresponding interval), and moreover, the quadrupole deformation is high enough such that it stabilizes the entire system.

### 4.1.1 Triaxial Rotor Model

The most general Hamiltonian for a *triaxial system* is given in terms of the components of the total angular momentum operator  $\hat{I}$  and the moments of inertia for the deformed ellipsoid, similarly as it was the case for the *rotational Hamiltonian* within the symmetry case:

$$\hat{H} = \frac{\hat{I}_1^2}{2\mathcal{I}_1} + \frac{\hat{I}_2^2}{2\mathcal{I}_2} + \frac{\hat{I}_3^2}{2\mathcal{I}_3} , \quad (4.1)$$

where the indices correspond to each of the principal axes of the rotational ellipsoid (principal axes are the ones in which the components of the MOI tensor are diagonal). More often, the notations  $A_{1,2,3} = \frac{\hbar^2}{2\mathcal{I}_{1,2,3}}$  are used in the Hamiltonian's expression, leading to  $A_1 \neq A_2 \neq A_3$  for the triaxial nuclei. Shi et al. [71] show a very straightforward way of obtaining the eigenvalues for the *triaxial rigid rotor*, following the quantum treatment made by Davydov and Filippov for the rigid rotor without symmetry axis [26]:

$$\begin{aligned} \hat{H} &= \hat{H}_{\text{diag}} + \hat{H}_{\text{non-diag}} , \\ \hat{H}_{\text{diag}} &= \left[ \frac{1}{2} (A_1 + A_2) (\hat{I}^2 - \hat{I}_3^2) + A_3 \hat{I}_3^2 \right] , \\ \hat{H}_{\text{non-diag}} &= \frac{1}{4} (A_1 - A_2) (\hat{I}_+^2 + \hat{I}_-^2) . \end{aligned} \quad (4.2)$$

This way of expressing the Hamiltonian is useful because there is a clear difference between a term which is diagonal and one that mixes states with different  $\Delta K = \pm 2$  quantum number. It is important to emphasize that this kind of Hamiltonian is still invariant to rotations with  $\pi$  around the principal axes. This is useful because one can solve the eigenvalue problem with the basis  $|IMK\rangle$ , were the wave-function is described as:

$$|IMK\rangle = \sqrt{\frac{2I+1}{16\pi^2(1+\delta_{K0})}} [|IMK\rangle + (-)^I |IM-K\rangle] , \quad (4.3)$$

where  $|IM \pm K\rangle$  are the Wigner  $D_{MK}^I$  - functions that determine the *orientation* of the nucleus itself (their are functions of the three Euler angles), the  $K$  quantum number is the projection of  $I$  onto the 3-axis of the body-fixed frame (intrinsic frame of reference), and the  $M$  number represents the projection of  $I$  onto the  $z$ -axis of the laboratory frame. This wave-function is quite similar to the one

defined in Eq. 3.69, when the decoupled states in the Rotation Aligned Bands were studied. Indeed, using this basis, the total Hamiltonian can be diagonalized [71] as such:

$$\hat{H}_{IK} = \frac{1}{2}(A_1 + A_2) [I(I+1) - K^2] + A_3 K^2 , \quad (4.4)$$

with the notation  $H_{IK} \equiv \langle IK | \hat{H} | IK \rangle$ . The second, non-diagonal term will have the energy states given as:

$$\hat{H}_{IK\pm 2} = \frac{1}{4}(A_1 - A_2)\sqrt{(I \mp K)(I \pm K + 1)(I \mp K - 1)(I \pm K + 2)} , \quad (4.5)$$

where  $\hat{H}_{IK\pm 2} \equiv \langle IK | \hat{H} | I \pm K \rangle$ . Finally, using these matrix elements, the energies can be obtained by solving the eigenvalue equation for given spins  $I$ . Such calculations were performed by the team for an even-even nucleus  $^{158}\text{Er}$  (see Fig. 8 from [40]) and the results of the diagonalization procedure were in complete agreement with alternative descriptions for  $\hat{H}$ .

#### 4.1.2 Triaxial Particle + Rotor Model

In this section, a general discussion about the Hamiltonian for a system which is composed on one single-particle (valence nucleon) in a high- $j$  shell and one triaxial core. Usually, such a treatment will be applied to odd- $A$  triaxial nuclei, and in fact the team's developed framework is founded on the triaxial PRM [26]. Davydov et al. developed this model for explaining the low-lying collective spectra of  $2^+$  states within some transitional nuclei.

The Hamiltonian of this system will be composed of a term which corresponds to the even-even core and that of a single-particle which is moving in a quadrupole deformed mean-field (remember that quadrupole deformation are the only relevant effects when discussing triaxial structures).

$$\hat{H} = \hat{H}_{\text{rot}} + \hat{H}'_{\text{sp}} . \quad (4.6)$$

Here, an important remark must be done regarding the notation of the terms. Usually, the single-particle Hamiltonian is composed of a term that gives the *intrinsic* energy coming from the  $j$  shell in which the nucleon is orbiting (one can

think of it as representing the Fermi energy level) and a term that characterizes the effective interaction between the particle and the deformed mean-field generated by the core. Consequently, the Hamiltonian  $\hat{H}'_{\text{sp}}$  should be written as:

$$\hat{H}'_{\text{sp}} = \hat{h}_0^j + \hat{H}_{\text{int}}^{\text{quad}} ,$$

where  $\hat{h}_0^j$  is the formerly described term and  $\hat{H}_{\text{int}}^{\text{quad}}$  is the latter. For example, Ring et al. [4] uses the SHO for describing  $\hat{h}_0^j$ . The interaction Hamiltonian is in fact a  $\gamma$ -deformed Nilsson potential, which was previously discussed (see Section 3.3.1), with its general expression in this case written as:

$$\hat{H}_{\text{int}}^{\text{quad}} = \kappa \beta r^2 \left[ \cos \gamma Y_2^0 + \frac{\sin \gamma}{\sqrt{2}} (Y_2^2 + Y_2^{-2}) \right]. \quad (4.7)$$

However, this generalized expression can be written for the single-particle characterized by its total angular momentum  $\mathbf{j}$  in the following way:

$$\hat{H}_{\text{int}}^{\text{quad}} = \frac{V}{j(j+1)} \left[ \cos \gamma (3j_z^2 - \mathbf{j}^2) - \sqrt{3} \sin \gamma (j_x^2 - j_y^2) \right] , \quad (4.8)$$

where the entire interaction strength between the particle and the core is embedded within the value of a parameter (usually adjustable) called *single-particle potential strength*  $V$ . This parameter is very important in the present research, since the obtained theoretical results regarding energy spectra was obtained through the determination of  $V$  numerically.

Peng et al. [72] gave a description for nuclei within the mass region  $A \approx 100, 130$  using a Hamiltonian in which two valence nucleons were coupled to the triaxial core (due to the nuclear chirality arising from the odd-odd nature of nuclei). Their Hamiltonian was given as:

$$\hat{H} = \hat{H}_{\text{intr}} + \hat{H}_{\text{coll}} , \quad (4.9)$$

where  $\hat{H}_{\text{coll}}$  is the typical rotor Hamiltonian and  $\hat{H}_{\text{intr}}$  represents the sum of a proton and neutron contribution, respectively:

$$\hat{H}_{\text{intr}} = h_p + h_n . \quad (4.10)$$

A remarkable feature of this approach is that the problem can be extrapolated to a case with multiple protons and neutrons, invoking some sort of ‘scalability’

of their model. Furthermore, the deformed potential (Eq. 4.7) that gives the energy splittings for the nucleonic orbits (recall the Nilsson diagrams Figs. 3.11 - 3.12) is expressed in terms of the nucleus's mass and the quadrupole deformation parameter [72]:

$$V_{\text{int}}^{\text{quad}} = \frac{206}{A^{1/3}} \beta_2 \left[ \cos \gamma Y_2^0 + \frac{\sin \gamma}{\sqrt{2}} (Y_2^2 + Y_2^{-2}) \right] . \quad (4.11)$$

The single-particle energies for protons and neutrons have a somewhat similar form as the one stated in Eq. 4.8, namely it is given as:

$$h_p(n) = \pm \frac{1}{2} C_\beta \left[ \left( j_3^2 - \frac{j(j+1)}{3} \right) \cos \gamma + \frac{1}{2\sqrt{3}} (j_+^2 + j_-^2) \sin \gamma \right] , \quad (4.12)$$

with the alternating signs corresponding to the proton and neutron, respectively. The *coupling parameter*  $C_\beta$  is a measure of energy (typically expressed in MeV units) and its value depends linearly on  $\beta$ :

$$C_\beta = \frac{195}{j(j+1)} \beta A^{-1/3} . \quad (4.13)$$

It is worth giving some quantitative results concerning the quadrupole potential and the single-particle Hamiltonian described above. As such, a simple numerical application will be employed, giving graphical representations with the behavior of these quantities with respect to the deformation parameters. Firstly, the potential  $V_{\text{int}}^{\text{quad}}$  will be analyzed in the polar plane defined by the angles  $(\theta, \varphi)$  which enter in the expression of the spherical harmonics. For nuclei within  $A \approx 160$  region, it is common to have values of  $\beta_2 \approx 0.2, 0.3$  and  $\gamma \approx 20^\circ$ , so values for these parameters will be given within this range. The quadrupole potential  $V_{\text{int}}^{\text{quad}}$  can be seen in Figs. 4.1 - 4.2.

For the evaluation of  $h$ , one can take the case when only the diagonal components of  $h$  are considered and apply the rules only for one proton ( $p$ ). As a result, the *mixing terms*  $j_+$  and  $j_-$  from  $h$  won't contribute at all, since their action on protonic states  $|jk\rangle$  will give zero. Only the  $(j_3^2 - j(j+1)/3)$  term will contribute to the diagonal components of  $h$ . For a proton state  $|jk\rangle$ , where  $k = -j, \dots, j$ , the diagonal element  $\langle jk| h |jk\rangle$  will be:

$$h_{jk} \equiv \langle jk| h |jk\rangle = \frac{1}{2} C_\beta \cos \gamma \langle jk| \left( j_3^2 - \frac{j(j+1)}{3} \right) |jk\rangle , \quad (4.14)$$

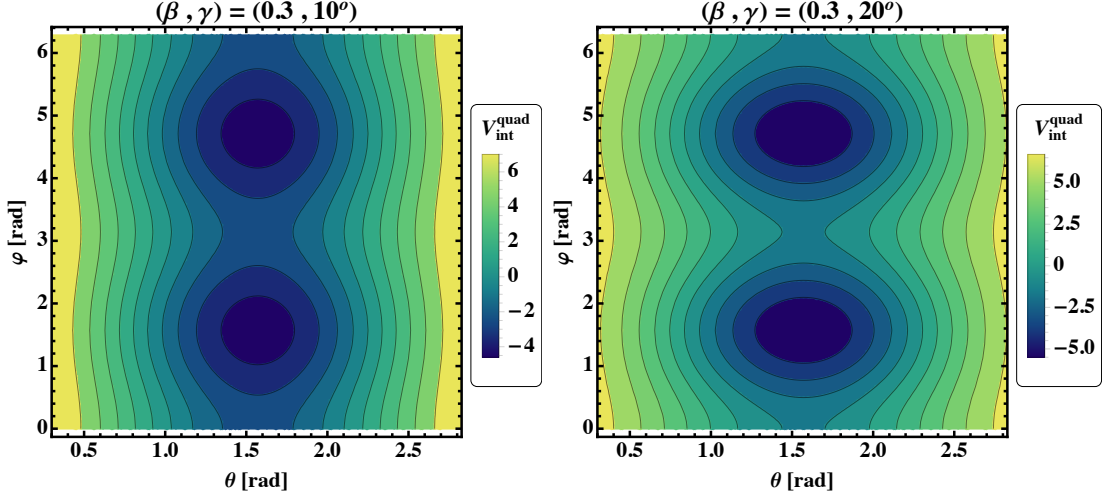


FIGURE 4.1: The quadrupole potential  $V_{\text{int}}^{\text{quad}}$  as defined in Eq. 4.11, represented as a function of the angular coordinates  $\theta$  and  $\varphi$ . Calculations were done with fixed parameters  $\beta_2$ ,  $\gamma$ , and for  $A = 163$ .

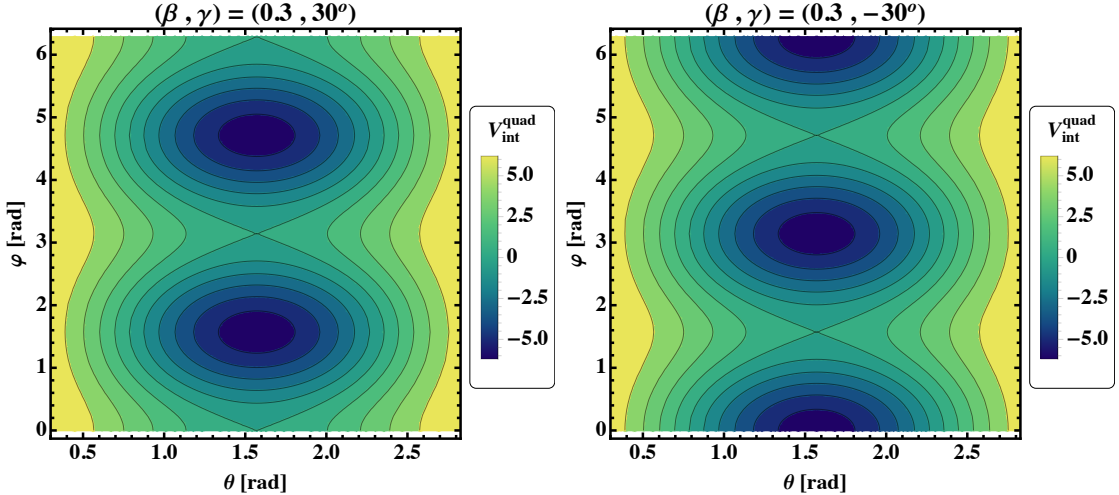


FIGURE 4.2: The quadrupole potential  $V_{\text{int}}^{\text{quad}}$  as defined in Eq. 4.11, represented as a function of the angular coordinates  $\theta$  and  $\varphi$ . Calculations were done with fixed parameters  $\beta_2$ ,  $\gamma$ , and for  $A = 163$ .

which can be simplified to:

$$h_{jk} = \frac{1}{2} C_\beta \cos \gamma \left( k^2 - \frac{j(j+1)}{3} \right) . \quad (4.15)$$

This matrix elements will be functions of deformation parameters as well as the projection  $k$  of the particle's angular momentum onto the 3-axis. Since  $j_3$  is applied twice on  $|jk\rangle$  state, the final result will be  $k^2$ , so only the positive values can be considered for the numerical application  $k = 1/2, \dots, j$ . When a high- $j$  proton orbital (say  $h_{11/2}$  or  $i_{13/2}$ ) is considered, for a nucleus with  $A = 167$ , the

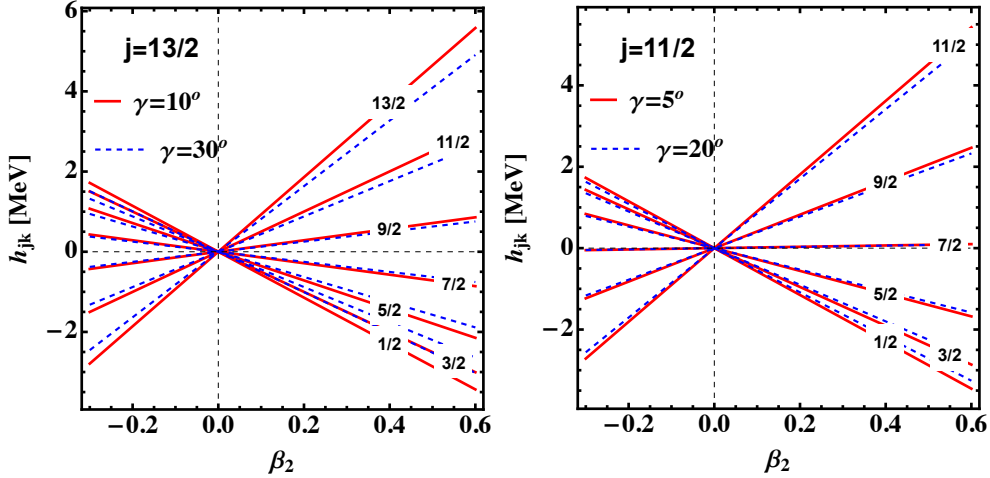


FIGURE 4.3: The evolution with quadrupole deformation parameter  $\beta_2$  for the diagonal matrix elements of  $h_{jk}$  defined in Eq. 4.15 (proton on a defined  $j$ -shell), at a fixed triaxiality parameter  $\gamma$ . See text for details.

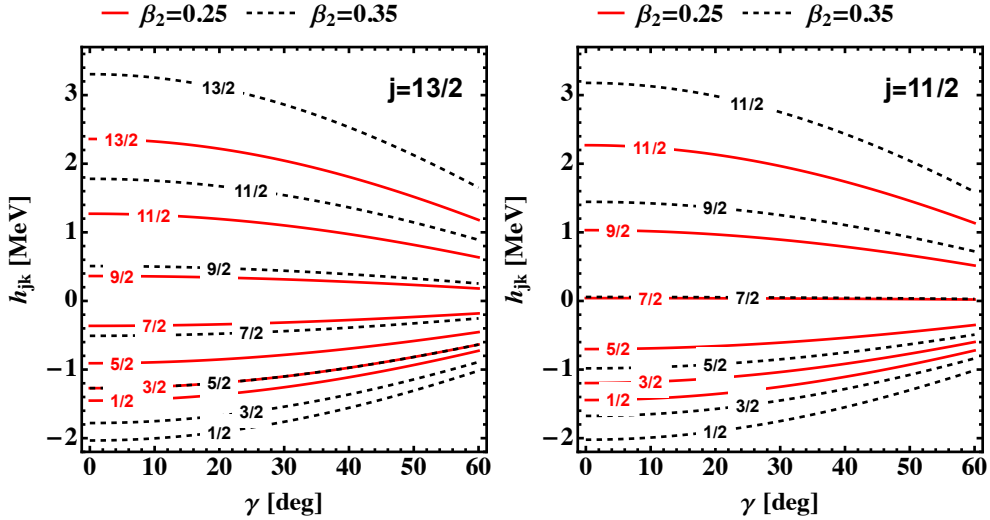


FIGURE 4.4: The evolution with triaxiality parameter  $\gamma$  for the diagonal matrix elements of  $h_{jk}$  defined in Eq. 4.15 (proton on a defined  $j$ -shell), at a fixed deformation parameter  $\beta_2$ . See text for details.

evolution of  $h_{jk}$  as function of  $\beta_2$  and  $\gamma$ , respectively, are shown in Figs. 4.3. For completeness, the evolution w.r.t. the triaxiality parameter  $\gamma$  for the diagonal matrix elements of  $h$  are shown Fig. 4.4.

Regarding this numerical application, one can observe the fact that since only the cosine function is present in the diagonal components of  $h$ , the single-particle energies are independent on the sign of  $\gamma$  (since cosine is an even function). However, this is not the case when calculations are done for the non-diagonal elements, since states with different  $k$  will add contributions to  $h$  via the sine function. For the evolution of  $h_{jk}$  with  $\beta_2$ , one can see that the lines in Fig. 4.3 (especially the

right plot) are almost similar, indicating that the diagonal components are not very sensitive to nuclear triaxiality. On the other hand, a difference in  $\beta_2$  between the components will result in large gaps.

Going back to the general Hamiltonian given in Eq. 4.6 and putting together Eqs. 4.7, 4.8, 4.11, it can be brought to a ‘final’ form. With this, rotor and the single-particle contributions are clearly depicted while the influence of the quadrupole deformation and triaxiality also explicitly employed [4]:

$$\hat{H} = \sum_i \frac{R_i^2}{2\mathcal{I}_i} + h_0^j + \frac{V}{j(j+1)} \left[ \cos \gamma (3j_z^2 - \mathbf{j}^2) - \sqrt{3} \sin \gamma (j_x^2 - j_y^2) \right]. \quad (4.16)$$

Regarding the dynamical character of  $\hat{H}$  defined in Eq. 4.16, the coupling of high- $j$  particle with a rotor will create physical effects which can be classified in the following way [4]:

- rotational energy is always minimized by the rotation of the core around the axis with the largest MOI
- alignment of the odd particle will always prefer a maximal mass overlap with the core (this configuration minimizes the potential energy the most)
- the Coriolis effect will always tend to align the particle with the core, in terms of their a.m.

Concluding this section, by using the triaxial PRM one can describe the energies of a an odd- $A$  triaxial nucleus, and moreover, as it will be shown, quantities such as transition probabilities (electric quadrupole type) and quadrupole moments can be calculated. It is a starting ground for multiple theoretical descriptions which aim to verify, confirm, and even predict phenomena specific to highly deformed shapes.

## 4.2 Stable Triaxial Deformation

As it was mentioned, across the chart of nuclides, stable isotopes do exist in an *equilibrium* at which no symmetries are involved with regards to their shape. Quantitatively, the stability of a triaxial nucleus is related to the presence (existence)

of minima within the *Potential Energy Surface*. This energy surface characterizes the shape of the nuclear surface with respect to the deformation parameters  $\beta$  and  $\gamma$ . One can speculate on the fact that for an ellipsoidal shape, the total energy at a fixed angular momentum, function of the deformation will be given as [4]:

$$E(\beta, \gamma, I) = E_{\text{LDM}}(\beta, \gamma, I) + E_{\text{shell}}(\beta, \gamma, I) - \bar{E}_{\text{corr}}(\beta, \gamma, I), \quad (4.17)$$

where  $E_{\text{LDM}}$  is the deformation energy for a rotating ellipsoid (characterized by the rigid-like MOI, since at high spin values this approximation holds true),  $E_{\text{shell}}$  is the energy within the shell model (can even use the Nilsson's deformed variant), and  $\bar{E}_{\text{corr}}$  is usually calculated as an *averaged value* of the Nilsson-Strutinsky corrected potential [73] (which is beyond the scope of this work). Finding these energies can be done by working at constant  $\omega$  or at constant  $I$ , when diagonalizing the deformed-single particle potential in the rotating frame [4].

Solving thus Eq. 4.17 results in having a *qualitative* analysis for the behavior of the nucleonic matter at high spins. These ‘solutions’ will consist of graphical representations in the  $(\beta, \gamma)$ -plane, where values with different magnitudes for the potential energy appear. The lower these values are, the ‘more stable’ the deformation is. Typically, one can find regions of stability across the plane with well-defined values for  $\beta$  and  $\gamma$  at which nucleus is stable and deformed. On the other hand, if the energy variation is rather flat in the  $\gamma$  degree of freedom, but centered around a finite  $\beta$ , then this nucleus is called  $\gamma$ -*unstable*. These energy surfaces are a key indicator of stability with respect to the deformation parameters. Examples of energy surfaces for some nuclei are shown in Figs. 4.5 - 4.6. It is remarkable the fact that small quantum fluctuations will exist around the minima. In order to explain the theoretical implications of Figs. 4.5 - 4.6, one needs to understand that based on a MHO, a so-called *Ultimate Cranker* (UC) numerical implementation has been developed [74, 75] (a Nilsson deformed potential in which pairing interaction is taken into account). This implementation is able to give the values for  $(\beta, \gamma)$  at which a nucleus might achieve stability, practically identifying local and global minima within the potential energy surface. In a future section, multiple isotopes with known stable triaxiality will be classified in terms of the deformation parameters, creating thus an ‘inventory’ with these deformed nuclei.

Similarly, PES calculations for other nuclei will also point out the stable deformations (with triaxial character), extracting the deformation parameters. For instance, within the  $A \approx 160$  mass region there are multiple nuclei in which TSD

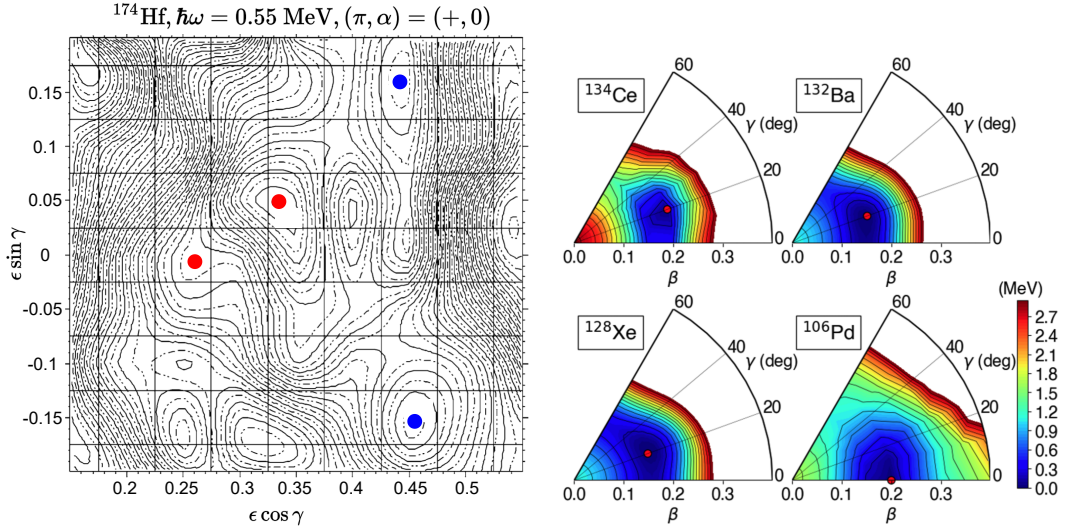


FIGURE 4.5: **Left:** Potential energy surface for  $^{174}\text{Hf}$ , evaluated at a constant rotational frequency. Positive parity and a signature  $\alpha = 0$  were considered. Four minima that could be attributed to known configurations are identified which are marked with red colored dots (normal deformation) and blue dots (strong deformation). This figure was taken from Ref. [76]. **Right:** PES for some even-even nuclei. Note the rather shallow triaxial minima for all nuclei, and the  $\gamma$ -soft nature of all the nuclei except for  $^{106}\text{Pd}$ , whose minimum is achieved at a null triaxiality parameter. This figure was taken from Ref. [77].

bands are identified. Best example are the results concerning Lu-Hf isotopes, where more than 20 such bands were experimentally confirmed [79]. It is interesting that fact that the nuclei with even  $N$  (especially the Lu isotopes) have ground state TSD bands which emerge from a configuration based on the  $\pi = i_{13/2}$  nucleon. In fact, Ødegård et al. [69] point out the fact that nuclei with proton number  $Z \approx 71$  and neutron number  $N \approx 94$  have stable triaxial shapes with large quadrupole deformation around the values  $(\beta_2, \gamma) = (0.38, \pm 20^\circ)$ , while the lowest energy state corresponding to the odd nucleon is the  $i_{13/2}$  proton [80].

Given the degree of shell filling, only some specific triaxial shapes with fixed value of  $\gamma$  are favored by the aligned particle (see Ref. [81] for more details). In the case of  $^{163}\text{Lu}$ , the aligned proton from  $j = 13/2$  shell favors a triaxiality of  $\gamma = 20^\circ$  (see Fig. 4.6). Similarly, other nuclei will have different high- $j$  nucleon configurations which will drive the system to large triaxial deformations, by favoring a particular value of  $\gamma$ .

Now that the stability of asymmetric nuclear shapes has been visualized in terms of energy surfaces and deformation parameters (whose magnitudes are more or less

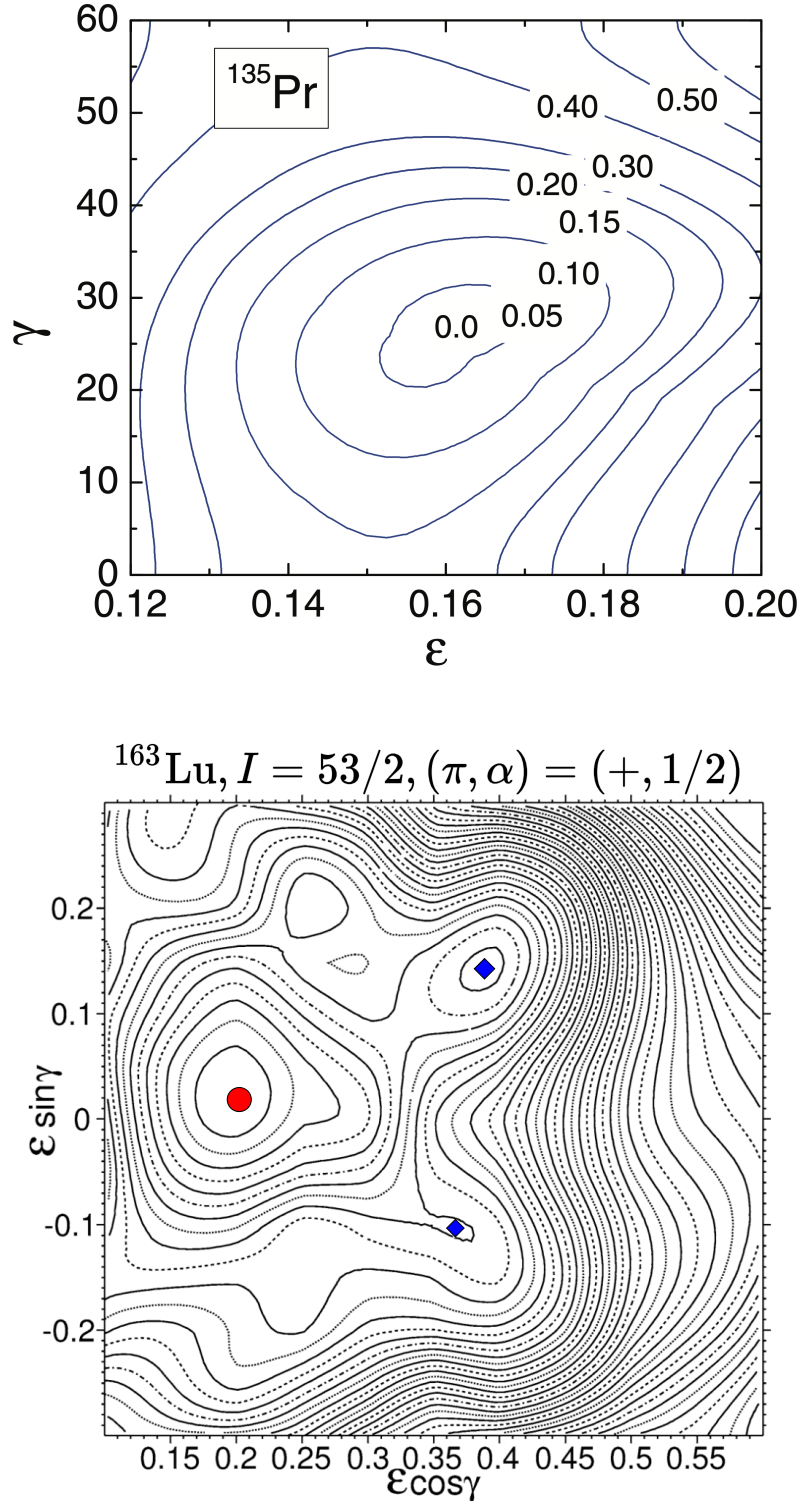


FIGURE 4.6: **Top:** PES for the odd- $A$  nucleus  $^{135}\text{Pr}$ , with units of MeV. The figure is taken from the work of Frauendorf et al. [23]. **Bottom:** PES for the odd- $A$  isotope  $^{163}\text{Lu}$  evaluated at a fixed spin  $I = 53/2$  with positive parity and positive signature. The red dot corresponds to a global minimum for normal deformed structure, while the blue diamonds represent two additional minima which correspond to strong deformation. This plot is taken from Ref. [78].

given by the favoring of the single-particle configuration), it is instructive to understand how one can identify triaxial nuclei (both experimentally and theoretically). This will be done in the following section.

### 4.3 Fingerprints of Triaxiality

Within recent years, it has been shown that triaxiality plays an important role on features such as:

- Calculating nucleon separation energies [67]
- Protonic emission probabilities [82, 83]
- Determination of fission barrier height [84, 85]
- Nuclear fragmentation [86]

Unfortunately, triaxiality is still quite challenging to measure it directly [25, 66]. On the experimental side, a tremendous effort was made in order to construct setups that can study nuclei at very high spins (were collective phenomena previously discussed appear). Over the last 25 years, with the advance in technology of detectors [87], some large facilities were built, with the sole purpose of studying high-spin nuclei with great degree of precision on the spectroscopic measurements that are performed. Facilities such as the EUROBALL [88] or GAMMAS-PHERE [89] opened *new frontiers* on the nuclear physics at high-spin; being able to measure excited spectra of nuclei having angular momentum within the range  $60 - 80\hbar$ . Regarding the reactions involved, most of the measurements of highly excited (and rapidly rotating) are obtained through *Fusion-Evaporation Reactions* in which heavy-ion collisions take place. Since this work does not focus on the experimental setups and procedures, only some literature covering these reactions are mentioned: [8, 10, 24, 79, 87, 90, 91].

Even though stable triaxiality is an elusive phenomenon, *two clear fingerprints* are known to pinpoint asymmetric nuclear shapes: **wobbling motion** and **chiral symmetry breaking**. There has been an extensive study of these two phenomena, and both indicate a clear correspondence between their physical significance and the lack of symmetry for the underlying nuclei. Since wobbling is the main

focus of this work, a brief introduction for chiral symmetry breaking will be made below, while a separated chapter will be devoted to the theoretical and experimental evidence regarding wobbling motion. Moreover, all the theoretical results obtained within the team’s framework will be presented.

### 4.3.1 Chiral motion

Firstly introduced by Frauendorf [45], it concerns nuclei in which the nucleonic configurations lead to a system that lacks *chiral symmetry*, meaning that the left-handed system is not identical with its right-handed system. The left/right handedness of the nuclear system comes from the coupling of three different angular momenta, typically that is a valence proton, a valence neutron, and a rotational core (of collective nature). As such, the chiral symmetry breaking is expected to appear in odd-odd nuclei.

In this pioneering work, it was shown that for a triaxial nucleus, the collective angular momentum  $\mathbf{R}$  will align along the intermediate ( $i$ ) axis of the deformed ellipsoid (note that the  $i$ -axis is also the axis with largest MOI). Regarding the particles, the location of their corresponding Fermi level will dictate the alignment of the nucleons with the ellipsoid [45, 92]. For a valence proton with the energy located in the bottom part of the high- $j$  subshell, it will align its a.m. with the short  $s$ -axis of the ellipsoid. Furthermore, a valence neutron having located in the upper part of the high- $j$  shell will align its a.m. with the long  $l$ -axis. Reasoning for these kind of orientations have been discussed already: they are related to the overlap between the single-particle wave-functions and that of the triaxial nuclear shape. *Maximal overlap will always minimize the interaction energy.* The three alignments will result in a perpendicular set of a.m., so they can be arranged in configurations with different chirality: left- and right-handed systems. The chiral operator combines a rotation with the time-reversal operator:  $\chi_{\text{chiral}} = \mathcal{T}R_y(\pi)$ .

When the chiral symmetry is broken in the intrinsic frame of reference (body-fixed frame), the ‘restoration’ of the symmetry in the laboratory frame will manifest itself as the emergence of two almost degenerate doublet bands with  $\Delta I = 1\hbar$  [45]. Also, in the laboratory frame of reference, this pair of bands will appear since the symmetry (broken in the body-fixed frame) will be restored via the quantum tunneling effect [93]. This interesting behavior has been drawing a lot of attention lately, with most of the experimental identifications around the transitional nuclei

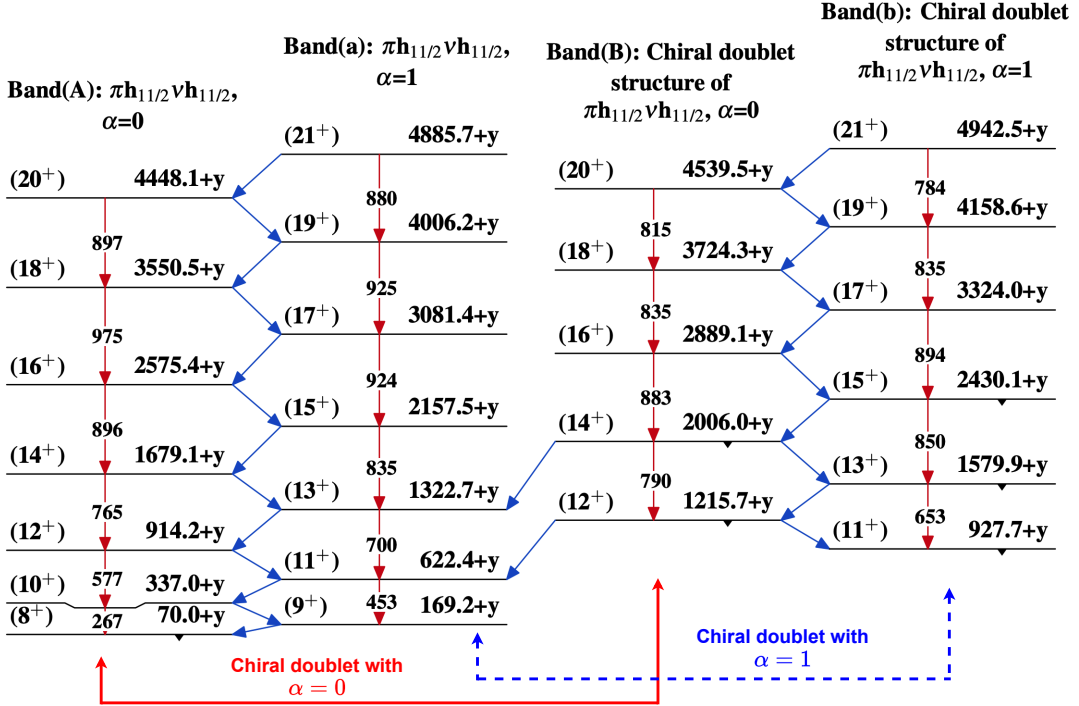


FIGURE 4.7: The energy spectra for the odd-odd  $^{136}\text{Pm}$  isotope, in which the chiral doublet built on the configuration  $\pi h_{11/2} \otimes \nu h_{11/2}$  appears. Experimental data is from Ref. [97] and the level scheme is adapted from Ref. [48].

$A \approx 130$ . Great research towards complete spectroscopy of some chiral nuclei has been done in Refs. [66, 92, 94–96]. Examples of experimental chiral doublets are shown in Figs. 4.7 - 4.8 for some odd-odd nuclei.

The geometrical interpretation of the left-handed and right-handed systems can be seen in Fig. 4.9, where the ellipsoid is ‘surrounded’ by the two valence nucleons, each with its aligned a.m. w.r.t. principal axes.

## 4.4 Wobbling Motion

The second fingerprint of triaxiality is the ‘core’ topic of this work, and it will be discussed in detail in the next chapter, where some theoretical ideas will be presented together with the latest experimental results. A great amount of progress towards understanding nuclear phenomena at high spin has been made by the scientific community which devoted research to this particular topic.

Going back to the discussion about the triaxial shapes and their asymmetry between the MOI, this key feature leads to the possibility of defining a rotation about

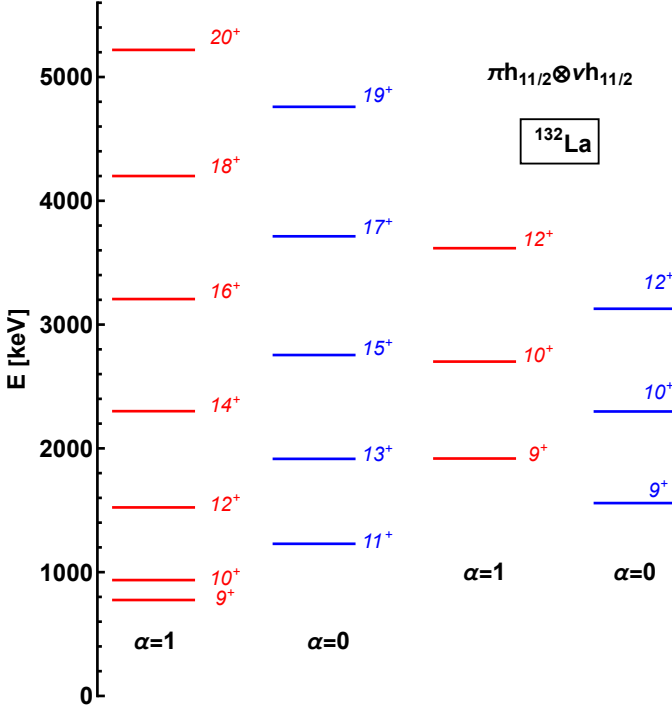


FIGURE 4.8: The energy spectra for the odd-odd  $^{132}\text{La}$  isotope, in which the chiral doublet built on the configuration  $\pi h_{11/2} \otimes \nu h_{11/2}$  appears, with each double being properly colored in red and blue, respectively. Experimental data is taken from Ref. [98, 99].

any of the three axis. Although the main rotational motion will be around the axis with the largest MOI (since this is energetically the cheapest [5]), the other two axes will contribute to a ‘total’ (superimposed) rotation such that the angular momentum  $\mathbf{I}$  of the system will precess around a steady position. The precessional motion has oscillator-like behavior, meaning that  $\mathbf{I}$  will not only precess, but its projection around the principal axes will oscillate around a steady position. The easiest way of understanding wobbling motion is a classical analog such as the *spinning asymmetric top*, but for a nucleus the spinning motion is *quantized* and a typical phonon number will be attributed to the system.

As it will be shown in the following chapter, treating the wobbling phenomenon in a ‘classical’ will lead to very good results concerning the physical quantities of interest. Moreover, there are many attempts (albeit quantum mechanical or semi-classical approximations) at describing wobbling motion in which the parameters used to describe the Hamiltonian have clear analogies with quantities that describe classical systems, keeping thus a close contact with well-defined concepts regarding system dynamics.

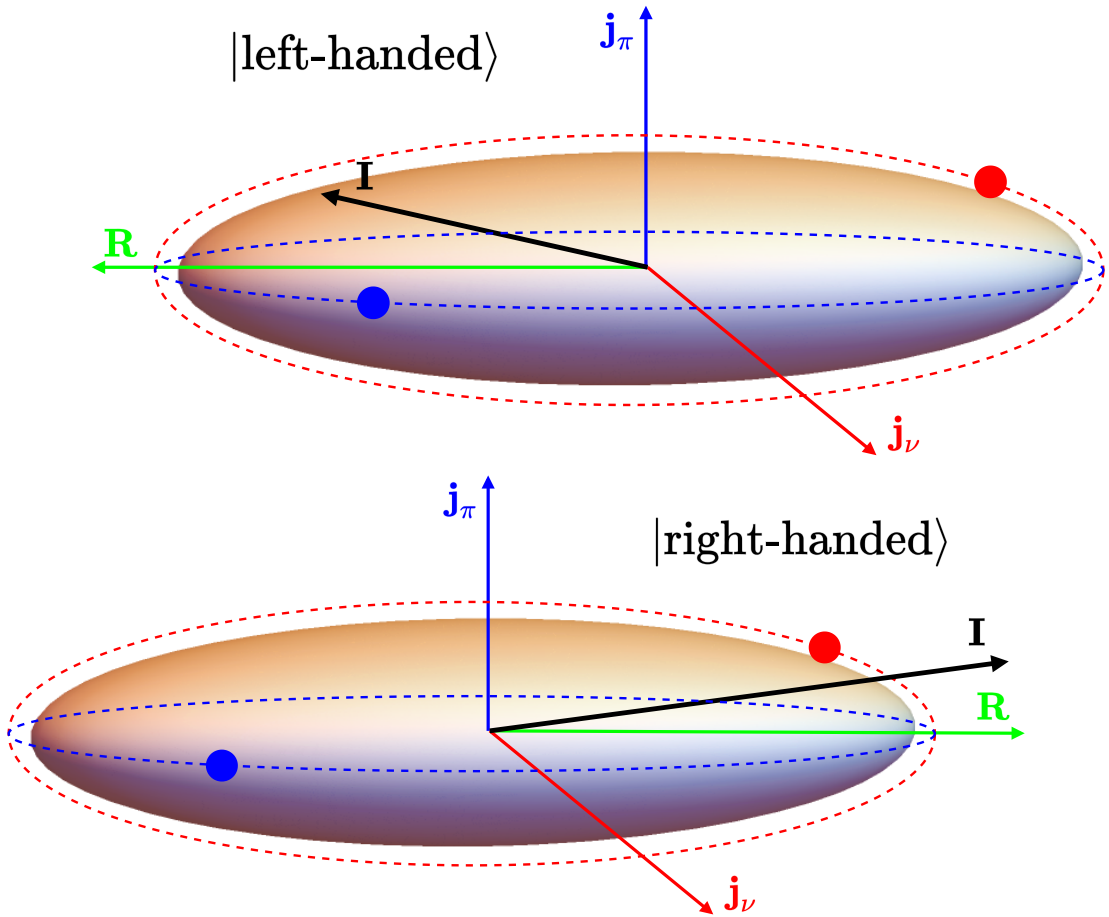


FIGURE 4.9: Left- and right-handed chiral systems (top and bottom insets, respectively) for a triaxial odd-odd nucleus, indicating the mutually perpendicular angular momentum vectors. The two valence nucleons with their orbits are colored with red (proton) and blue (neutron). These figures were inspired by an original design from [92]. Considering the discussion regarding alignments, the proton a.m. is aligned with the  $s$ -axis, the neutron with the  $l$ -axis, and the core with the  $i$ -axis of the ellipsoid.

Other classical analogies for the nuclear wobbling motion can be seen in celestial bodies such as planets. Indeed, Earth has a precession given by its rotation and a small amplitude polar motion. As a result, the Earth's 'angular momentum' will oscillate with respect to one of the body's fixed axis.

# Chapter 5

## Wobbling Motion in Nuclei

The pioneering work of Bohr and Mottelson [1] which was done more than 50 years ago lead to some interesting features regarding the collective phenomena in triaxial nuclei. Namely, they pointed out that a specific precessional motion of the nucleus's spin will take place when the rotational energy is sufficient. The angular momentum for triaxial nuclei is not aligned any of the principal axes of the ellipsoid, but it *precesses* and *wobbles* around one of these axes. They called this phenomenon **wobbling motion** (w.m.). This combined motion comes from a consequence regarding the MOI. Indeed, the asymmetry of the three MOI makes the quantum mechanical nature of rotation to be possible around any of the three axes. As such, a *main* rotation around the axis with the largest MOI will be the most energetically favorable, but the other two directions can *quantum mechanically disturb* this main rotation, leading to this unique characteristic of triaxial nuclei.

The non-uniformity nature of w.m. was firstly studied for the ‘pure’ rigid-rotators that correspond to the even-even nuclei. In this case, the w.m. can be treated as small amplitude oscillations of the total angular momentum  $\mathbf{I}$  around the axis corresponding to the largest MOI.

### 5.1 Wobbling Motion in Even-Even Nuclei

The analytical expressions for wobbling excitations were firstly evaluated by Bohr and Mottelson using the so-called *Harmonic Approximation* (HA). This can be

described as a small-amplitude limit for the Triaxial Rigid Rotor Hamiltonian that was discussed in Chapter 4 (see Section 4.1.1). In this limit, the projection of the total angular momentum onto the axis with largest MOI can be approximated  $I_3 \approx I$ , meaning that the nucleus will do most of its rotation around this axis, with some ‘disturbance’ from the other two principal of the triaxial rotor.

For the description of this simple wobbler, one can consider the case when the 3-axis has the largest MOI, and the following order holds true:

$$\mathcal{I}_3 > \mathcal{I}_2 > \mathcal{I}_1 , \quad (5.1)$$

or equivalently:

$$A_3 < A_2 < A_1 . \quad (5.2)$$

The Hamiltonian can be written as:

$$\hat{H}_{\text{rot}} = A_3 I_3^2 + (A_1 I_1^2 + A_2 I_2^2) \quad (5.3)$$

The different colors from Eq. 5.3 try to emphasize the fact that a Hamiltonian for the simple wobbler can be regarded as *a main rotation around 3-axis* (represented by red color) and *the (precession + oscillation) of the total angular momentum* (represented by blue color).

The wobbling excitations which cause oscillations with small amplitudes for  $\mathbf{I}$  about the 3-axis are assumed to have a harmonic-like behavior, meaning that the final energy spectrum of a simple wobbler (even-even nucleus) will have the typical  $\hbar\omega(n + 1/2)$  behavior. Since this oscillator motion can be explained as ‘vibrations’ of the total angular momentum around a steady position, where each wobbling excitation consists of an additional vibrating phonon, one can express the Hamiltonian in terms of *boson* creation and annihilation operators. As such, the quantum mechanical treatment implies [1]:

$$b^\dagger = \frac{1}{\sqrt{2I}} I_+ , \quad b = \frac{1}{\sqrt{2I}} I_- , \quad [b, b^\dagger] \approx 1 . \quad (5.4)$$

This initial quantization allows one to write Eq. 5.3 as a rotational term and a wobbling-specific one:

$$\hat{H}_{\text{rot}} = \textcolor{red}{A}_3 \textcolor{red}{I}_3^2 + \textcolor{blue}{H}_w , \quad (5.5)$$

$$\textcolor{blue}{H}_w = \textcolor{blue}{t}_1 \left( n + \frac{1}{2} \right) + \frac{1}{2} \textcolor{blue}{t}_2 (\textcolor{blue}{b}^\dagger \textcolor{blue}{b}^\dagger + \textcolor{blue}{b} \textcolor{blue}{b}) , \quad (5.6)$$

where the *number of boson excitations* is denoted by  $n$  and it is given by  $n = \textcolor{blue}{b}^\dagger \textcolor{blue}{b}$ . Each wobbling quanta will carry an angular momentum of one unit less with respect to the 3-axis. The two factors  $t_{1,2}$  are expressed in terms of the inertial parameters as [1]:

$$t_1 = I(A_2 + A_1 - 2A_3) , \quad (5.7)$$

$$t_2 = I(A_2 - A_1) . \quad (5.8)$$

Notice the linear dependence of the two parameters on the total angular momentum  $I$ . Moreover, depending on the values of  $A_k$ , the contribution of  $t_{1,2}$  can be negative. Their behavior is shown within the right inset of Fig. 5.2. Although the Hamiltonian  $H_w$  is considered to have an oscillator-like behavior, its general expression does not look like a typical harmonic Hamiltonian. For this, the Hamiltonian given in Eq. 5.6 can be brought to a diagonalized form by introducing a new set of boson creation and annihilation operators. These operators will be written as linear combinations of  $(\textcolor{blue}{b}^\dagger, \textcolor{blue}{b})$ :

$$c^\dagger = w_1 b^\dagger - w_2 b , \quad (5.9)$$

$$c = w_1 b - w_2 b^\dagger , \quad (5.10)$$

where the two coefficients  $w_{1,2}$  are defined in terms of  $t_{1,2}$  as:

$$w_1 = \left[ \frac{1}{2} \left( \frac{t_1}{\sqrt{t_1^2 - t_2^2}} + 1 \right) \right]^{1/2} ,$$

$$w_2 = \left[ \frac{1}{2} \left( \frac{t_1}{\sqrt{t_1^2 - t_2^2}} - 1 \right) \right]^{1/2} . \quad (5.11)$$

The terms  $w_{1,2}$  verify the condition  $w_1^2 - w_2^2 = 1$  and they make the ‘dangerous’ products  $(\textcolor{blue}{b}^\dagger \textcolor{blue}{b}^\dagger, \textcolor{blue}{b} \textcolor{blue}{b})$  disappear in this new representation [100]. Note that there is no spin dependence inferred in Eq. 5.11 such that  $w_{1,2}$  are constant functions of

spin, unlike the coefficients  $t_{1,2}$ . Moreover, introducing a number operator  $\hat{n} = c^\dagger c$  and the excitation quanta  $\hbar\omega_w$  defined as:

$$\hbar\omega_w = \sqrt{t_1^2 - t_2^2} = 2I\sqrt{(A_1 - A_3)(A_2 - A_3)} , \quad (5.12)$$

then a final expression of  $H_w$  can be expressed, which has a behavior typical to the *harmonic oscillator*:

$$H_w = \hbar\omega_w \left( \hat{n} + \frac{1}{2} \right) . \quad (5.13)$$

In this expression, the excitation quanta  $\hbar\omega_w$  which was defined in Eq. 5.12 in terms of  $t_{1,2}$  is called *wobbling frequency* and its increasing linearly with the total angular momentum. Accordingly, Eq. 5.5 can be re-written with the wobbling Hamiltonian defined in Eq. 5.13:

$$\hat{H}_{\text{rot}} = A_3 I(I+1) + \hbar\omega_w \left( \hat{n} + \frac{1}{2} \right) . \quad (5.14)$$

Thus, in the HA, the eigenvalues of the rotor Hamiltonian can be expressed in terms of a *wobbling phonon number*  $n_w$  (which is the eigenvalue of the number operator  $\hat{n} = c^\dagger c$ ) and a *wobbling frequency* (defined in Eq. 5.12):

$$E_{I,n} = A_3 I(I+1) + \hbar\omega_w \left( n_w + \frac{1}{2} \right) . \quad (5.15)$$

The spectrum for an even-even wobbling nucleus is thus represented by Eq. 5.15. Notice again the two colored terms that illustrate the energy coming from the rotation around the 3-axis and the disturbed motion with small oscillations around the other two axes. Consequently, the wobbling character of the system will be generated by the latter harmonic term. The wobbling phonon number  $n_w$  is related to the ‘strength’ of the tilting for  $\mathbf{I}$ , indicating the fact that an increasing number for  $n_w$  will result in oscillations with larger amplitudes around the other two axes. The phonon number takes values  $n_w = 0, 1, \dots$ . In inset b) from Fig. 5.1, a sketch which shows the tilting effect that the wobbling phonon number has on the total angular momentum vector is drawn. For completeness, the collective structure of two wobbling bands generated through phonon excitations is exemplified in inset a) from Fig. 5.1.

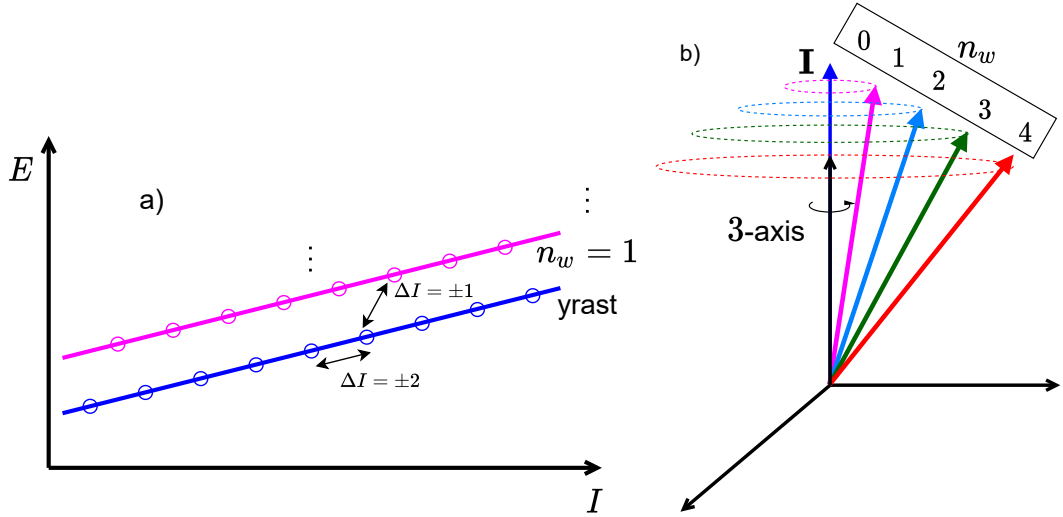


FIGURE 5.1: **Left:** A typical wobbling structure for even-even nuclei. The yrast band contains even values of spins since the band has signature  $\alpha = 0$ , while the first excited band has odd spins and  $\alpha = 1$ . The intraband states differ by 2 units of angular momenta, while the interband ones differ with only one unit. **Right:** The increase of tilting angle between the rotational axis (the 3-axis in this case) and the total angular momentum  $\mathbf{I}$ . With each wobbling phonon number, the total angular momentum tilts more and more, generating a ‘stronger’ precessional motion (illustrated by the colored ellipses).

An alternative way of depicting the wobbling term  $H_w$  from Eq. 5.5 would be to express it more generally, in terms of  $I_2$  and  $I_3$ . When doing so, one achieves the following form (assuming that rotation is around the 3-axis) [100]:

$$H_w = (A_1 - A_3)I_1^2 + (A_2 - A_3)I_2^2 = T_{\text{kin}} + T_{\text{pot}}, \quad (5.16)$$

where according to Ref. [71], one can regard these two factors as a *kinetic* and a *potential* term. This way of expressing  $H_w$  is instructive since it keeps a close contact with the ‘classical’ picture of understanding the total energy of a system.

As a quantitative analysis of the wobbling frequency and the rotor energy, one can take three arbitrary values for the moments of inertia (and, implicitly, the inertia factors  $A_k$ ) and see the behavior of both  $E_{I,n}$  and  $\hbar\omega_w$  with increasing angular momentum and wobbling phonon number. Keep in mind that depending on the value of the wobbling phonon number, different spin sequences will be allowed. More precisely, from the invariance of the rotor w.r.t. rotations by  $\pi$  about the principal axes for even-even nuclei, the signature quantum number  $\alpha$  can take the values 0 and 1. Each wobbling band will have an alternating signature, starting with  $\alpha = 0$  for  $n_w = 0$  then  $\alpha = 1$  for  $n_w = 1$  and so on: even spin sequences

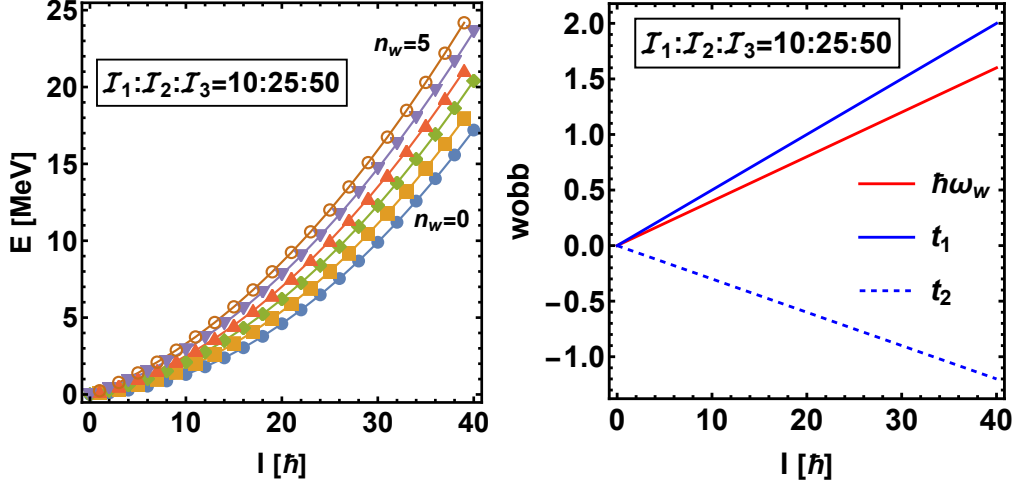


FIGURE 5.2: **Left:** The energy spectrum for an even-even nucleus with three different moments of inertia, with the main rotation around the 3-axis, according to Eq. 5.15. Each wobbling band has alternating signature number  $\alpha$  (starting with  $\alpha = 0$  for the ground state  $n_w = 0$  band). Notice the even/odd spin sequences for each band. **Right::** The wobbling frequency plotted together with the linear terms  $t_1$  and  $t_2$  that are used to express  $\hbar\omega_w$ . Same set of MOI were used across both figures and the unit for  $\mathcal{I}_i$  is  $\hbar^2 \text{ MeV}^{-1}$ .

appear for even values of  $n_w$  and odd spin sequences appear for odd values of  $n_w$  (see Fig. 5.2).

The rotor energy from Eq. 5.15 is graphically represented for an arbitrary set of moments of inertia as a function of the nuclear angular momentum  $I$  in Fig. 5.2. This pedagogical example contains rotational bands up to  $n_w = 5$  in the wobbling phonon number. From Fig. 5.2, one can see the linear dependence on the total angular momentum and, moreover, the wobbling energy and frequency both are increasing with spin.

Another instructive analysis would be the evolution of the components of  $\mathbf{I}$  as functions of the polar and azimuthal angles  $\theta, \varphi$ . Indeed, expressing the three angular momentum components as:

$$I_1 = I' \sin \theta \cos \varphi , \quad (5.17)$$

$$I_2 = I' \sin \theta \sin \varphi , \quad (5.18)$$

$$I_3 = I' \cos \theta , \quad (5.19)$$

where  $I' = \sqrt{I(I+1)}$ , one can make a graphical representation for them, by letting  $\theta$  and  $\varphi$  vary within their corresponding intervals. In Fig. 5.3, the quantities

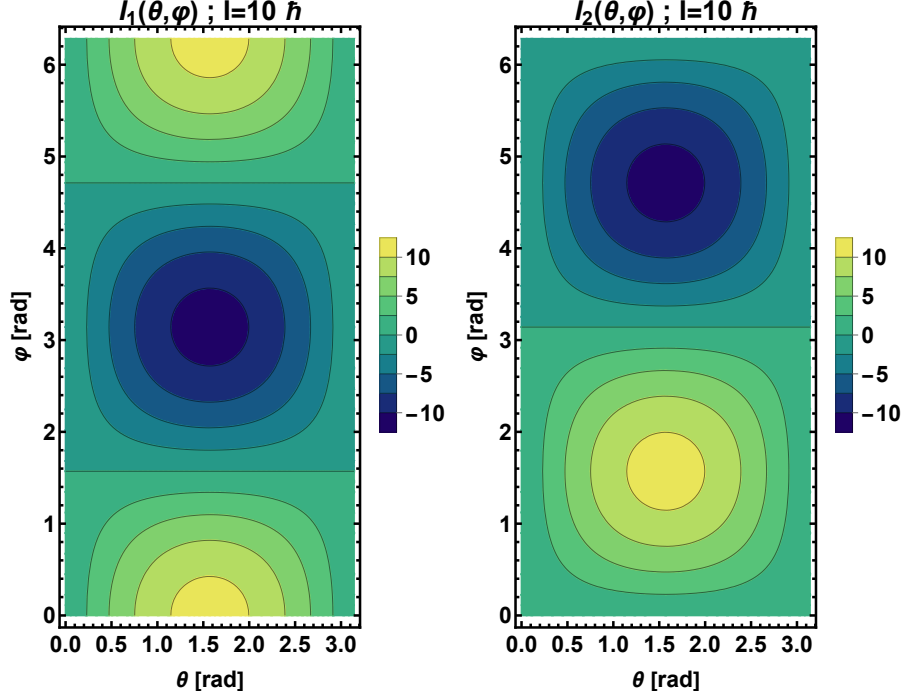


FIGURE 5.3: The geometrical representation of the first and second component of the total angular momentum  $\mathbf{I}$  as functions of the polar angles, according to Eq. 5.19.

$I_1$  and  $I_2$  are represented in the  $(\theta, \varphi)$  plane for a fixed spin value  $I = 10\hbar$ . Since the third component is independent of the azimuthal angle  $\varphi$ , it has been dismissed.

The other relevant observables which can be calculated for simple wobbler within the HA are the two quadrupole moments  $Q_{20,22}$  and the intraband + interband  $B(E2)$  transition probabilities. The quadrupole components are expressed in terms of the intrinsic quadrupole moment  $Q_0$  and the triaxiality parameter as [101]:

$$Q_{20} = Q_0 \cos \gamma, \quad Q_{22} = \frac{1}{\sqrt{2}} Q_0 \sin \gamma. \quad (5.20)$$

These components can be furthermore used to determine the intraband  $B(E2)$  transition probabilities [71]:

$$B(E2; (n, I) \rightarrow (n, I-2)) = \frac{5}{16\pi} Q_{22}^2, \quad (5.21)$$

and also the interband transitions:

$$B(E2; (n, I) \rightarrow (n - 1, I - 1)) = \frac{5}{16\pi} \frac{n}{I} \left( \sqrt{3}Q_{20}w_1 + \sqrt{2}Q_{22}w_2 \right)^2 , \quad (5.22)$$

$$B(E2; (n, I) \rightarrow (n + 1, I - 1)) = \frac{5}{16\pi} \frac{n+1}{I} \left( \sqrt{3}Q_{20}w_2 + \sqrt{2}Q_{22}w_1 \right)^2 . \quad (5.23)$$

Notice that for the intraband transitions, going from the state  $I$  to  $I - 2$  will only depend quadratically on the quadrupole component  $Q_{22}$ , making thus the transitions spin-independent.

### Triaxial rotor energy vs. wobbling energy

An important discussion should be made regarding the nomenclature for energies when referring to wobbling motion. As shown in Eq. 5.15, the energy spectrum for a simple wobbler can be determined for every phonon number and spin sequences. However, that is the ‘full’ spectrum of the wobbler, which is composed of the *yrast* states with  $n_w = 0$  and the *excited states* having  $n_w = 1, \dots$  and so on. On the other hand, the so-called *wobbling energies* are defined in terms of these ‘absolute values’ (i.e.,  $E_{I,n}$ ) with the following rules [71]:

$$E_{\text{wob}}(I_{\text{even}}) = E_{I,n} - E_{I,0} , \quad (5.24)$$

$$E_{\text{wob}}(I_{\text{odd}}) = E_{I,n} - \frac{1}{2} (E_{I-1,0} + E_{I+1,0}) , \quad (5.25)$$

where the former wobbling energy corresponds to the even values of  $I$  and the latter is applied for odd values of  $I$ . Very often within literature the energies calculated via Eq. 5.15 are referred to also as wobbling energies, which is not the same as Eq. 5.25, so a distinction should be made clear.

#### 5.1.1 Testing the Harmonic Approximation

It is worth going further and apply the HA formalism for even-even nuclei for an existing spectrum. As such, one can take  $^{130}\text{Ba}$  as a testing example. As it will be discussed in a follow-up section, it turns out that experimental observations for wobbling structures in even-mass isotopes have been very scarce. Nevertheless, very recently Petrache et al. identified a large collection of band structures in  $^{130}\text{Ba}$  [102]. Two of them are reported to be of wobbling nature [103]. Having

these two collective bands, one can check if the energy formula given in Eq. 5.15 for the simple wobbler can be applied for this isotope.

The method described in here will be based on a *fitting procedure*, namely a set of parameters will be extracted from the expression of  $E_{I,n}$  and they will be adjusted such that the experimental data is best reproduced by the theoretical model. This kind of approach works really well for ‘well-behaved’ model functions and if the input data is large enough to reach a good fit precision. More often than not, if the model function contains parameters which have a clear physical meaning then fitting becomes a suitable approach. In fact, in the following chapters, the developed formalism will verify the experimental data through similar fitting procedures (although their ‘core’-implementation will be more complex).

Looking at the energy formula from Eq. 5.15, at a first glance, two fitting parameters would appear, namely the largest moment of inertia  $\mathcal{I}_3$  and the wobbling frequency  $\hbar\omega$ . However, the wobbling frequency is furthermore dependent on the other two moments of inertia (as per Eq. 5.12), meaning that one can use the set  $\mathcal{P}_{\text{fit}} = [\mathcal{I}_1, \mathcal{I}_2, \mathcal{I}_3]$  as appropriate fitting parameters. The wobbling phonon number  $n_w$  is attributed as follows:  $n_w = 0$  for the yrast band (denoted throughout calculations with B1) and  $n_w = 1$  for the first excited band (denoted with B2). The band B1 has signature  $\alpha = 0$  so it is the even-spin sequence, while B2 has odd spins. The experimental data regarding spins and energies for the two bands correspond to the measurements done in Ref. [102].

## Energy Spectrum

Indeed, by following the procedure described above, the set  $\mathcal{P}_{\text{fit}}$  is obtained. The parameters, i.e., the three moments of inertia are shown in Table 5.1. Remarking that fact that the largest MOI which was obtained via the fitting procedure is the one corresponding to the 3-axis. With these parameters, the theoretical energies are determined numerically and the two bands are compared to the measured data in Fig. 5.4. Concerning the fitted energies, in the present calculations, instead of working with the ‘absolute energies’ (i.e., the exact values of the energies that correspond to the measured spectrum), the *excitation energies* were used instead [40, 104, 105]. These are determined by subtracting the band-head energy of B1 (the  $10^+$  level) from each excited state of B1 and B2. Doing this improves the

$\mathcal{P}_{\text{fit}}$			
$\mathcal{I}_1$	$\mathcal{I}_3$	$\mathcal{I}_2$	Unit
27	22	43	$\hbar^2 \text{MeV}^{-1}$

TABLE 5.1: The parameter set  $\mathcal{P}_{\text{fit}}$  obtained from the fitting procedure of the excitation energies of the two wobbling bands (B1 and B2) for  $^{130}\text{Ba}$ . The model function corresponds to the energy of a simple wobbler (see Eq. 5.15).

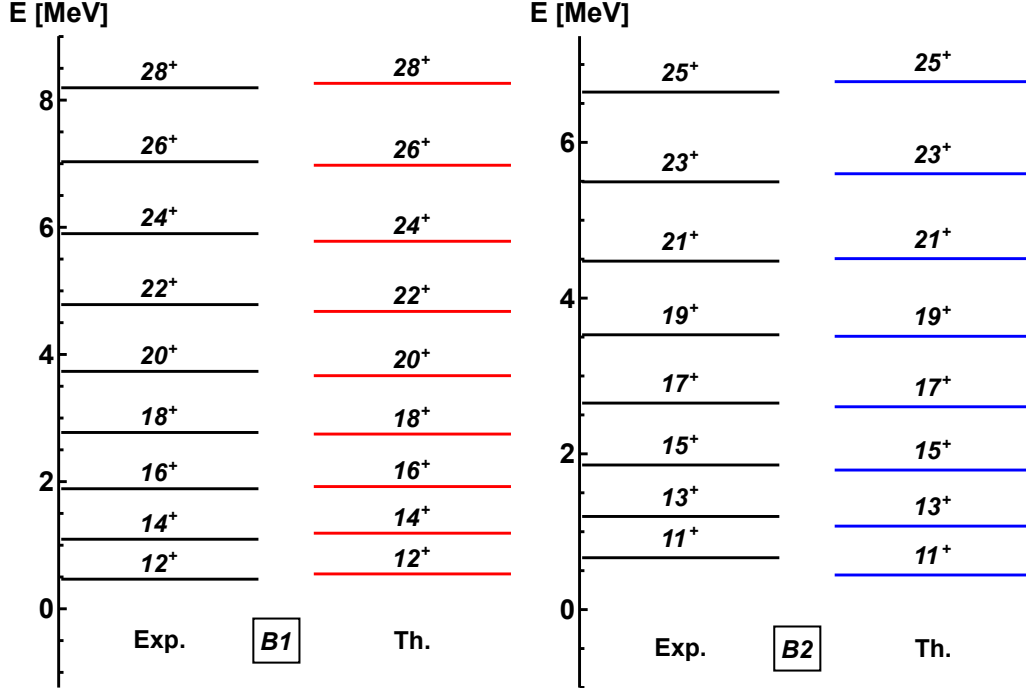


FIGURE 5.4: Comparison between the experimental and theoretical excitation energies (Eq. 5.26) for the two wobbling bands of  $^{130}\text{Ba}$  (B1 and B2). Experimental data is taken from Ref. [102]. The theoretical data was obtained by fitting Eq. 5.15 as described in text, with the parameters defined in Table 5.1. Note that the band-head  $I^\pi = 10^+$  state from B1 is missing from the spectrum since it was subtracted from each level.

accuracy of the results. The excitation energy for a spin state  $I$  is given as:

$$E(I) = E_{\text{abs}}(I) - E_{\text{abs}}(I_0) , \quad (5.26)$$

where ‘abs.’ signifies the absolute value for  $E$  at that particular spin state and  $I_0$  is the band-head state within the yrast band.

Besides the excited spectrum obtained in Fig. 5.4, other quantities such as the rotational frequencies for the two bands in  $^{130}\text{Ba}$  are compared with experimental values in Fig. 5.5, and the obtained results agree with the measured data quite well. Note that both frequencies are increasing functions of angular momentum,

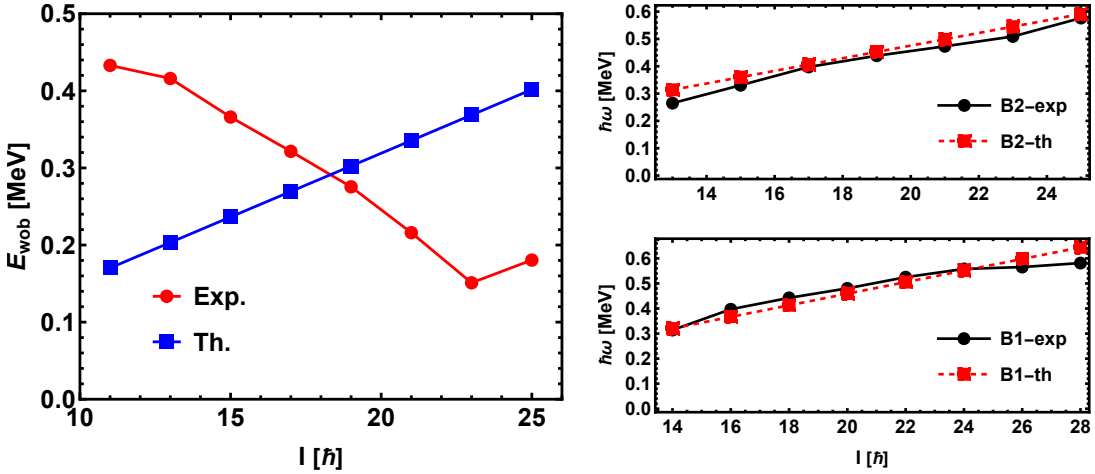


FIGURE 5.5: **Left:** The wobbling energies for  $^{130}\text{Ba}$  calculated with Eq. 5.25. For the first state of B2, the energy was determined as  $E_{\text{wob}}(11^+) = E_{\text{B2}}(11^+) - \frac{1}{2}E_{\text{B1}}(12^+)$  since the band-head state of B1 is zero (as per the definition of excitation energy given in Eq. 5.26). **Right:** The rotational frequencies for the two wobbling bands of  $^{130}\text{Ba}$ , calculated using Eq. 3.77.

although for B1, at spin  $I \geq 24\hbar$ , there seems to be a less of an increase, which is not fully reproduced by the fitted values. Moreover, having the excitation energies for the two bands, one can evaluate the theoretical wobbling energies as defined in Eq. 5.25 and compare them with the experimental values. The two quantities are graphically represented in Fig. 5.5. Remarking the fact that there is an opposite behavior for the two curves, namely the experimental wobbling energies decrease with angular momentum, while the theoretical ones are constantly increasing. Unfortunately, it turns out that by using the Hamiltonian for a *simple wobbler* is not enough to completely describe the collective motion in this isotope.

### Transition Probabilities

Another step regarding the calculations for  $^{130}\text{Ba}$  consists of the electromagnetic transition probabilities. For this investigation some prior quantities are required. Firstly, the reduced transition probabilities  $B(E2)$  (both the interband and the intraband) depend on the components  $Q_{20}$  and  $Q_{22}$  of the quadrupole moment. These two can be evaluated numerically using the expressions from Eq. 5.20, while the intrinsic quadrupole moment is furthermore evaluated using Eq. 3.87. From the microscopic calculations performed by Chen et al. in Ref. [103], they determined that this isotope has a stable triaxial minimum located at  $(\beta_2, \gamma) = (0.24, 21.5^\circ)$ . Within the following computations, this set of deformation

Parameters	Calculated values	Observations
$\beta_2$	0.24	Taken from Ref. [103]
$\gamma$	$21.4^\circ$	Taken from Ref. [103]
$w_1$	1.008	Evaluated with $\mathcal{P}_{\text{fit}}$
$w_2$	0.132	Evaluated with $\mathcal{P}_{\text{fit}}$
$Q_0$	$390.376 \text{ } eb \cdot 10^{-2}$	As per Eq. 3.87
$Q_{20}$	$363.213 \text{ } eb \cdot 10^{-2}$	As per Eq. 5.20
$Q_{22}$	$101.168 \text{ } eb \cdot 10^{-2}$	As per Eq. 5.20
$B(E2)_{\text{in}}$	$0.0509047 \text{ } (eb)^2$	Eq. 5.21

TABLE 5.2: The numerical values for the quantities which are required to determine the quadrupole transition probabilities  $B(E2)$  defined in Eqs. 5.21 - 5.23. The parameter set  $\mathcal{P}_{\text{fit}}$  was obtained through the fitting procedure and the values are shown in Table 5.1. The intraband transition probabilities  $B(E2)$  are evaluated for states  $(n, I) \rightarrow (, , I - 2)$ .

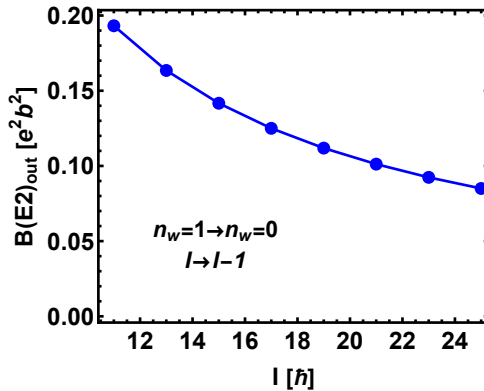


FIGURE 5.6: The interband quadrupole transition probabilities (Eq. 5.22) from the first excited wobbling band (B2) to the yrast band (B1) for  $^{130}\text{Ba}$ .

parameters will be used. Taking the value of  $\beta_2 = 0.24$ , the intrinsic quadrupole moment  $Q_0$  is readily obtained from Eq. 3.87. The transition probabilities from Eqs. 5.21, 5.22, and 5.23 also depend on the two factors  $w_{1,2}$  defined in Eq. 5.11, which are functions of the three moments of inertia. Thus, the quality of the fitting procedure will also reflect the calculus for the transition probabilities through  $\mathcal{P}_{\text{fit}}$ . The numerical values for  $Q_0$ ,  $w_{1,2}$ , and  $Q_{20,22}$  are presented in Table 5.2. Having the deformation parameters, the  $w_{1,2}$  terms, and the quadrupole components, one can evaluate the reduced transition probabilities.

The graphical representation from Fig. 5.6 shows the interband transition probabilities  $B(E2)_{\text{out}}$  for states  $(n_w = 1, I) \rightarrow (n_w = 0, I - 1)$ . These values are determined with the parameters defined in Table 5.2. A constant decrease with spin can be observed, and an overall agreement with theoretical calculations from Ref. [103] is observed (see inset *a* from Fig. 4).

$I$	$\frac{B(E2)_{\text{out}}}{B(E2)_{\text{in}}}$	
	Experimental	Calculated
11		0.379505
13	0.32	0.32112
15	0.36	0.278304
17	0.22	0.245562
19	0.22	0.219714
21	0.41	0.198788
23		0.181502
25		0.166982

TABLE 5.3: The ratios  $\frac{B(E2)_{\text{out}}}{B(E2)_{\text{in}}}$  for  $^{130}\text{Ba}$ . The experimental data (where available) was taken from Ref. [102, 103].

Considering the interband transitions  $B(E2)_{\text{out}}$  calculated above and the constant value for  $B(E2)_{\text{in}}$  (typical for the HA), the ratios  $B(E2)_{\text{out}}/B(E2)_{\text{in}}$  can also be evaluated. These values are good indicators if a nucleus has a strong deformation and for a wobbler, they lie within  $0.2 - 0.5$ . In Table 5.3, the obtained ratios are compared with the experimental ones, where a decent agreement can be seen. The theoretical values are decreasing with spin.

### Harmonic Approximation - General Discussion

Even though the spectrum of this even-even nucleus has been quantitatively reproduced quite well and the values for the tree obtained MOI indicate a triaxial nucleus with main rotation around the third axis, it should not be considered a ‘realistic’ tool in describing this isotope. This is because in another work, Chen et al. [103] found through microscopic calculations that the wobbling motion does not occur as per a pure triaxial rotator, but it emerges from the coupling of two quasi-particles  $\pi(h_{11/2})^2$  with a triaxial core. In fact, their work shows that  $^{130}\text{Ba}$  is the first nucleus in which a configuration with two quasi-particles generates stable triaxial deformation through wobbling motion. Consequently, the numerical implementation performed here only shows that HA can be a suitable tool to show that  $^{130}\text{Ba}$  does behave as a wobbler, but this pure triaxial rotator model *hides* contributions coming from single-particle configuration within the final Hamiltonian. This translates to the fact that Eq. 5.15 contains the effect of the two  $h_{11/2}$  protons hidden within  $\hbar\omega_w$ . In fact, looking back at  $E_{\text{wob}}$  from Fig. 5.5, the discrepancy of the two lines is a clear indicator that some other terms should be

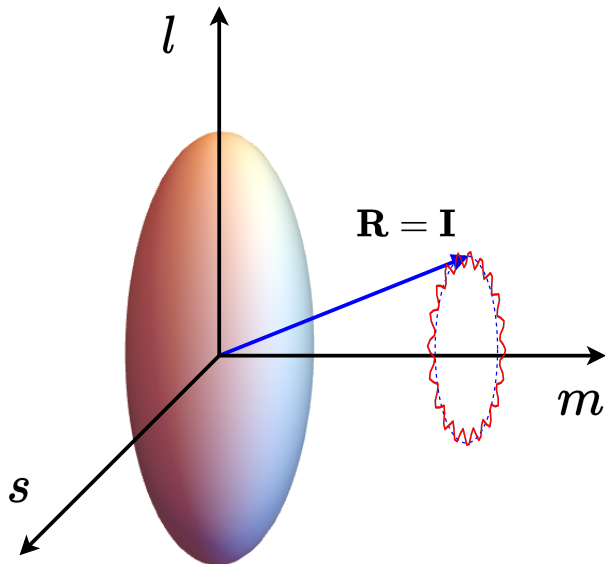


FIGURE 5.7: A schematic representation with a *simple wobbler*, with the total angular momentum doing a precessional motion about the axis with largest MOI. In this particular sketch, the axis with largest MOI is denoted with  $m$  for intermediate/medium.  $l$ - and  $s$ -axis represent the long and short axes, respectively. The small-amplitude oscillations of  $\mathbf{R}$  are depicted with the (red) encircled sine wave. This figure was adapted from Ref. [106] and inspired from Ref. [107].

taken into account. Also, it is worth mentioning that a quenching factor was necessary in the expression of  $B(E2)_{\text{in},\text{out}}$  in order to compensate for the magnitude of  $w_{1,2}$ . Nevertheless, this simple and straightforward formalism used to describe the wobbling bands in the even-even  $^{130}\text{Ba}$  nucleus proves to be a decent tool. The calculations presented here have been done independently by the current team, and the obtained results are unique to this research. They will be considered towards a separate forthcoming publication.

Concluding this section on wobbling motion of even-even nuclei, a final sketch is depicted in Fig. 5.7, where the main axes of the triaxial ellipsoid are represented and denoted with  $m$ ,  $s$ , and  $l$ -axis (medium, short and long, respectively). The precession motion of the total angular momentum (the a.m. of the core itself) will be around the  $m$ -axis, having the largest moment of inertia.

## 5.2 Wobbling Motion in Odd-Mass Nuclei

# Bibliography

- [1] Aage Niels Bohr and Ben R Mottelson. *Nuclear Structure (In 2 Volumes)*. World Scientific Publishing Company, 1998.
- [2] H Morinaga and PC Gugelot. Gamma rays following ( $\alpha$ , xn) reactions. *Nuclear Physics*, 46:210–224, 1963.
- [3] Walter Greiner and Joachim A Maruhn. *Nuclear models*. Springer, 1996.
- [4] Peter Ring and Peter Schuck. *The nuclear many-body problem*. Springer Science & Business Media, 2004.
- [5] Aage Bohr. *Rotational states of atomic nuclei*. Munksgaard, 1954.
- [6] Samuel SM Wong. *Introductory nuclear physics*. John Wiley & Sons, 2008.
- [7] G Andersson, SE Larsson, G Leander, P Möller, Sven Gösta Nilsson, Ingemar Ragnarsson, Sven Åberg, R Bengtsson, J Dudek, B Nerlo-Pomorska, et al. Nuclear shell structure at very high angular momentum. *Nuclear Physics A*, 268(2):205–256, 1976.
- [8] James Till Matta. *Exotic Nuclear Excitations: The Transverse Wobbling Mode in 135 Pr*. Springer, 2017.
- [9] R Casten and Richard F Casten. *Nuclear structure from a simple perspective*, volume 23. Oxford University Press on Demand, 2000.
- [10] Michael Christopher Lewis. *Lifetime Measurements of Excited States in 163 W and the Properties of Multiparticle Configurations in 156 Lu*. The University of Liverpool (United Kingdom), 2019.
- [11] Ingemar Ragnarsson and Sven Gvsta Nilsson. Shapes and shells in nuclear structure. *Shapes and Shells in Nuclear Structure*, 2005.

- [12] QB Chen, SQ Zhang, PW Zhao, and J Meng. Collective hamiltonian for wobbling modes. *Physical Review C*, 90(4):044306, 2014.
- [13] CF von Weizsäcker. Zur theorie der kernmassen. *Zeitschrift für Physik*, 96(7):431–458, 1935.
- [14] Kenneth S Krane. *Introductory nuclear physics*. John Wiley & Sons, 1991.
- [15] Subramanyan Raman, CW Nestor Jr, and P Tikkanen. Transition probability from the ground to the first-excited  $2^+$  state of even-even nuclides. *Atomic Data and Nuclear Data Tables*, 78(1):1–128, 2001.
- [16] Roger D Woods and David S Saxon. Diffuse surface optical model for nucleon-nuclei scattering. *Physical Review*, 95(2):577, 1954.
- [17] Brian R Martin and Graham Shaw. *Particle physics*. John Wiley & Sons, 2017.
- [18] Carlos A Bertulani. *Nuclear physics in a nutshell*. Princeton University Press, 2007.
- [19] CJ Gallagher Jr and SA Moszkowski. Coupling of angular momenta in odd-odd nuclei. *Physical Review*, 111(5):1282, 1958.
- [20] Sven Gösta Nilsson. Binding states of individual nucleons in strongly deformed nuclei. *Dan. Mat. Fys. Medd.*, 29(CERN-55-30):1–69, 1955.
- [21] C Gustafson, IL Lamm, B Nilsson, and SG Nilsson. Nuclear deformabilities in the rare-earth and actinide regions with excursions off the stability line and into the super-heavy region. Technical report, Lund Inst. of Tech., Sweden, 1967.
- [22] Adam Benjamin Garnsworthy. *Neutron-proton interactions in heavy self-conjugate nuclei*. University of Surrey (United Kingdom), 2007.
- [23] S Frauendorf and F Dönau. Transverse wobbling: A collective mode in odd-a triaxial nuclei. *Physical Review C*, 89(1):014322, 2014.
- [24] Biswarup Das. *NUCLEAR STRUCTURE STUDIES AT HIGH ANGULAR MOMENTUM IN MASS 100 REGION*. PhD thesis, HOMI BHABHA NATIONAL INSTITUTE, 2018.

- 
- [25] Ikuko Hamamoto. Interplay between one-particle and collective degrees of freedom in nuclei. *Physica Scripta*, 91(2):023004, 2016.
  - [26] AS Davydov and GF Filippov. Rotational states in even atomic nuclei. *Nuclear Physics*, 8:237–249, 1958.
  - [27] Charles H Townes, HM Foley, and W Low. Nuclear quadrupole moments and nuclear shell structure. *Physical Review*, 76(9):1415, 1949.
  - [28] M Goldhaber and AW Sunyar. Classification of nuclear isomers. *Physical Review*, 83(5):906, 1951.
  - [29] Aage Niels Bohr and Benjamin Roy Mottelson. Collective and individual-particle aspects of nuclear structure. *Dan. Mat. Fys. Medd.*, 27(CERN-57-38):1–174, 1953.
  - [30] Niels Bohr. Neutron capture and nuclear constitution. *Nature*, 137(3461):344–348, 1936.
  - [31] James Rainwater. Nuclear energy level argument for a spheroidal nuclear model. *Physical Review*, 79(3):432, 1950.
  - [32] Albert Messiah. *Quantum mechanics*. Courier Corporation, 2014.
  - [33] ZP Li and D Vretenar. Model for collective motion. *arXiv preprint arXiv:2203.07608*, 2022.
  - [34] K Kitao, Y Tendow, and A Hashizume. Nuclear data sheets for  $a = 120$ . *Nuclear Data Sheets*, 96(2):241–390, 2002.
  - [35] E Browne and JK Tuli. Nuclear data sheets for  $a = 60$ . *Nuclear Data Sheets*, 114(12):1849–2022, 2013.
  - [36] Jun Chen, Balraj Singh, and John A Cameron. Nuclear data sheets for  $a = 44$ . *Nuclear Data Sheets*, 112(9):2357–2495, 2011.
  - [37] Alan L Nichols, Balraj Singh, and Jagdish K Tuli. Nuclear data sheets for  $a = 62$ . *Nuclear Data Sheets*, 113(4):973–1114, 2012.
  - [38] Bai Erjun and Huo Junde. Nuclear data sheets for  $a = 63$ . *Nuclear Data Sheets*, 92(1):147–252, 2001.

- [39] TM Corrigan, FJ Margelan, and SA Williams. Exact solution of the quadrupole surface vibration hamiltonian in body-fixed coordinates. *Physical Review C*, 14(6):2279, 1976.
- [40] AA Raduta, R Poenaru, and L Gr Ixaru. Semiclassical unified description of wobbling motion in even-even and even-odd nuclei. *Physical Review C*, 96(5):054320, 2017.
- [41] N Nica. Nuclear data sheets for  $a = 158$ . *Nuclear Data Sheets*, 141:1–326, 2017.
- [42] Elizabeth A McCutchan. Nuclear data sheets for  $a = 180$ . *Nuclear Data Sheets*, 126:151–372, 2015.
- [43] Pierre Celestin Uwitonze. *Assignment of Spin and Parity to States in the Nucleus 196T1*. PhD thesis, Rhodes University, 2015.
- [44] Xiaofeng Wang. *Exotic collective excitations at high spin: triaxial rotation and octupole condensation*. University of Notre Dame, 2007.
- [45] Stefan Frauendorf and Jie Meng. Tilted rotation of triaxial nuclei. *Nuclear Physics A*, 617(2):131–147, 1997.
- [46] Yang Sun, Shuxian Wen, et al. Varied signature splitting phenomena in odd proton nuclei. *Physical Review C*, 50(5):2351, 1994.
- [47] CW Reich and Balraj Singh. Nuclear data sheets for  $a = 163$ . *Nuclear Data Sheets*, 111(5):1211–1469, 2010.
- [48] MR Bhat. Evaluated nuclear structure data file (ensdf). In *Nuclear data for science and technology*, pages 817–821. Springer, 1992.
- [49] R Bengtsson and S Frauendorf. Quasiparticle spectra near the yrast line. *Nuclear Physics A*, 327(1):139–171, 1979.
- [50] Samuel M Harris. Higher order corrections to the cranking model. *Physical Review*, 138(3B):B509, 1965.
- [51] R Bengtsson, H Frisk, FR May, and JA Pinston. Signature inversion—a fingerprint of triaxiality. *Nuclear Physics A*, 415(2):189–214, 1984.
- [52] J Kvasil and RG Nazmitdinov. Backbending and  $\gamma$  vibrations. *Physical Review C*, 69(3):031304, 2004.

- [53] Saddon T Ahmad, M Kotb, Idris H Salih, and Hewa Y Abdullah. Backbending phenomena in even-even [formula omitted] hf isotopes. *Physics of Atomic Nuclei*, 84(1):18–29, 2021.
- [54] CS Wu, L Cheng, CZ Lin, and JY Zeng. Relation between the kinematic and dynamic moments of inertia in superdeformed nuclei. *Physical Review C*, 45(5):2507, 1992.
- [55] CS Wu, JY Zeng, Z Xing, XQ Chen, and J Meng. Spin determination and calculation of nuclear superdeformed bands in a 190 region. *Physical Review C*, 45(1):261, 1992.
- [56] N Nica. Nuclear data sheets for  $a = 160$ . *Nuclear Data Sheets*, 176:1–428, 2021.
- [57] CW Reich. Nuclear data sheets for  $a = 162$ . *Nuclear Data Sheets*, 108(9):1807–2034, 2007.
- [58] AS Davydov and AA Chaban. Rotation-vibration interaction in non-axial even nuclei. *Nuclear Physics*, 20:499–508, 1960.
- [59] Ben R Mottelson and JG Valatin. Effect of nuclear rotation on the pairing correlation. *Physical Review Letters*, 5(11):511, 1960.
- [60] J Kruelinde and Z Szymański. On the effect of quadrupole pairing interaction on the backbending behaviour in rotating nuclei. *Physics Letters B*, 53(4):322–324, 1974.
- [61] AA Raduta and R Budaca. Semimicroscopic description of backbending phenomena in some deformed even-even nuclei. *Physical Review C*, 84(4):044323, 2011.
- [62] Frank S. Stephens, Peter Kleinheinz, Raymond K. Sheline, and Reinhard S Simon. Backbending and rotation alignment. *Nuclear Physics*, 222:235–251, 1974.
- [63] Frank S. Stephens and Reinhard S Simon. Coriolis effects in the yrast states. *Nuclear Physics*, 183:257–284, 1972.
- [64] Kris LG Heyde. The nuclear shell model. In *The Nuclear Shell Model*, pages 58–154. Springer, 1994.

- [65] R Neugart and G Neyens. Nuclear moments. In *The Euroschool Lectures on Physics with Exotic Beams, Vol. II*, pages 135–189. Springer, 2006.
- [66] R Budaca. Tilted-axis wobbling in odd-mass nuclei. *Physical Review C*, 97(2):024302, 2018.
- [67] Peter Möller, Ragnar Bengtsson, B Gillis Carlsson, Peter Olivius, and Takatoshi Ichikawa. Global calculations of ground-state axial shape asymmetry of nuclei. *Physical review letters*, 97(16):162502, 2006.
- [68] GD Dracoulis, GJ Lane, AP Byrne, H Watanabe, RO Hughes, Filip G Kondev, M Carpenter, RVF Janssens, T Lauritsen, CJ Lister, et al. Isomers and excitation modes in the gamma-soft nucleus  $^{192}\text{Os}$ . *Physics Letters B*, 720(4-5):330–335, 2013.
- [69] SW Ødegård, GB Hagemann, DR Jensen, M Bergström, B Herskind, G Sletten, S Törmänen, JN Wilson, PO Tjøm, I Hamamoto, et al. Evidence for the wobbling mode in nuclei. *Physical review letters*, 86(26):5866, 2001.
- [70] DR Jensen, GB Hagemann, I Hamamoto, SW Ødegård, B Herskind, G Sletten, JN Wilson, K Spohr, H Hübel, P Bringel, et al. Evidence for second-phonon nuclear wobbling. *Physical review letters*, 89(14):142503, 2002.
- [71] Shi Wen-Xian and Chen Qi-Bo. Wobbling geometry in a simple triaxial rotor. *Chinese Physics C*, 39(5):054105, 2015.
- [72] J Peng, J Meng, and SQ Zhang. Description of chiral doublets in a  $^{130}$  nuclei and the possible chiral doublets in a  $^{100}$  nuclei. *Physical Review C*, 68(4):044324, 2003.
- [73] Matthias Brack, Jens Damgaard, AS Jensen, HC Pauli, VM Strutinsky, and CY Wong. Funny hills: The shell-correction approach to nuclear shell effects and its applications to the fission process. *Reviews of Modern Physics*, 44(2):320, 1972.
- [74] Tord Bengtsson. A method to remove virtual interactions with applications to nuclear spectroscopy. *Nuclear Physics A*, 496(1):56–92, 1989.
- [75] Tord Bengtsson. The high-spin structure of  $^{158}\text{Er}$ : A theoretical study. *Nuclear Physics A*, 512(1):124–148, 1990.

- [76] MK Djongolov, DJ Hartley, LL Riedinger, Filip G Kondev, RVF Janssens, K Abu Saleem, I Ahmad, DL Balabanski, MP Carpenter, P Chowdhury, et al. Extending the region of triaxial superdeformation: candidate tsd bands in  $^{174}\text{hf}$ . *Physics Letters B*, 560(1-2):24–30, 2003.
- [77] K Nomura and CM Petrache. Examining the wobbling interpretation of low-lying bands in gamma-soft nuclei within the interacting boson-fermion model. *arXiv e-prints*, pages arXiv–2106, 2021.
- [78] D Ringkøbing Jensen, GB Hagemann, I Hamamoto, SW Ødegård, M Bergström, B Herskind, G Sletten, S Törmänen, JN Wilson, PO Tjøm, et al. Wobbling phonon excitations, coexisting with normal deformed structures in  $^{163}\text{lu}$ . *Nuclear Physics A*, 703(1-2):3–44, 2002.
- [79] Yingqiong Gu. *Theoretical investigation of triaxial strong deformation and tidal waves in nuclei*. University of Notre Dame, 2007.
- [80] H Schnack-Petersen, Ragnar Bengtsson, RA Bark, P Bosetti, A Brockstedt, H Carlsson, LP Ekström, GB Hagemann, B Herskind, F Ingebretsen, et al. Superdeformed triaxial bands in  $^{163,165}\text{lu}$ . *Nuclear Physics A*, 594(2):175–202, 1995.
- [81] Ikuko Hamamoto and Ben Mottelson. On the intrinsic spectra of rotating nuclei with tri-axial shape. *Physics Letters B*, 127(5):281–285, 1983.
- [82] Chong Qi, Roberto Liotta, and Ramon Wyss. Recent developments in radioactive charged-particle emissions and related phenomena. *Progress in Particle and Nuclear Physics*, 105:214–251, 2019.
- [83] R Budaca and AI Budaca. Deformation dependence of the screened decay law for proton emission. *Nuclear Physics A*, 1017:122355, 2022.
- [84] Peter Möller, Arnold J Sierk, Takatoshi Ichikawa, Akira Iwamoto, Ragnar Bengtsson, Henrik Uhrenholt, and Sven Åberg. Heavy-element fission barriers. *Physical Review C*, 79(6):064304, 2009.
- [85] Bing-Nan Lu, En-Guang Zhao, Shan-Gui Zhou, et al. Potential energy surfaces of actinide nuclei from a multidimensional constrained covariant density functional theory: Barrier heights and saddle point shapes. *Physical Review C*, 85(1):011301, 2012.

- [86] F Palumbo and A Richter. Splitting of the magnetic dipole giant resonance and triaxial deformation. *Physics Letters B*, 158(2):101–102, 1985.
- [87] Gregoire Henning. *Stability of transfermium elements at high spin: measuring the fission barrier of  $^{254}\text{No}$* . PhD thesis, Paris 11, 2012.
- [88] J Simpson. The euroball spectrometer. *Zeitschrift für Physik A Hadrons and Nuclei*, 358(2):139–143, 1997.
- [89] I-Yang Lee. The gammasphere. *Nuclear Physics A*, 520:c641–c655, 1990.
- [90] Akaa Daniel Ayangeakaa. *Exotic Modes of Collective Excitations: Nuclear Tidal Waves and Chirality*. PhD thesis, University of Notre Dame, 2013.
- [91] Nirupama Sensharma. *Wobbling Motion in Nuclei: Transverse, Longitudinal and Chiral*. University of Notre Dame, 2021.
- [92] K Starosta, T Koike, CJ Chiara, DB Fossan, DR LaFosse, AA Hecht, CW Beausang, MA Caprio, JR Cooper, R Krücken, et al. Chiral doublet structures in odd-odd  $n=75$  isotones: Chiral vibrations. *Physical review letters*, 86(6):971, 2001.
- [93] SQ Zhang, Bin Qi, SY Wang, and J Meng. Chiral bands for a quasi-proton and quasi-neutron coupled with a triaxial rotor. *Physical Review C*, 75(4):044307, 2007.
- [94] J Meng, B Qi, SQ Zhang, and SY Wang. Chiral symmetry in atomic nuclei. *Modern Physics Letters A*, 23(27n30):2560–2567, 2008.
- [95] R Budaca. Semiclassical description of chiral geometry in triaxial nuclei. *Physical Review C*, 98(1):014303, 2018.
- [96] R Budaca. From chiral vibration to tilted-axis wobbling within broken chiral symmetry. *Physics Letters B*, 817:136308, 2021.
- [97] EA Mccutchan. Nuclear data sheets for  $a=136$ . *Nuclear Data Sheets*, 152:331–667, 2018.
- [98] E Grodner, J Srebrny, Ch Droste, T Morek, A Pasternak, and J Kownacki. Ds<sub>am</sub> lifetime measurements in the yrast band of  $^{131}\text{la}$  and the chiral bands in  $^{132}\text{la}$ . *International Journal of Modern Physics E*, 13(01):243–246, 2004.

- [99] E Grodner, I Zalewska, T Morek, J Srebrny, Ch Droste, M Kowalczyk, J Mierzejewski, M Sałata, AA Pasternak, J Kownacki, et al. Lifetime measurements in  $^{128}\text{Cs}$  and  $^{132}\text{La}$  as a test of chirality. *International Journal of Modern Physics E*, 14(03):347–352, 2005.
- [100] Makito Oi. Semi-classical and anharmonic quantum models of nuclear wobbling motion. *Physics Letters B*, 634(1):30–34, 2006.
- [101] Takuya Shoji and Yoshifumi R Shimizu. Microscopic description of nuclear wobbling motion rotation of triaxially deformed nuclei. *International Journal of Modern Physics E*, 15(07):1407–1416, 2006.
- [102] CM Petrache, PM Walker, S Guo, QB Chen, S Frauendorf, YX Liu, RA Wyss, D Mengoni, YH Qiang, A Astier, et al. Diversity of shapes and rotations in the  $\gamma$ -soft  $^{130}\text{Ba}$  nucleus: First observation of a t-band in the  $a = 130$  mass region. *Physics Letters B*, 795:241–247, 2019.
- [103] QB Chen, S Frauendorf, and CM Petrache. Transverse wobbling in an even-even nucleus. *Physical Review C*, 100(6):061301, 2019.
- [104] AA Raduta, R Poenaru, and Al H Raduta. Wobbling motion in  $^{164}\text{Lu}$  within a semi-classical framework. *Journal of Physics G: Nuclear and Particle Physics*, 45(10):105104, 2018.
- [105] AA Raduta, R Poenaru, and CM Raduta. Towards a new semi-classical interpretation of the wobbling motion in  $^{163}\text{Lu}$ . *Journal of Physics G: Nuclear and Particle Physics*, 47(2):025101, 2020.
- [106] R Poenaru and AA Raduta. Extensive study of the positive and negative parity wobbling states for an odd-mass triaxial nucleus ii: Classical trajectories. *Romanian Journal of Physics*, 66(9-10), 2021.
- [107] N Sensharma, U Garg, QB Chen, S Frauendorf, DP Burdette, JL Cozzi, KB Howard, S Zhu, MP Carpenter, P Copp, et al. Longitudinal wobbling motion in  $^{187}\text{Au}$ . *Physical review letters*, 124(5):052501, 2020.